Doctorate School In Information And Communication Technologies

University of Modena And Reggio Emilia
Department Of Engineering *Enzo Ferrari*

High brightness solid state optical sources and visually safe lighting

Tutor:
Prof. Ing. Luigi Rovati

The Director of the School:
Prof. Ing. Giorgio M. Vitetta

The Coordinator of the Doctorate:
Prof. Ing. Giorgio M. Vitetta

PhD dissertation of:

Mario Bernabei
77387

XXVIII Cycle

Contents

List of Tables

List of Figures

Chapter 1

Abstract

The big changes in indoor illumination caused by the introduction of LED-based devices may have effects on the health and well-being of the persons that are still under study. The key device of these new commercial sources is the Gallium Nitride based (GaN) LED. This device developed at the end of the 90's has made possible to revolutionize the lighting world. Despite all, the device has some critical aspects which depend on the construction technology and not well-controlled physical parameters. The physical phenomenon that affects the GaN LED devices is the efficiency droop. The main physical mechanisms causing the efficiency droop in InGaN/GaN blue light-emitting diodes and remedies proposed for droop mitigation are classified and reviewed in this work. Droop mechanisms taken into consideration are Auger recombination, reduced active volume effects, carrier delocalization, and carrier leakage. Many approaches to compensate this droop have been proposed in literature, that actually allow the devices to achieve thresholds lumens/watt enough high to substitute of the usual light sources, but without solving the problem. Numerical device simulations of a reference device are used through this work as a proof of concept for selected mechanisms and remedies.
It is also important to study the light emitted from these new solid state sources, and the effect that this radiation has on the human visual system. The actual regulations standardize the intensity and fluctuations of the light emitted in indoor spaces as workplace or house and outdor, unfortunately these regulations are obsolete because are based on light sources now banned from production and the market in general. In the specific from the point of view of flicker, these changes further highlight the inadequacy of the current international standard EN 61000-4-15 which has been adopted by the IEEE as IEEE std 1453, gives functional and design specifications about the actual Flickermeter based on the analysis of the voltage supplying a specified light source, such incandescent light source based instrument is obsolete nowadays, with the advent of new light sources, such as halogen, fluorescent, and

especially solid state sources; a different and appropriate tools is mandatory to investigate the effects on the human eye of these sources. With the aim of providing a contribution to a matter that involves several scientific disciplines, new results on pupil responses induced by RGB flickering stimuli are presented in this work. Tests on volunteers have been performed to evaluate the inter- and intra-subject variability of pupil responses induced by the above stimuli and reported. An instrument formerly developed has been used to investigate the pupil response is described in this work.

Chapter 2

Acknoledgment

I would like to thank first of all my tutors, Prof. Luigi Rovati and Porf. Giovanni Verzellesi for being a point of reference and a guide on which to rely. Thanks for the precious collaboration to Prof. Roberto Tinarelli and Prof. Lorenzo Peretto. Many thanks to all the people with who I spent the PhD period, Elecom Optolab boys in particular Ing. Stefano Cattini for precious advices, availability and friendship. Finally, thanks to my family to supporting me and a special thanks to Elena to who i dedicate this work.

Chapter 3

Introduction

Indoor illumination has undergone big changes in recent years. LED-based products have replaced conventional light sources in several indoors environments providing both superior efficiency and performance with capabilities such as tunable lighting. Gallium nitride (GaN) light-emitting diodes (LEDs) are rapidly saturating the LCD backlighting market and have already started to penetrate the general illumination one [2]. In order for this market expansion to be as fast as projected, the cost-per-lumen of packaged LEDs must rapidly decrease within the next few years, from the present average values of 12.5-9 $\$/klm$, down to 2.3-2 $\$/klm$ in 2015, with an ultimate goal of 0.5 $\$/klm$ after 2020. Correspondingly, the luminous efficacy must increase from the 2011 values of 98-135 lm/W up to 162-190 lm/W in 2015, with ultimate goals of 199 lm/W and 266 lm/W to be approached after 2020 for phosphor-converted and color-mixed LEDs, respectively [3]. All LED package elements will have to contribute to this cost/performance roadmap, including the LED chip. To this respect, the above forecasted efficacy improvements call for improved *internal quantum efficiency* (IQE), besides higher light extraction efficiency and reduced series resistances.

However, the effects on health and wellbeing of this light sources are still under study and investigation by researchers. Unfortunately, the present state of knowledge doesn't provide a reliable and quantitative description of some visual perception parameters when LED light is involved. The most investigated health effects relate with the toxic effect of blue light and risk of glare (EN 62471 blue hazard, [4]). It is known that the blue light, necessary to excite phosphors and thus generate white radiation, causes toxic stress to the retina. This issue is particularly critical in children as their crystalline lens is unable to filter the blue components of light efficiently. Many LED lamps recently introduced on the market emit warmer shades of white light, thus reducing the blue light content in the spectrum. Concerning the glare effects, Iacomussi et al. [5] show as the effect of glare is practically indepen-

dent from the emission spectrum of the light source at higher adaptation luminances (22 cd/m^2) while at lower adaptation luminances LED (9 cd/m^2) LED sources give better performances then incandescent lamps. Many lighting LEDs products now available on the market use diffusers to reduce glare (reduction of the radiance) and, according to [6], the most part of lighting LED products present low risks or no risk at all for the general population when the viewing distance is equal to or greater than 200 mm.

Indoor ambient lighting also has an important effect on wellbeing, in particular when the exposure is prolonged and/or susceptible populations are exposed, e.g. offices, classrooms, hospitals and daycare centers. Several studies report the impact of lighting flicker on well-being, performance and physiological arousal [7] [8]. Unfortunately, standards and instruments available to regulate ambient lighting flicker refer to a specific incandescent filament lamp [9] and thus are not suitable for LED-based products. Standardized flicker measurement procedures are not yet in place, and existing flicker metrics have evident inadequacies for LED products. Electrical and photometric flicker for a LED lamps are related to physical phenomena completely different respect to the conventional illumination sources. For example, Rand et al. reported as commercially available LED lamps produce electrical flicker in the 15Hz range when connected to a conventional residential dimmer [10]. Electrical drivers used for biasing the LEDs basically determine fluctuations in the driving current that result in photometric flicker. Optical measurements can actually determines these fluctuations, however this information does not reflect what is actually perceived by the human eye. In fact, the pupil reflex tends to compensate these fluctuations whenever possible. Practically, up to now, neither electrical nor optical measurements can provide a real quantification of the flicker annoyance. In previous papers form our group [11] [12] [13], we proposed a method aimed at investigating the effect of flicker by means of the pupil diameter analysis. In the literature, the pupil response has already been proposed to provide diagnostic and clinical information [14] [15] [16]. These studies highlight as the pupillary response may be related to the physical and mental condition of the human being. Our hypothesis is that also the flicker annoyance can alter the pupillary response. Therefore, a careful analysis of the dynamics of the pupil response could provide quantitative information suitable for the development of a modern regulation [17]. Emission spectra of LED are widely different from those found in conventional light lamps and effects of chromatic flicker could stimulate unusual physiological mechanisms. Therefore, great attention has been devoted to quantification of pupil responses to colored light stimuli. Several researches were aimed on the one hand to assess outer and inner retinal function [18] [19] and on the other hand to evaluate the effects of chromatic flicker [20] [21]. Low-uncertainty and repeatability are the most important characteristics for a pupil-

lometer designed for this application. Although numerous researches on chromatic pupillometry are ongoing and promising results are reported in the literature, no commercially devices are available and no standardized protocols have been defined for clinical usage.

Chapter 4

GaN LED

4.1 InGaN/GaN LED Droop Efficiency

IQE is the ratio of the number of photons emitted per second by the LED active region to the number of carriers injected per second into the active region itself. Ideally, increasing the LED driving current enables the same lumen output to be achieved with less LED chips and/or using smaller LEDs. Unfortunately, this straightforward route to cost-per-lumen reduction is not readily available in actual GaN LEDs, these being affected by a phenomenon, generally called efficiency droop (hereafter droop, for brevity), that makes IQE to decline at high driving current density. More specifically, IQE typically peaks at a few A/cm^2 and then drops at increasing current density down to values that can be as low as 50% of the peak value for current densities in the order of hundreds of A/cm^2. This phenomenon takes place also under pulsed operation at duty cycles and pulse widths for which thermal effects can be ruled out as a cause for IQE decay. Therefore, in state-of-the-art GaN LEDs, increasing the driving current as a means to reduce the cost-per-lumen involves a significant tradeoff in terms of reduced IQE and overall power efficiency. Despite having been the subject of extensive research efforts for a decade, the physical origin of droop has not been clarified. Correspondingly, several technological modifications to the GaN LED structure have been proposed as droop remedies. Some of these approaches have been successfully demonstrated in laboratory LED prototypes, but no unequivocal design rules have been established yet to over- come droop either at a commercial level or in the lab.

4.1.1 LED Basics

A simple way to efficiently generate light in many semiconductors is to fabricate the material as a pn-junction diode. In this manner, stimulated electrons can be efficiently and directly used to generate light, and a great deal of control can be exercised over the fabrication of the light-emitting region and the efficiency of the device.

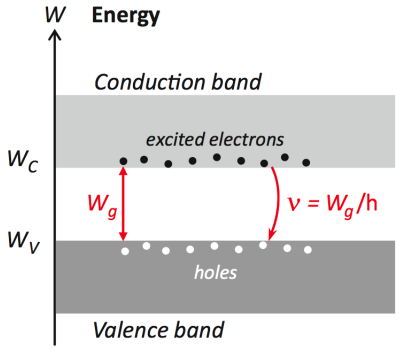

Figure 4.1: Light emission occurs when an excited electron falls back from the conduction band with a direct energy state transition into the valence band and recombines with a hole.

Generally speaking, light generation in a semiconductor occurs when an excited electron resumes equilibrium through a direct conduction band to valence band transition by recombining with a hole in the valence band as the picture 4.1 report. The frequency and the wavelength of the emitted photon is determined by the $W_g = W_c - W_v$ bandgap energy as follows:

$$\nu = W_g/h \tag{4.1}$$

$$\lambda = c/\nu = c \cdot h/W_g \tag{4.2}$$

where h is Planck constant and c denotes the speed of light. As seen from 4.1 and 4.2, the most important parameter to determine the properties of the emitted light is the energy band structure of the semiconductor material used. Semiconductor materials are classified as *direct bandgap* or *indirect bandgap* materials. Light emission takes place in pn-junctions formed in direct bandgap materials. Direct bandgap materials are characterized by an energy band structure such that the minimum energy level of the conduction band (where unlocalized electrons are free to move in the real physical space formed by the semiconductor lattice) and the maximum of the valence band as the figure 4.2 a) shows.

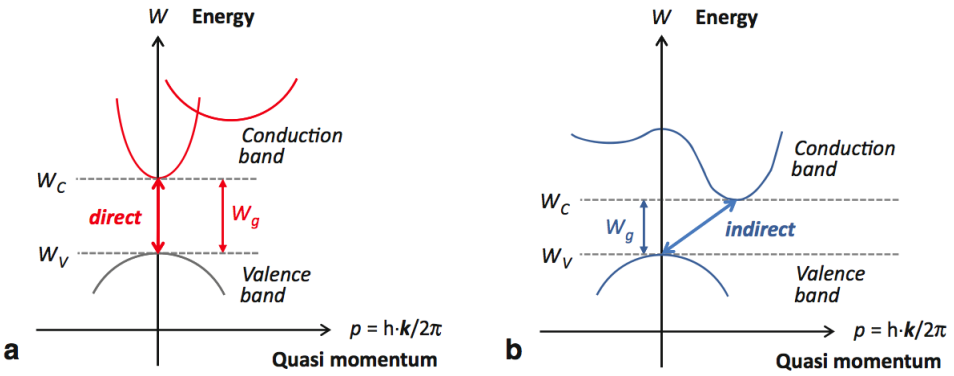

Figure 4.2: Band structure of direct and indirect bandgap materials.

The junction diode provides a simple and efficient technique for placing large number of electrons in an excited state. In order for an electrical current to cross the potential barrier formed by the pn-junction, electrons must be raised from the valence to the conduction band. After the junction has been crossed, the electrons recombine with holes on the p side and this results in photon emission. Such a process is called *radiative recombination*. In contrast to this, in the so-called *non-radiative recombination* processes, as shown in 4.2 instead of photon emission, the energy of the recombining electron is transferred to the vibration energy of the semiconductor lattice by means of phonons, resulting in heat generation.
A major goal of LED device construction is to assure the highest possible ratio of the electrical current associated with radiative recombination with respect to the total current of the LED device. The second goal is to assure that most of the photons generated at a pn-junction of an LED are coupled out to the outer space.
As the picture 4.3 a) shows is a case of an unbiased pn-junction the diffusion potential forms an energy barrier of qV_d which blocks the flow of carriers across the junction, therefore there is no significant current flow through the junction. If an external V voltage is applied which results in reduction of the potential barrier electrons are injected into the p-side and holes are injected into the n-side and current flow occurs as reported in the picture 4.3 b). This is a positive voltage between the p-side (also known as anode) and the n-side (referred to as cathode) of the pn-junction. While the injected carriers, now as minority carriers, are moving forward by diffusion, they are recombining with the majority carriers. If, for example, the recombination process is a radiative recombination (such as a direct bandgap transition), photon emission takes place.

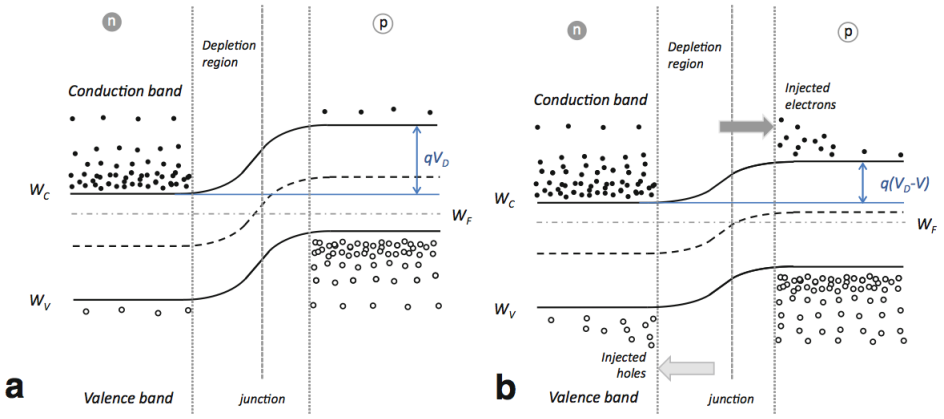

Figure 4.3: Simplified energy-level diagrams of a pn-junction. a) No current flow, b) Current flow.

The wavelength of the emitted radiation in such an arrangement is related to the bandgap of the semiconductor material making up the diode. Bandgap engineering means designing the material composition and the doping levels of a LED which will determine the properties of the emission spectra (such as the peak wavelength) and device efficiency. Nowadays there are two widely used material systems: AlGaInP (aluminum-gallium-indium-phosphide) for producing red to yellow LEDs and InGaN/GaN (indium-gallium-nitride/gallium-nitride) for building green to blue LEDs. White LEDs are typically so-called phosphor converted devices in which an LED chip with short wavelength (blue or UV) primary emission is covered by a phosphor layer which absorbs some of the short wavelength light and converts it to longer wavelength light in a wider spectral range. The fundamental physical operation of such LEDs, except the wavelength conversion process taking place in the phosphor, is the same as the operation of monochromatic LEDs [22].

4.1.2 Heterojunction Devices

A heterojunction is defined as a semiconductor structure in which the chemical composition changes with position. Heterojunctions are able to improve the performance of semiconductor devices because they permit the device designer to modify locally the energy-band structure of the semiconductor and so control the motion of the charge carriers. In the simplest case in a heterojunction two materials of different bandgaps are used.
Bandgap engineering allows the LED designer to achieve higher efficiencies in converting electric current to light than conventional homostructures. The radiative efficiency in heterostructure LEDs is higher than that of the homostructure LEDs because of the increased current injection efficiency at the heterojunction. Since

the radiative efficiency of the p-side is usually much higher than that of the n-side, higher efficiency devices are made by eliminating the minority carrier injection into the n-type material. By creating a heterostructure at the p/n interface, a valence band discontinuity is formed which provides a hole potential barrier.

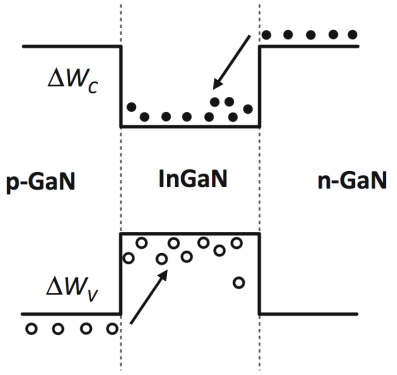

Figure 4.4: Simplified energy band diagram for a heterojunction.

The figure 4.4 illustrates the energy band diagram for heterojunction flat-band conditions where the applied bias just cancels the built-in field. The conduction band discontinuity $\triangle W_C$ and the valence band discontinuity $\triangle W_V$, produce a barrier to electron and hole flow, respectively. Due to the barrier height limitation of the bandgap discontinuity, more carriers come across the pn-junction as leakage current. On the other side, nonradiative recombination through deep energy levels at the interface will reduce the radiative efficiency and causes a potential heating at the same time [22].

4.1.3 Quantum Well Structure

If one makes a heterostructure with sufficiently thin layers, quantum interference effects begin to appear prominently in the motion of the electrons. The simplest structure in which these may be observed is a quantum well, which simply consists of a thin layer of a narrower bandgap semiconductor between thicker layers of a wide bandgap material. With advanced epitaxial techniques, the potential profile of the quantum well does not need to be rectangular. Because the band edge energy is usually linear in the composition, W_V and W_C will follow the functional form of the composition. Quantum well heterostructures are key components of many optoelectronic devices, because they can increase the strength of electrooptical interactions by confining the carriers to small regions. Basically, the electrons and holes are confined so tightly in space that their allowed states have discrete energy levels due to the localization. Recombination between such discrete energy levels results in very narrow emission spectra, characteristic to laser diodes [22].

4.1.4 Carrier Transport

In semiconductor devices, carriers move due to different physical processes. The most important ones are: diffusion, drift caused by electric field, heat-emission, and tunneling.

4.1.5 Drift Diffusion

Microscopic particles, be it molecules, atoms, or electrons, could generate diffusion movement, which is merely caused by the inhomogeneity of the density of the distribution of the particles. They will diffuse from regions of high concentration to regions of low concentration. The current in this case is called diffusion current. Carrier diffusion could happen, whether an external field is applied or not. The basic driving force of the carrier diffusion originates from the thermal energy of the majority carriers, which leads to the constant random motion of carriers [22].

4.1.6 Drift Current

When an external voltage is applied on the semiconductor, the corresponding electric field would also affect the random movement of electrons: in average they will drift along the opposite direction of the electric field. The so-called mobility is used to represent the ability of the charge carriers to be drifted by the electric field. The macroscopic electric current associated with this is called drift current [22].

4.1.7 Droop Mechanism

Droop is the non thermal roll over of the IQE at increasing driving current density. Ideally all injected carriers are consumed by radiative recombination within the QW region(s), so that current injected into the LED active region is equal to the total active region volume multiplied by the elementary charge and the the radiative recombination rate, therefore, $IQE = 1$. Main non-radiative recombination processes take actually place inside the LED active region, including Shockely-Read-Hall (SRH) recombination and Auger recombination, other secondary effect as carrier delocalization. Asymmetry of GaN LEDs makes electron leakage on the p-side of the device favored over hole leakage on the opposite side, this justifying the introduction of an AlGaN EBL interposed between the active region and the p region [23, 24].

$$IQE = \frac{Bn^2}{An + Bn^2 + Cn^3 + k(n - n_0)^m + \frac{L_{LK}}{qV_{QW}}} \tag{4.3}$$

All this considered, IQE can be expressed as 4.3 where An and Cn^3 are the SRH and Auger recombination rates, I_{LK} is electron leakage current, and V_{QW} is the active region volume. The term $k(n - n_0)^m$ accounts for the nonradiative loss mechanism associated with carrier delocalization, n_0 and k being a threshold carrier density triggering delocalization and a suitable constant, respectively, and $m \geq 2$. A sketch of carrier flows and resulting recombination and leakage terms is shown in 4.5

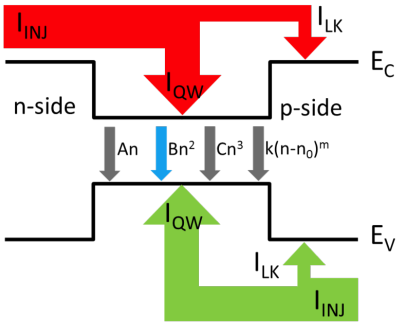

Figure 4.5: Sketch of recombination and leakage terms in a single-QW or double-heterostructure LED.

A classification of droop mechanisms is illustrated in figure 4.6. All the causes of the droop mechanism are analyzed on a model of InGaN/GaN multi quantum well device in the section 8.2.1.

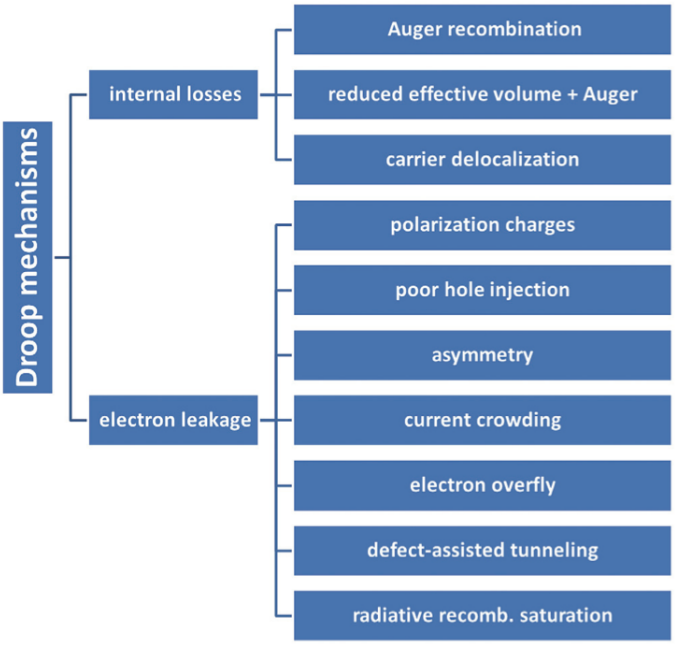

Figure 4.6: Classification of droop mechanisms.

Chapter 5

Optical Sources

5.1 State of the art

The first otical sources was born at the end of the XIX century thanks to the studies of Joseph Swan and Thomas Edison 5.1, the simplest artificial light source is the classical incandescent lamp; in it a tungsten filament electric current flows reaches (for effect Juole) temperatures of about 3000 $°C$ and becomes incandescent.

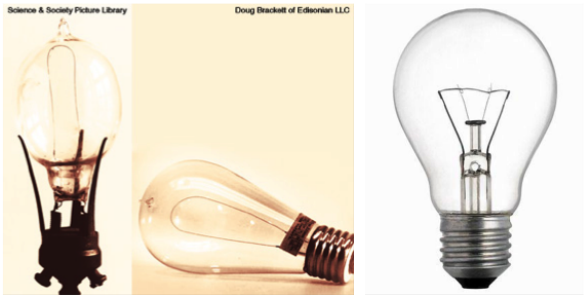

(a) (b)

Figure 5.1: a) First bulb filament lamps. b) modern tungsten incandescent lamp

It exploits the fact to obtain a Joule heating filament, until it reaches a temperature such that the spectrum of black-body contents are visible enough to illuminate 5.5; such heating involves, consequently, an increase of the electrical resistance and therefore a reduction of the current that flows there. This leads to a dynamic equilibrium in which the electrical resistance opposed by the tungsten filament to the passage of electric current assumes a stationary value which balances the power dissipated by the Joule effect. In modern bulbs the glass bulb is not empty but contains an inert gas at low pressure, usually argon, more rarely krypton. The latter allows a higher yield of about 10% at the same power. These gases reduce the risk of implosion and prolong the life of the filament. Moreover, the presence of argon/krypton reduces blackening of the bulb due to the deposit of tungsten sublimates. During

operation, the tungsten sublimates and the filament becomes thinner and thinner, until cracking generally after about 1000 hours of operation. In addition to heat, electric energy is converted to light, to an extent of about 10%; then it can be stated that about 90% of the electricity consumption is dispersed as heat [25].
An improved version of the incandescent bulb lamp is the halogen bulb, figure 5.2.

Figure 5.2: Hanogen lamp.

The gas contained in the bulb is added iodine, krypton and, sometimes, xenon to allow the heating of the filament up to more than 3000 K, in order to increase the luminous efficiency and move upward the color temperature. In the tungsten halogen which evaporates due to the high temperature it reacts with the gas to form a halide of tungsten. Subsequently the mixture, coming into contact with the hot filament decomposes and re-deposited on the tungsten filament itself creating a cycle, the halogen cycle. In this way the lifespan of a halogen lamp may be at least the double of a normal incandescent light bulb, although the filament is much hotter. Since the filament, to allow the chemical reaction between tungsten and iodine, should be maintained at a temperature of about 3000 K, the bulb is not realized with amorphous glass, as in the other incandescent bulbs, but with fused quartz, which has a crystalline structure and is resistant to higher temperatures.
The limits of these devices are related to the issue of ultraviolet rays, are harmful to the human eye and capable of causing skin cancer and cause decoloration of the illuminated objects. The phenomenon is in part due to the use of quartz instead of glass for the construction of the bulb. Quartz is indeed more resistant to high temperatures but transparent to ultraviolet rays. The shielding of these radiations is done by placing in front of the lamp a glass plate, which reduces the passage to only 15% and which also serves as protection in case of accidental explosion of the bulb. The luminous efficiency of a halogen lamp, thanks to whiter light compared to a traditional incandescent bulb, is 50-100% higher than this, while the useful life ranging from 2000 to 6000 hours [26].
A completely different technology of optical source is represented by the fluorescent lamps, the source is a discharge lamp in which the light emission is indirect, because the emitter is not the ionized gas, but a fluorescent material. It consists of a glass

tube, circular or variously shaped (for example Compact Fluorescent Lamp (CFL), which have the tube shape such as to have little encumbrance, usually integrate power electronics). The inner surface of the tube is coated with fluorescent material-looking white powder, the vacuum is produced firstly, then is introduced a noble gas (argon, xenon, neon, krypton) at low pressure and a small amount of mercury, which partly evaporates mixing with the gas. At each of the two ends of the tube it is present an electrode. The current flow between the electrode stimulate the gases to emit ultraviolet luminous radiation. The fluorescent material, hit by such radiation, emits visible light. The visible radiation, having a wavelength greater than that of ultraviolet see in figure 5.3, carries only a part of the energy transmitted from the wave ultraviolet: the remaining energy is converted into heat, which goes to heat the tube. A different composition of the fluorescent material allows to produce a warmer light, cooler light.

Figure 5.3: Fluorescend lamp.

Fluorescent lamps have an average life greater than incandescent bulbs, but their duration may be strongly influenced by the number of starts and stops, unless it uses an electronic drive: each of these operations, in fact, reduces the life of the lamp, due to the wear suffered by the electrodes for the largest number of warm-ups required. The value provided by manufacturers is generally calculated with ignition cycles of 8 hours and range from 12 to 15000 lamp hours tubular 5-6000 hours of compact lamps. The electronic drive, instead, thanks to the controlled preheating of the cathodes (electrodes), it retards the damage, allowing for a number of ignitions almost infinite (over 60000) and the precision of control extends the lives of at least 10000 hours [27].
Alternatives to filament, alogen and fluorescent lamps, are constituted by one or more LED diodes, fed by a dedicated electronic circuit, the purpose of which is primarily to reduce the mains voltage to a few volts required by the LEDs. The light is produced by a physical process in the junction of the diode, called "electron-hole recombination" that gives rise to the emission of photons, well-defined color employee by the energy released in the recombination. I am now well-established the monochromatic LEDs such as red, yellow, green and blue, and all their combinations.

Only then it was possible to produce white light LED; for example, the device MT-G Easy White, designed to replace standard MR16 halogen spotlights swhon in figure 5.4, is available in 4 shades of white, with color temperatures from 2700 to 4000 Kelvin, the most recent MK-R, with a yield of 200 lumens per watt is available in 6 shades of white. White light can also be obtained by mixing the output of RGB LEDs, devices that are built around the year 2000, comprise three junctions light emitting green, blue and red; in this case, white light is obtained by addition of the three primary colors. Alternatively, a blue LED is coupled with a layer of phosphors that emit yellow light and the combination of the respective emission spectra also produces in this case an effect of white light, this devices are based on GaN chip LED.

Figure 5.4: One of the first model of LED lamp.

Unlike incandescent bulbs, which end their lives with the burning of the filament, LEDs degrade slowly, with a loss of brightness that comes down to 20-30%. From an economic point of view the LEDs are more expensive than filament bulbs, but the duration of operation of an LED, which is around 50000-80000 hours, is well above the life of a traditional bulb. From the energy point of view, LEDs are much more efficient than filament bulbs, since 50% of the energy absorbed produces illumination and therefore the amount of energy wasted in the form of infrared radiation and heat released into the environment is very reduced compared to traditional lighting technologies [28].
In the figure 5.5 are shown the emission spectrum of the sources described, compared with the day-light sun radiation. The spectra reported in the figure refers to visible range optical frequencies only. The spectrum can be significantly different from source to another, it is important to know the optical characteristics of these devices for the visual safe lighting.

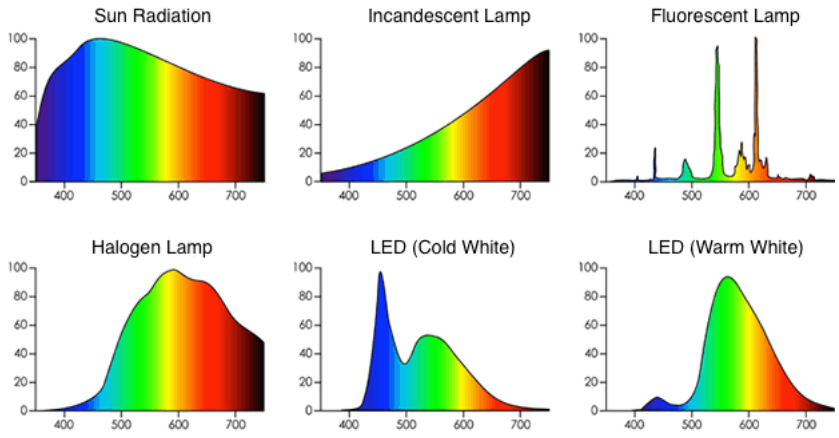

Figure 5.5: Spectrum, in the visible range, of the sources described campared with the sun day-light.

5.2 Application Field

The Directive 2005/32 / EC (in Europe, EISA 2007 in USA) defines the structure with which the company establishes the *ecodesign* requirements for energy-using products (EuP) The directive update with 2009/125/CE establishes minimum requirements for domestic lighting. Basically from September 1, 2009 will no longer be carried out before placing on the market within the European Union, the lamps with high power consumption for use in the home environment. This is in line with plans for climate protection in the EU; incandescent lamps will no longer be available gradually by 2012. The directive sets exactly when and what types of bulbs can no longer be placed on the market and relates more to the traditional incandescent lamps. For example, from September 1, 2009 it will no longer be introduced in the market with bulb lamps diffusing, except for energy saving lamps (CFLi) in energy efficiency class A. From that date also will be banned incandescent lamps with a power equal to or greater than 80 W. The Directive also establishes new requirements for the packaging and quality requirements for the benefit of European consumers.

After the directive the introduction of new light sources was necessary and natural , in particular sources with high energy efficiency which the LEDs have been strongly introduced into the market. As the figure 5.6 shows applications in which the LED device is employed are many.

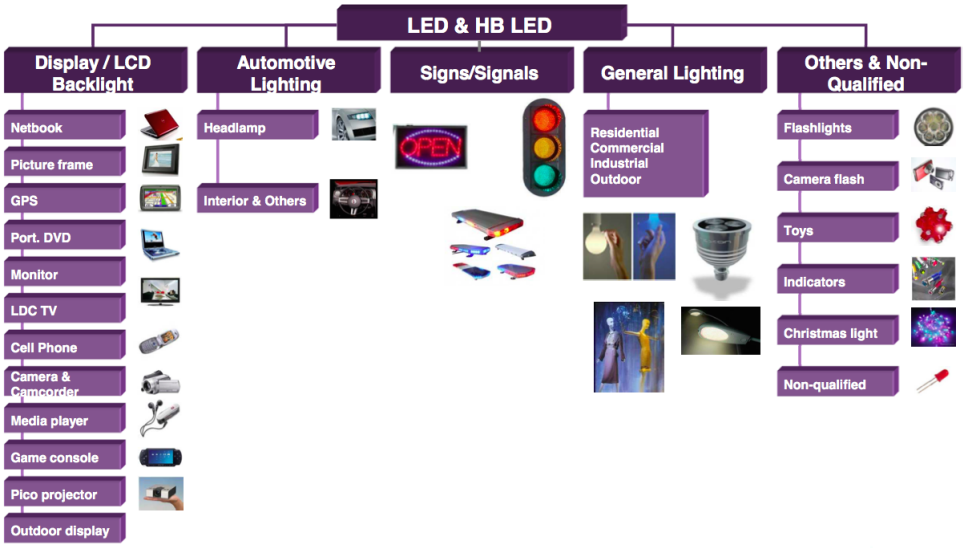

Figure 5.6: Overview of LED applications.

As the picture shows 5.6 the main applications where the LED technology has been strongly introduced are:

- *Display LCD / Backlight*
- *Automotive Lighting*
- *Signs/Signals*
- *General Lighting*
- *Others & Non-Qualified*

5.2.1 Display LCD / Backlight

LCD displays are used in a variety of devices that can be divided in large (TVs, desktop monitors...), medium size (laptops, tablets, netbooks, photo frames, portable DVD displays...) and small size (cell phones, digital cameras, portable game consoles, navigation devices (GPS)..).

Figure 5.7: A LED TV of 6.5 mm thickness.

The LEDs for thais application are used as the light source for the Backlight Unit (BLU) of a Liquid Crystal Display (LCD), for example the called LED TVs, see figure 5.7 are therefore just regular LCD TV using an LED based backlight instead of the traditional Cold Cathode Fluorescent Lamp (CCFL). The LEDs bring on that devices potential benefits:

- *energy efficiency*
- *mercury-free light source*
- *Form factor (thin displays)*
- *Local dimming*
- *Others & Non-Qualified*

5.2.2 Automotive Lighting

The automotive marked is a field of application where the LEDs found place, the main parts where the LED is installed are the headlamp, the interior of the car or the back light for example as the figure 5.8 shows.

Figure 5.8: Back light of a car.

The benefits are a fast response of the parts, that can be interpreted as security, reliability as a warranty, lower volume respect to the old sources results a gain in space in the car and finally the flexibility of the LED that is an added value as style.

5.2.3 Signs/Signals

Is important to reduce the cost of the energy by saving it in cities and big metropolis. The LEDs can help to achieve this goal. The figure 5.9 shows two examples of LED introduction. The LED leads to a drastic reduction of the consumption of energy both for private citizen than public lighting, a great reduction of the total cost of energy. Even if the cost of the device is not yet optimal the total cost of the energy is lower than by using the old optical sources.

(a) (b)

Figure 5.9: a) LED Signs on a shop . b) Traffic light implementing LED technology

5.2.4 General Lighting

The normatives banned old technology the optical sources as explained above, the figure 5.10 shows such a strong expansion of the application for general lighting and the LED will still expanding. The new solid-state sources are and will be increasingly present in the home, work and outdoors. The objective is to lead to a lower consumption of energy and thus to energy savings on a large scale.

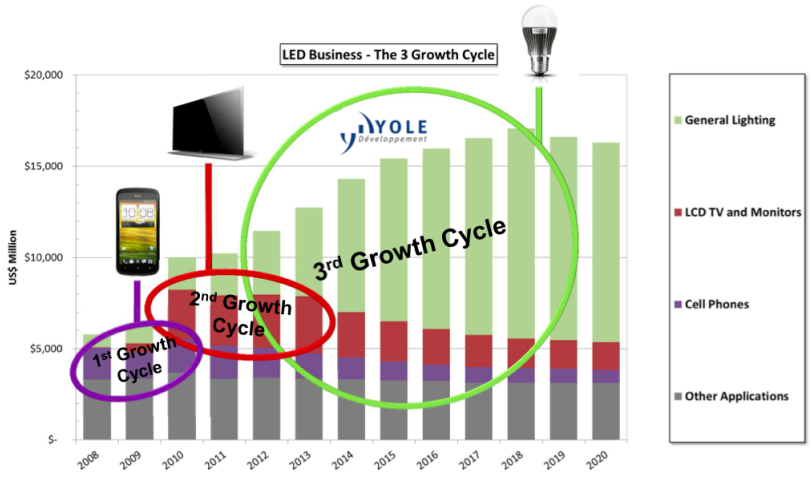

Figure 5.10: LED business and application.

The present situation is characterized by a highly fragmented application market with different drivers for adoption and wide variety of technical requirements depending on the application and location. This situation open the view on two different LED adoption paradigms LED bulb replacements (replacement/retrofit) vs. dedicated LED solutions (new Installations).
It is very important to evaluate and know the characteristics of the light emitted from this new solid state sources, now because it is already in place a strong introduction of these sources in the workplace, at home as well as for the public lighting, to protect the human being from any risk that may afflict the human visual system and even the biological rhythms that regulate our body, circadian rhythms. As well as the light emitted, it is also important to know the parts of the commercial LED light bulb is realized, specifically the GaN LED chip and the electronics dedicated, power supply, of this device. Depending on the luminous power exists dedicated drivers, designed with specific architectures depending on the final application. Is important to study this aspect of the solid state sources, as will be introduced successively, any electrical disturbance that is located in the private or industry net supply can be transferred via the converters and generate optical noise, if the driver is not properly implemented, bringing annoyance and disturbs the human visual apparatus.

Chapter 6

Human Visual System

6.1 Anatomy and function

The human eye is a complex organ able to give a big amount of information about surroundings than all other senses combined. Its structure is remarkable, not only for what it can do, but also because the eye is the only part of the body with semi-direct access to nerves and tiny blood vessels that can be seen directly, and by its inspection it is possible to provide important clues about the health of the entire body. Like a camera, it is able to refract light and produce a focused image that can stimulate neural responses with the specific task, the ability to see. It is essentially an opaque eyeball, shown in figure 8.84, filled with a water fluid-like. In the front of the eyeball is a transparent opening known as the cornea. That is a thin membrane that has the dual purpose of protecting the eye and refracting light as it enters the eye.

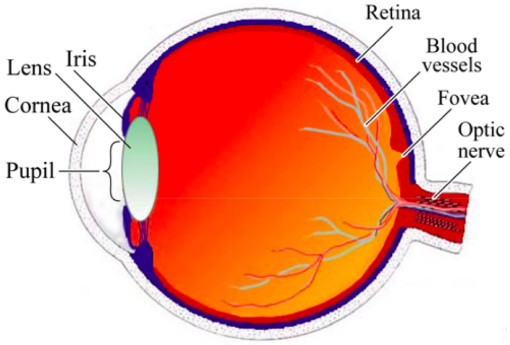

Figure 6.1: The human eye.

After light passes through the cornea, a portion of it goes through an opening known as the pupil. Rather than being an actual part of the eye's anatomy, the pupil is merely an opening. The pupil is the black portion in the middle of the eyeball.

Its black appearance is attributed to the fact that the light that the pupil allows to enter the eye is absorbed on the retina (and elsewhere) and does not exit the eye. Like the aperture of a camera, the size of the pupil opening can be adjusted by the dilation of the iris. The iris is the colored part of the eye; it is a diaphragm that is capable of stretching and reducing the size of the opening. In bright-light situations, the iris adjusts its size to reduce the pupil opening and limit the amount of light that enters the eye. Also, in dim-light situations, the iris adjusts so as to maximize the size of the pupil opening and increase the amount of light that enters the eye. Light that passes through the pupil opening, will enter the crystalline lens. This one is made of layers of a fibrous material that has an index of refraction of roughly n = 1.40. Unlike the lens on a camera, the lens of the eye is able to change its shape and thus serves to fine-tune the vision process. The lens are attached to the ciliary muscles which relax and contract in order to change the shape of the lens. By carefully adjusting the lenses shape, the ciliary muscles assist the eye in the critical task of producing an image on the back of the eyeball. The inner surface of the eye is known as the retina. The retina contains the rods and cones that serve the task of detecting the intensity and the frequency of the incoming light. An adult eye is typically equipped with up to 120 million rods that detect the intensity of light and about 6 million cones that detect the frequency of light. These photoreceptors send nerve impulses to the brain, that travel through a network of nerve cells. There are as many as one million neural pathways from the rods and cones to the brain. This network of nerve cells is bundled together to form the optic nerve on the very back of the eyeball. The dimensions of the eye are reasonably constant, varying among normal individuals by only a millimeter or two; the vertical diameter is about 24 mm and is usually less than the transverse diameter. At birth that diameter is about 16 to 17 mm; it increases rapidly to about 22.5 to 23 mm by the age of three years; between three and 13 the globe attains its full size. The weight is about 7.5 g and its volume 6.5 mm^3 [29]

6.2 Pupillary Light Reflex

This chapter will describe the human visual system mainly focused ini the *Pupillary Light Reflex* (PLR). The first section will introduce the *Pupillary Light Pathways*, followed by the analysis of the *Pupillary Light Reflex Arc*. The main components of the PLR are reported: the *Retina*, the *Autonomous Nervous System* and the *Iris Muscle Plant* explained focusing on the pupil light reflex functionality.

6.2.1 Pupillary light reflex pathways

Pupillary light reflex (PLR) is the iris response to changes in the intensity of light incidence on the retina. There are a visual photo-transduction and a non visual one. This reflex is autonomic, cranial, parasympathetic-mediated. As the picture 6.2 both eye are interconnected, if one is stimulated by a light stimulus, also the dimension of the other pupil will be influenced, even in resting condition without stimulus.

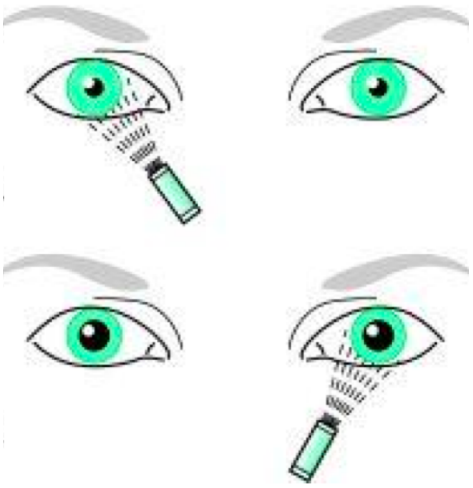

Figure 6.2: The reference device for the droop efficiency simulations.

In order to better understand where this reflex is used, it's important to comprehend its mechanism. The PLR is not a reaction related only with the eyes, but on this effect specific parts of the nervous system is involved. As the picture 6.3The light that travel in the eye impact on the first surface thet is composed by the sensory receptors, which are localized in the retina of the eye. The photoreceptors converts the optic to electric signal that through the sensory fibers is guided by the optic nerve (the second cranial nerve) to the brain. The signal is elaborated by the integration center in the central system, in the midbrain. The next part of the nervous system is represented by the motor fibers to the muscle in the iris that constricts the pupil, neuronal projection that belongs to the oculomotor nerve (the third cranial nerve): pupil constriction is the parasympathetic response. The response feedback of the elaborated signal travel back to the effector, the muscles in the iris . The pupil is the round black circle at the center of the iris of the eye, through which light passes, the size is determined by the antagonist activity of two smooth iris muscles: the *sphincter pupillae* and the *dilator pupillae*. Looking more closely to the main nuclei and brain parts involved, it is necessary to describe the axonal projections of the reflex. First of all, the retinal ganglion cell of the eye receives inputs from rods and cones, by setting the photo-transduction. The axon projects in the pretectal

nucleus, located in the midbrain, and here innervates two outputs directed to both side of the brain, one for each side: the first one is directed to the Edinger-Westphal nucleus, located in the ipsilateral side of the midbrain, where synapses with the ciliary ganglion; the second one is directed to the contralateral portion of the body. The nerve fiber that project from the ciliary ganglion is directed to the homolateral muscle of the iris. This cranial light reflex arc results in pupil constriction. Checking the reflex is like looking at the complete pathway.

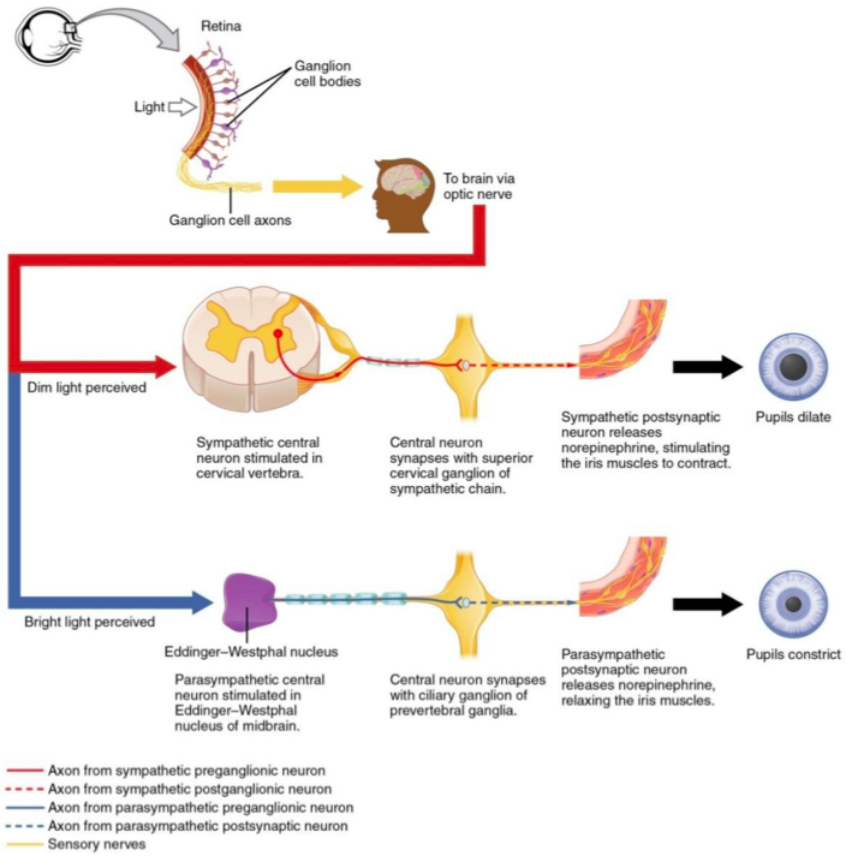

Figure 6.3: Representation of sympathetic and parasympathetic pathways in the pupillary light reflex.

6.2.2 The pupillary light reflex arc

The three main components of the pupillary light reflex will be described more in detail in the following paragraphs, in the specific:

- *Retina*
- *Autonomous Nervous System*
- *Iris Muscle Plant*

The Retina

The photoreceptors are very specialized sensory neuron cells, are able to acquire information and convert it into electric impulses. The photoreceptors are a fundamental part of the retina, that can be divided in *rods* and the three types of *cones*, each of the cone is sensitive to specific band of optical frequencies in the visible range.
The rods take their name from the shape in which they are observed through microscope, a long cell body with a rod shape. Inside a rod there are bunches of structures known as optic disks, large membrane-bound structures, which are connected with lots of Rhodopsin, proteins that are able to actually absorb the light (in a certain range of wavelength, see section 6.2.2) and begin the phototransduction that eventually leads these rods to fire an action potential that will reach the brain. Similarly the cone, its name because is cone-shaped, are also photoreceptors that are specialized neurons, the internal structure is the same as rod, but the protein involved is known Photopsin. As the ray light enters the eye, if it happens to hit the rod Rhodopsin, could start the phototransducion cascade that results in firing of an action potential; the same happens if the ray light reach the cones. The first difference of the two photoreceptors is the population: the number of rods is of about 100 million, but on the contrary, cones are about 5 million in the retina.

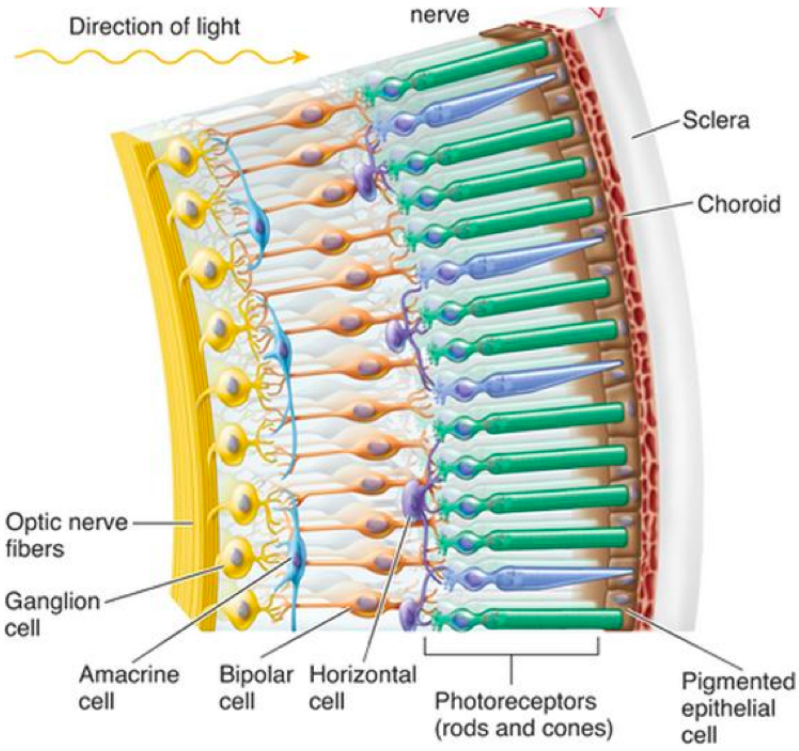

Figure 6.4: Distribution and arrangement of the photoreceptors in the retina.

Where the photoreceptors are located is another big difference: the rods are located mostly in the peripheral area of the retina, although the cones are primarly concentrated near the fovea region. Additionally, rods are 1,000 more sensitive to light than cones, and are implicated in the *scotopic vision*, because they are more specialized in detecting light and whether it is present. The rods are responsible for a gray scale vision and are saturated (excessively stimulated) and so non-functional even in ordinary house illumination conditions. They usually are able to respond to electromagnetic waves until 55 Hz. On the other hand, cones result in colored vision: they start to response to a dim light, such as the light of the stars in the night, and fully and exclusively works in day light, resulting in *fotopic vision*. They are able to respond to a beam of light at low intensity, and cannot exceed 12 Hz of frequency. There are 3 types of cones which we will refer to as the short-wavelength sensitive cones, the middle-wavelength sensitive cones and the long-wavelength sensitive cones respectively known as S-cone, M-cones, and L-cones. In primates, short wavelength sensitive cones (S cones) and medium- or long- wavelength-sensitive cones (L/M cones) are two separate populations. Each cone type has a different developmental timecourse, contributes to different intra-retinal circuits, and transmits different types of information to the brain. This can partially be explained by the different nature that s-cones express, due to evolutionary reasons : first of all, the S cone's sensitivity curve (with peak at 437 mm) is very different from the sensitivity curves of the L and M cones which are quite similar with their peaks very close to each other (at 564 mm and 533 mm respectively) and overlap over a wide range of the visible wavelengths. Secondly, the population of the S cones is much smaller than that of the L or M cones, constituting only about 10% of the overall cone population, while the remaining 90% are L and M cones, with 2 to 4 times more L cones than M cones. Finally, S cones are totally absent in the foveal area (and so are the rods) where there is a high concentration of M and L cones.
For the greater part of 150 years it was assumed that the mammalian retina contained only two types of photoreceptors; rods and cones. However, a flurry of recent evidence has demonstrated the existence of a third type of mammalian photoreceptor that differs greatly from rods and cones. This type utilizes a different photopigment, is much less sensitive to light, and has far less spatial resolution; characteristics that fit perfectly with this photoreceptorś primary function of signaling changes in ambient light levels to the brain throughout the day. Most surprisingly, these non-rod non-cone photoreceptors are *ganglion cells*, and thus, have the unique ability to communicate directly with the brain. These intrinsically photosensitive retinal ganglion cells (*ipRGCs*) are a rare sub-population of ganglion cells (1-3%) whose primary role is to signal light for unconscious visual reflexes, such as pupillary constriction, but also regulating a number of daily behavioral and physiological rhythms, collectively

called *circadian rhythms*. This latter process, which adjusts circadian rhythms to the light/dark cycle of an animalś environment, is known as photoentrainment. This can be observed in blind patients that have lost image vision owing to rod/cone degeneration, but can still be photoentrained due to the preservation of their ipRGCs. The pupillary light reflex (PLR) allows reducing the rod and cone saturation by light, and improves resolution by increasing the depth of field .The pupillomotor information conveyed to the midbrain may nevertheless derive indirectly from the outer retina (rod and cone activation) or directly from within the inner retina (melanopsin activation due to the ipRGCs, the spectral sensitivity of the photoprotein is of about 480 nm).

Spectral Sensitivity

As explained in the previous section 6.2.2 there are three cone photoreceptors types in human retinas. This three types of cones have differential sensitivity to short, medium, and long, wavelengths, and the presence of the three types of cone photoreceptor makes human trichromatic color vision. While the vision is dichromatic when there are only two types of color sensitive sensors, as in some color blind humans. The spectral sensitivities of these photoreceptors have been determined by Schnapf [30], using suction electrodes to measure cone photocurrent directly. The fundamentals are three smooth functions of wavelength peaking at 440 nm (S cones), 530 nm (M cones) and 560 (L cones)[31]. Human sensitivity to light across the visible spectrum under photopic, daylight conditions is called the photopic luminosity function, denoted V_λ. There are different methods to measure this function, for example based on the heterochromatic flicker photometry which consist in exciting the eye with a white light at a frequency of 20 Hz or above, another approach is to measure it by using contour distinctness and minimal motion as response criteria. The luminance of a light source is its effectiveness in stimulating the visual neural mechanism that has its spectral sensitivity the photopic luminosity function,thus, the luminance of any light may be computed by multiplying its spectral radiance distribution, wavelength by wavelength , by the photopic luminosity function and summing the products from all the wavelengths. The spectral sensitivities of the M (530 nm) and L (560 nm) cones and the photopic luminosity function are graphed in figure 6.5 from [31].

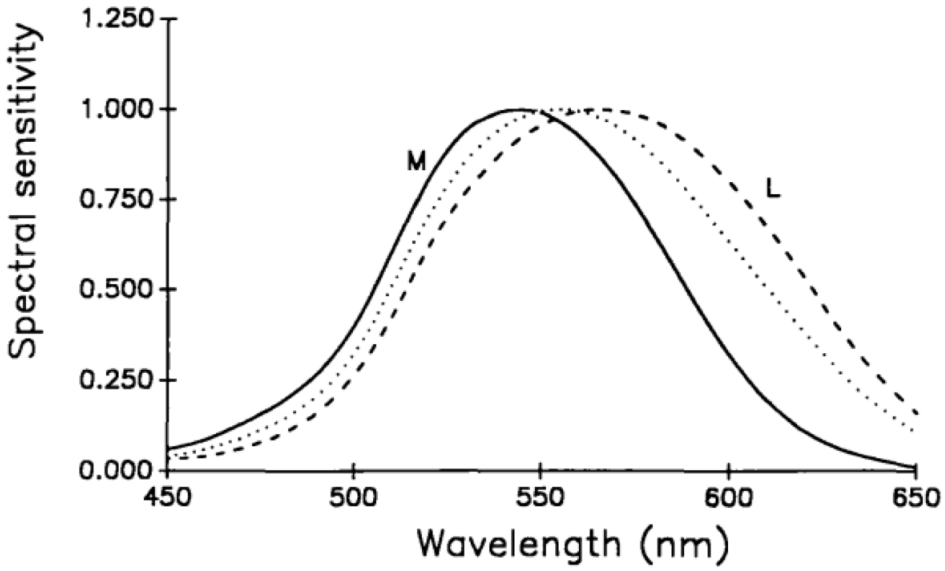

Figure 6.5: The photopic luminosity average curve of statistically significant population.

The purpose of this graph is to show the degree of overlap of two longer wavelength cones with the photopic luminosity function, and also to demonstrate the closeness of the luminosity function to the L cone sensitivity especially at longer wavelengths. The spectral sensitivity of a mammalian photoreceptor is determined by a protein coined as opsin that the photoreceptor expresses. After absorbing a photon, the photopigment undergoes photoactivation and bleaches to opsin and all-trans-retinal, in other words the photopigment optically decolorizes with a reduced optical density. The spectral sensitivity of this compound is determined by the sequence of amino acids that make up the opsin protein. An inexpensive LED-based five-primary photostimulator that can control the excitations of rods, S-, M-, L-cones, and melanopsin-containing ipRGCs in humans at constant background photoreceptor excitation levels was developed for studying the adaptation behavior of ipRGCs with rod, cone, or melanopsin input [1], and the spectral sensitivities described in figure 6.6 will be used to model the photoreceptors response in the section 8.4.3.

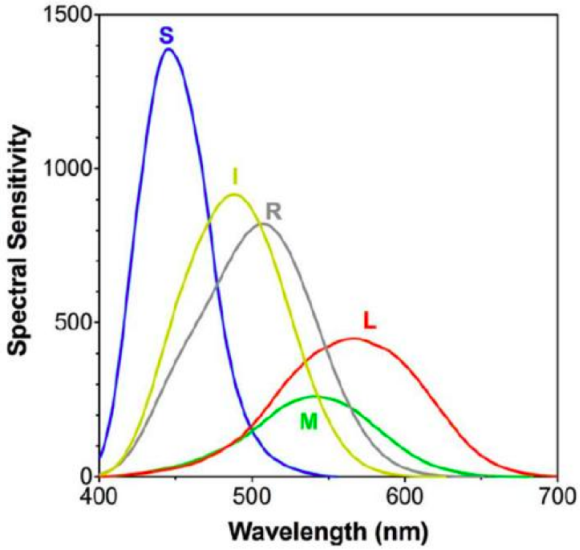

Figure 6.6: Spectral sensitivities of the five types of photoreceptors [1].

Eye responsitivity

The responsivity of the rods and cone photoreceptors is quite different. As the figure 6.7 shows the vision, scotopic or photopic, is activated depending on the amount of light respectively for the rods and cones. When different wavelengths of light are employed for measuring the threshold, it is found, for example, that the eye is much more sensitive to blue-green light than to orange. The interesting feature of this kind of study is that the subject reports only that the light is light; he distinguishes no color.

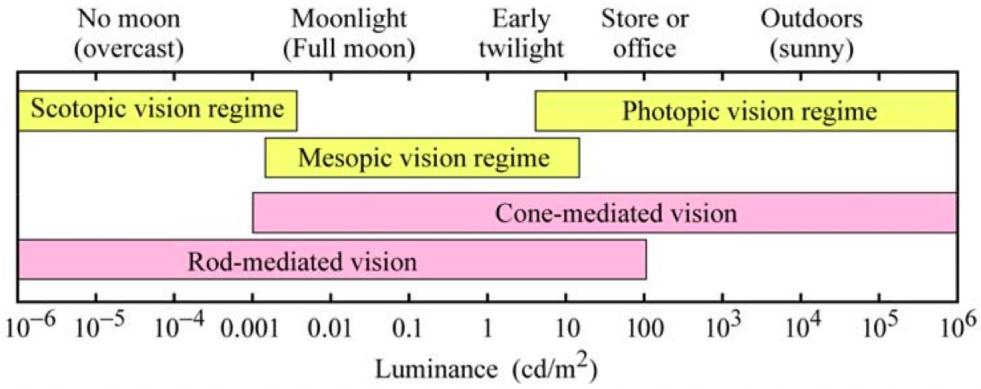

Figure 6.7: Vision regime of the human eye.

If the intensity of a given wavelength of light is increased step by step above the threshold, a point comes when the subject states that it is colored, and the difference between the threshold for light appreciation and this, the chromatic threshold, is called the photochromatic interval. This suggests that the rods give only achromatic,

or colorless, vision, and that it is the cones that permit wavelength discrimination. The photochromatic interval for long wavelengths (red light) is about zero, which means that the intensity required to reach the sensation of light is the same as that to reach the sensation of color. This is because the rods are so insensitive to red light; if the dark-adaptation curve is plotted for a red stimulus it is found that it follows the cone path, like that for foveal vision at all wavelengths.

Color exchange and equilluminance

Color exchange, or silent substitution, the concept is a technique for identifying contributions from photoreceptors or other spectral response mechanism [32]. For any spectral sensitivity function, and two light sources with different spectral distribution within the band of the band of the sensitivity function, one can perform a color exchange experiment that will provide a characteristic color balance for that spectral sensitivity.

6.2.3 The autonomic nervous system

Furthermore, in the absence of a documented disorder of the peripheral components of the ANS, the alterations of the pupil size can be used for the assessment of the ParNS and the SNS neurotransmitters function, i.e. Acetylcholine (Ach) and Noradrenaline (Nor) respectively, within the CNS . In accordance with the CNS integratory mechanisms that govern the PLR, Yamaji et al have divided the characteristic V-shaped response into three segments, a primary that is due exclusively to ParNS excitation, a middle that is attributed both to the SNS and the ParNS and a latter that reflects only SNS activity. The dilator muscle of the iris is activated by sympathetic nerve fibres. Stimulation of the sympathetic nerve in the neck causes a powerful dilation of the iris; again, the influx of adrenalin into the blood from the adrenal glands during extreme excitement results in pupillary dilation. Many involuntary muscles receive a double innervation, being activated by one type of nerve supply and inhibited by the other; modern experimentation indicates that the iris muscles are no exception, so that the sphincter has an inhibitory sympathetic nerve supply, while the dilator has a parasympathetic (cholinergic) inhibitor. 6.8

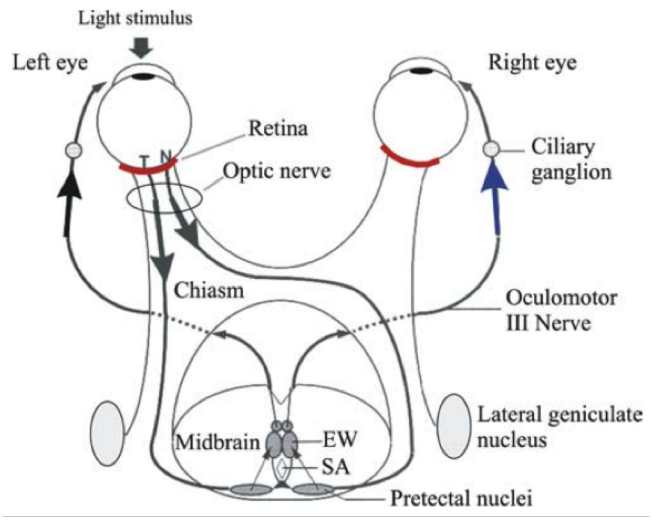

Figure 6.8: Vision regime of the human eye.

Thus, a drug like pilocarpine not only activates the constrictor muscle but actively inhibits the dilator. A similar double innervation has been described for the ciliary muscle. In general, any change in pupillary size results from a reciprocal innervation of dilator and constrictor; thus, activation of the constrictor is associated with inhibition of the dilator and vice versa. The constriction and dilation of the pupillary aperture is produced mainly through Autonomic Nervous System (ANS) control exerted on the muscles of the iris. More specifically, neurons of the Parasympathetic Nervous System (ParNS) innervate circular fibers of the iris, causing pupillary constriction, also known as myosis, whereas excitation by Sympatethic Nervous System (SNS) neurons causes the radial fibers of the iris to produce dilation of the pupil, response called mydriasis, figiure (6.9. The circular muscle fibers are also termed the sphincter pupillae, and their parasympathetic innervation begins at a group of brain cells located in the midbrain, Edinger-Westphal nucleus (EW). The efferent parasympathetic fibers travel from this nucleus, along the oculomotor nerve (third cranial nerve), to the ciliary ganglion near the eyeball, and finally to the smooth muscles surrounding the pupil. The radial fibers, also termed the dilator pupillae, are under control of SNS processes originating in the hypothalamus. From here fibers project downward to the spinal cord (lower cervical and upper thoracic) and leave the cord to synapse the superior cervical ganglion. Sympathetic influence projects from this ganglion directly to the dilator pupillae of the iris. The ANS is intimately involved in emotional behavior. A strong emotional stimulus will cause the pupils to dilate. Thus, a dilated pupil will appear as part of a startle reaction with a response occurring in as little as 0.2 s and peaking in 0.5 to 1.0 s. The dilation will persist even if a bright light is presented to the eye, indicating that

the emotional response can override the usual pupillary constriction to intense light stimuli. Animal studies have shown that pupillary dilation occurs with stimulation of the hypothalamus, thalamus, and reticular formation.

6.2.4 The iris muscle plant

Pupillary size reflects a balance between two opposing muscle groups located in the iris as in figure 6.9. Pupil constriction is due to the increased tension in the papillary constrictor. The papillary constrictor muscle is circularly arranged and is innervated by the parasympathetic nervous system, and the motor nucleus, called the Edinger-Westphal nucleus, located in the midbrain.

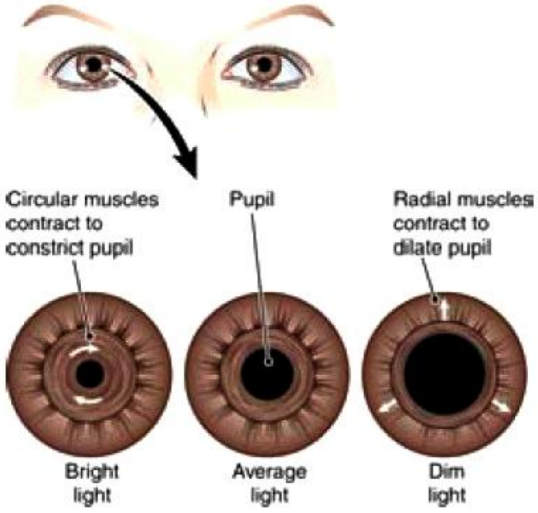

Figure 6.9: The iris muscle plant.

There are two mechanisms for papillary dilation: first one is *active* reflex dilation, which is due to contraction of the papillary dilator; the second one is conversely *acive* and is due to the inhibition of the activity of the Edinger-Westphal nucleus. The papillary dilator muscle is radially arranged and is innervated by the sympathetic nervous system.

6.2.5 Accomodation

The image of an object brought close to the eye would be formed behind the retina if there were no change in the focal length of the eye. This change to bring the image of an object upon the retina is called accommodation. The point nearer than which accommodation is no longer effective is called the near point of accommodation. In very young people, the near point of accommodation is quite close to the eye, namely about 7 cm in front at 10 years old; at 40 years the distance has increased

to about 16 cm, and at 60 years it is 100 cm or 1 m. Thus, a 60-year-old would not be able to read a book held at the convenient distance of about 40 cm, and the extra power required would have to be provided by convex lenses in front of the eye, an arrangement called the presbyopic correction. It is essentially an increase in curvature of the anterior surface of the lens that is responsible for the increase in power involved in the process of accommodation.

6.3 Pupillary Light Reflex Models

Since 1956 there was the intention to comprehend deeply the human visual system, for this purpose the researcher starts to design an analitical models, for the quantitative modeling of the complex human pupillary light reflex (PLR) phenomenon, various mathematical approaches have been used, the aim for modeling the PLR responses is helpful for understanding the mechanism of the pupil system. The pioneering work designed the pupil mechanism as a servocontrol system and analyzed using linear servoanalytic approaches [33]. Later on the studies proceed based on the Stark completing the model with the addition of analytical approaches for the stability and oscillations principle and application on the pupillary movements [34, 35, 36]. In figure 6.10 it can be observed the original scheme proposed by Stark for describing the PLR in 1956 and it represents the first model of the PLR.

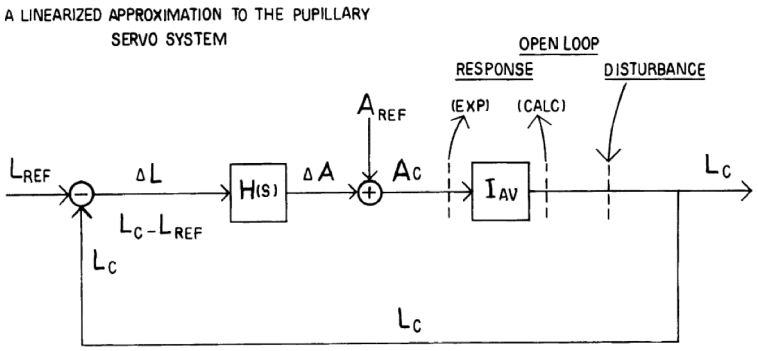

Figure 6.10: A simple servosystem resembling the pupillary light reflex.

The amount of light flux falling on the retina is the controlled quantity (L_c). A reference light flux quantity (L_{ref}) exists which is compared with actual light (L_c) falling on the retina. Any difference or error ($L_c - L_{ref}$) which occurs is measured, and it is this quantity which actuates the control system, or pupil neuromuscular apparatus. The control system then operates, varying pupil size and so changing controlled light (L_c) to reduce error. Similar control theory-based approaches were also used to model the nonlinearities of the pupillary responses. Although these control models provided valuable insight into the potential neural circuit governing

PLR, the associated transfer functions are difficult to be converted into closed-form equations and have limited applications in the interpretation of the pupil behavior. Essentially the model implemented is based on the linear system identification theory, the PLR systems are well approximated by the third order linear transfer function and the oscillation frequency of change in the pupil diameter under the high gain condition can be predicted by its Nyquist diagram. Some years later the model is treated as a nonlinear PLR system [37]. Stark give the developments in control theory and in research into biological control systems have occurred in those years allowed to apply to solve the system: optimal control theory, Liapunov stability methods, Wiener-G functional analysis, general systems identification procedures and pattern recognition techniques for adaptive systems have influenced experimental approaches to a wide variety of neurological control systems. It was purposed an intensive reinvestigation using classical electrophysiological techniques to define interesting design features of the underlying neurophysiological mechanisms of these systems to obtain better results and more accurate models.
In the conclusions of this article he said that linear transfer function studies such as those reviewed in 1959, but not discussed in Stark paper, are excellent starting points because of the great engineering theory and practice introduced in this field. It can be said that certain systems have "essential" non-linarites and a linear approach will be misleading rather than helpful. In fact, for the pupillary system this turned out to be a rather fortunate and appropriate method since the final neuromuscular plant so dominates the behavior of the system as regards the classical feedback phenomenon of stability and the generation of instability oscillations. The control theory-based approaches were also used to model the non-linearities of the pupillary responses, the control models provided valuable insight into the potential neural circuit governing PLR [38, 39].
Stark worked for many years on the modeling of the pupillary light reflex and also collaborated with many researchers in this field [40]. The last article about the PLR that uses this approach is a Simulink model created as shown in 6.11

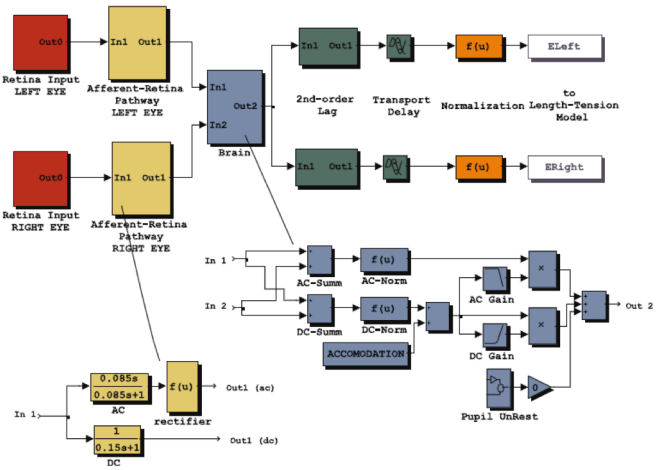

Figure 6.11: Binocular Simulink Model.

This model represents blocks with a classical control engineering approach. The pupil model is divided into three main compartments: the two afferent retinal pathways are separated (left and lower-left inset) and they both implement logarithmic response to the light and *AC rectifier effect*, as well as the DC and AC modules. Light stimuli can be applied to both pathways simultaneously or in alternating fashion. The midbrain ocular motor complex (Brain module in the center lower-middle inset) implements the pupil size effect and combines together the AC and DC dynamic components. The pupil noise is added to the system before the efferent oculomotor bifurcation. The oculomotor III nerve efferent pathway, one for each eye, has a second-order lag block and transport delay modules and continues to the final length tension non-linearity. Specific melanopsin block has been excluded from the model, and the authors hypothesize that the description of melanopsin dynamics could lead to a different or more elaborated definition of the PSE mechanism. Furthermore, the gain control operator is thought to be defined in the Brain block generally enough, and it could be functionally extended to interpret different retinal contributions to the PSE non- linearity. Alternatively, a third melanopsin input could for example be added in parallel to the AC and DC channels.
Many other models could be found in literature that describe the PLR. As being a complex system, there could be chosen black box approaches or models which are focused on certain aspects or details. A nonlinear first-order delay differential equation to generate the autonomous oscillations under *high-gain* negative-feedback conditions is proposed [41, 42, 43] . However, the PLR responses generated from this model were not consistent with the observed data, by considering the membrane potential of the retinal ganglion cells to improve the calculated pupillary responses to sinusoidal inputs a ameliorate model was designed [44]. Recently, Pamplona et al. further modified the model by incorporating an empirical function describing

the dependency of average pupil size on ambient illuminance [45]. However, no first-order differential equation-based model could produce realistic transient PLR profiles induced by short-pulse optical stimulation.
An entirely new PLR model based on a homeomorphic biomechanical model of the pupil muscle plant was proposed in the 90's by Usui and Hirata [46]. The constrictor and dilator were modeled using the same basic mechanic units including an elastic element, a viscous element, and an active contractile element. as the figure 6.12 shows. The model ensures consistent results with the observed data and was used to monitor autonomic nervous activity.

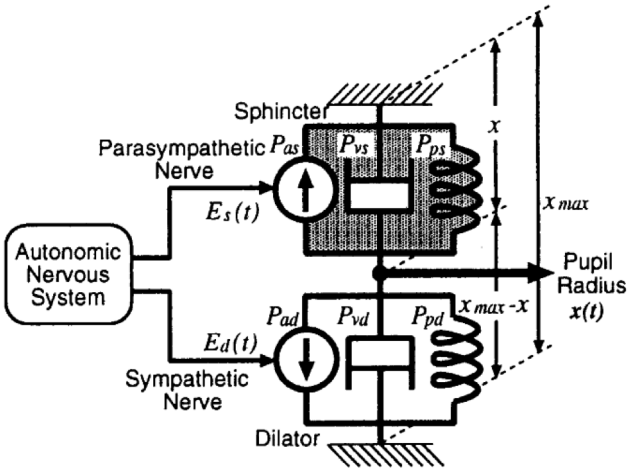

Figure 6.12: The muscle plant modelled by Usui nad Hirata.

However, this model was overly complicated because of a total of 19 equations. Even with all dependent equations being combined, the model still consisted of three independent second-order delay differential equations. Therefore, it was impractical to design a robust inverse algorithm to obtain model parameters from experimental data. But this model will be very used for the high number of experimental data which will be very useful for modeling the muscle plant or the autonomous nervous system with some procedures that will be explained in the dedicated chapter.
A recent model was introduced that purpose a mathematical model that can describe short-light-flash-induced transient pupillary light reflex (PLR) and extract autonomic nervous system (ANS) inputs from measured pupillograms [47]. The complex system introduced by Usui and Hirata was reduced in a dynamic equation for constrictor and dilator and the passive iris muscle elasticity was modeled as a second-order equation of muscle length based on experimental observation. Viscous resistance in the constrictor and dilator modeled as a linear function of velocity.

Chapter 7

Physiological effects related to artificial light

The importance of the PLR for diagnosis and its utility is illustrated in this section. Several studies demonstrate that by the study of the pupillary reflex an effective diagnosis can predict several diseases, related with the human body. A brief overview of the PLR model state of the art is proposed of the last decades by the researchers.

7.1 Importance of PLR

Since ancient times, the medical practice has paid great attention to the messages and the meanings channeled thought the eyes, in fact the ladder were considered the mirror of overall health conditions. Frequent pupil evaluation is today more than a ever a part of the protocol for care of the critically injured or ill patient. The pupillary light reflex (PLR) and pupil size have been traditionally used as a clinical parameter and as a prognostic indicator [48]. The pupillary light reflex (PLR) is a valuable objective test used to evaluate visual function. It provides information about the integrity or not of the afferent and efferent pathways starting from the retina. In the absence of a documented peripheral disorder, the pupil's reaction to light may be used to assess Ach and Nor function in the central nervous system (CNS) [49]. Assessment of the pupil reflex has been used in modern biomedical research to study any possible deficit that may occur in the pupil mobility in: alcoholics, diabetic patients, Down syndrome, depression, generalized anxiety disorder, drug abuse, mental retardation, Alzheimer disease[50], Parkinson disease, cognitive and emotional process [51], fatigue, and to elucidate the mode of action of specific anti-depressants [52].
Ophthalmologists and researchers use an infrared pupillometer to measure the size of the pupils. The device consists of a large camera tuned for infrared detection and

two infrared side lamps for pupil illumination. The physical examination of pupil size is a non-invasive clinical exam, that could easily reveal many clinical underpinning conditions [53]. Looking at papillary reaction, in size and shape, to both bright light and dim light, as well as testing the reaction to near stimuli, such as small print, could lead the clinician to a preliminary clinical suspicion.
The largest aberrations in human eyes are defocus and astigmatism, followed by the aggregate effect of all the remaining, higher order monochromatic aberrations. Chromatic aberration arises because the refractive index of the ocular media, like all common optical media, increases with decreasing wavelength. Consequently, any light rays incident on the cornea except those perpendicular to its surface will, upon passing into the eye, is bent more if the wavelength is short than if it is long.
However, pupil size abnormalities can sometimes signal diseases, such as: glaucoma or aneurysm [54], which cause pupil dilatation, while cluster headaches results in constriction; lung cancer and brain tumor, due to the mass that compresses the nerve, as well as many other conditions, like e.g. head trauma, stroke and ictus, can cause changes in the size of the pupil.
Pupil size and shape are not the only parameters eligible: it is in fact very important a dynamic approach in medical examination, in order to identify for e.g. a defect in direct response to the light, and whether a patient is complaining of decreased vision from an ocular problem such as cataract or from a defect of the optic nerve. Some examples as the syphilis can cause an Argyll-Robertson pupil, condition in which pupils are small, unequal, misshaped and constrict with near focusing but do not react normally to light; the Relative Afferent Pupillary Defect (RAPD), for instance, is a defect in the direct response and is due to damage in optic nerve or severe retinal disease; the Adie's (Tonic) Pupil is a benign process which is related to either absent or sluggish response to light; it is common in women in the 3rd/4th decade of life (but also can be present in men), if the suspicion is confirmed, that sign may represent a denervation in the postganglionic parasympathetic nerve; the Horner's Syndrome, characterized by a loss of sympathetic innervation, secondary to many disease or disorder, i.e. carotid artery dissection, dysplasia and nasopharyngeal tumors, as well as lymphoproliferative disorders [55]. Pupil size and pupil dilation have been studied in relation to mental workload and the overall state of alertness and pupillography has been successfully employed in monitoring psycho-cognitive activity in many perception experiments such as speech or word recognition, reading and simple auditory tests. The limitations of the pharmacological methods led to the application of infrared video pupillography (pupillometry), a non-invasive optical technique that was established by Otto Lowenstein that does not depend on the condition of the epithelium or the stability of the solutions [56], and can measure a natural phenomenon, not a chemically induced one. Pupillometry is based

on the fact that the size and the responsiveness of the human pupil are governed by the antagonistic action of the Parasympathetic. Nervous system (ParNS) and the Sympathetic Nervous System (SNS), pupillometry is widely used as a clinical test for the functioning of both branches of the ANS.

7.2 Flicker

Rapidly varying loads such as electric furnaces, arc welders, large motors, etc. cause disturbances during power generation, transmission or distribution, that are the origin of supply voltage fluctuation. This is a power quality problem which generated engineering concern since the onset of electrical illumination technology. The term *flicker* is strongly associated with the operation of varying loads. Flicker involves voltage fluctuation and its effect on the lighting system resulting in changes in luminance and consequent irritation of human vision. The type of voltage fluctuation, caused by subharmonics and interharmonics of voltage, associated with lighting is commonly called *voltage flicker* which can be divided into two general categories: cyclic and non-cyclic. The first one results from periodic loads such as welders as in the given system. The second, on the other hand, may be caused by a motor starting or breaking on a random schedule. Considering the filament incandescent lamp in the light system, cyclic voltage flicker can be conveniently expressed as the RMS value of the modulating waveform divided by the RMS value of the fundamental voltage. For a non-cyclic case, it also can be expressed as the change in voltage divided by the average voltage, multiplied by 100, to obtain, in this way, a percent of change. The measurement of the voltage flicker involves the determination of the system RMS voltage variation and the frequency at which it occurs. The maximum permissible voltage disturbances that the system can tolerate without complaints about light flicker and annoyance is termed *Light Flicker Voltage Requirements*. The International Electrotechnical Vocabulary [57] defines Flicker as the *impression of unsteadiness of visual sensation induced by a light stimulus whose luminance or spectral distribution fluctuates with time*. So, *Light Flicker* is a subjective impression of luminance fluctuation of light emanation or gleams from a lamp. The International Electrotechnical Commission with the IEC 61000-2-2 define the parameters that try to make a subjective phenomenon with the objective rules that can be applied in the regulations. *Pst* (Perception of flicker Short Term), the short-term flicker severity (¡10 min). By applying variations on a incandescent light bulb 60 W emitted power for 10 minutes on a sample of people who observed the emitted light, 50% of them revealed the presence of variations of lighting intensity. In this noise value it is assigned the value Pst = 1.0. *Plt* (Perception of flicker Long Term),

severity of the long-term flicker which is calculated from a sequence of 12 values of Pst on an interval of 2 hours, but the required specifications may vary.

7.3 Flickermeters, state of the art

It is clear that the relationship between voltages and luminous fluctuation is closely dependent on the kind of source and that how the human eye perceives light variation is the results of complex neuro-physiological and psychological mechanisms which may change among people. Therefore, the evaluation of flicker severity shall theoretically require information on the light source, the voltage supplying it and, obviously, the response of the human visual system to the produced luminous radiation, pending such a model holds for all the people. The instrument defined by the standard $EN61000-4-15$ [58], which has been adopted by the IEEE as $IEEEStd1453$ [9], processes the voltage and compute an index representing the flicker severity that must be compared with the limit in [59] to verify if the voltage is compliance or not. Such an instrument assumes that the light source is a 60 W, 230 V, 50 Hz incandescent filament lamp and implements a model of the eye-brain system. The reason for which an incandescent lamp is considered is very simple: when the Standard was written, such kind of light was the most commonly light source used. As far as the visual system model is concerned, it was obtained starting from the studies carried out by Rashbass [60] and by Koenderink & Van Doorn [61, 62] in the 1970s.

Recently, great attention has been devoted to quantification of pupil responses to colored light stimuli. These studies were aimed on the one hand to assess outer and inner retinal function [18, 19] and on the other hand to evaluate the effects of chromatic flicker [20, 21]. Low-uncertainty and repeatability are the most important characteristics for a pupillometer designed for this application. Although numerous researches on chromatic pupillometry are ongoing and promising results are reported in the literature, no commercially devices are available and no standardized protocols have been defined for clinical usage. The existing approaches have relied on either off-the-shelf proprietary laboratory equipment [21], or modified Ganzfeld dome equipped with eye-tracking cameras [63]. The combination of the two systems can cost more than 10,000 €. Moreover, the integration of the light stimulator and recording camera into a single measuring system might ensure the immediate use, better repeatability and provide a first step toward a clinical use of this technique. In this work is presented a user-friendly handheld chromatic pupillometer, an improved version based on previous studies [12, 13], that could be easily used even by non-expert personnel. The device includes the light stimulator

and pupil acquisition unit. Thanks to a fast prototyping implementation, the parts of the system can be easily assembled and the cost of all the system components is less than 500 €. Flicker stimulation is based on a RGB LEDs unit controlled directly by the user through a simple LABVIEW virtual instrument. To avoid off-axis artifacts, the pupil image is acquired coaxially with the stimulus by a low-cost, 25-Hz CCD camera equipped with a fixed focal length objective. Moreover, a soft eyepiece is used to maintain stable the eye-camera distance reducing artifacts due to involuntary movements along the optical axis.

7.4 Flicker effect on the human being

7.4.1 Mental fatigue or annoyance

A number of scientific papers analyze the psychophysical effects of light flicker [8, 64, 65, 66]. Mental fatigue is a common phenomenon in daily life. The term *fatigue* has, unfortunately, become a rather overworked word, with its precise meaning eroded by multiple uses. At this point, we should define our meaning of the term. It is defined as a state of cortical deactivation which reduces cognitive performance and causes reduction in attention or concentration. The physiologic definition is about the condition of cells or organs in which have undergone excessive activity with resulting loss of power or capacity to respond to stimulation. To assessing mental fatigue researches present two strategies: one taking in account ergonomic and technical parameters the second is is based on recording of physiological outputs of the body, by means of measurements of biochemical and electrical parameters (e.g. EEG, ECG, heart rate, respiration rate) [67, 68]. When normal man or animals are subjected to sensory or emotional stress, the pupils enlarge, and a light reflex elicited under such conditions will be inhibited. When, on the other land, the subject is tired, and when the eye is expose to repeated light stimuli as fairly short intervals, the pupils become smaller and the reaction less and less extensive. In these works, the human annoyance is basically associated with fluctuations in the light irradiance and spectrum, frequency and duration of the fluctuations. The definition of flicker, presented previously on section 7.2 preview that the degree of annoyance is quantified respect to a 60 W coiled lamp, therefore, the quantification is limited to a specific type of lamp (no longer available on the market) with spectral characteristics dominated by the black body emission. Moreover, it is important to understand the difference between sensation and perception. The definition of flicker uses the terms *sensation* that is the physiological detection of external conditions that can lead to a nervous system response. Perception is the process by which the brain interprets sensory information. Thus some stimuli can be detected and lead to a nervous

system response but not interpreted. Some people who suffer from flicker sensitivity may not be aware that flicker is the reason they are suffering. Furthermore, not all human observers are equally sensitive to the potential effects of flicker. Hence, the subjective analysis performed by a survey used for the quantification of flicker, offers two main problems: (i) it refers to a standard source no longer commercially available, and (ii) suffers from all the problems related to wrong perceptions. Our attempt is to quantify the flicker through a measurable variable as the ocular pupil. This information has always been recognized in the medical world as a parameter indicative of health disorders [14, 15, 16]. Thus, we believe that it can be also correlated to the annoyance induced by luminous flicker. To not be bound to a specific type of lamp, the approach presented in this work involves the use of LED sources in order to generate stimuli of variable irradiance, color and, frequency and amplitude of the fluctuation.

7.4.2 Melanopsin

Studies in the1990s and early 2000s demonstrated the existence of a third class of mammalian photoreceptors that differs greatly from rods and cones, the ganglion cells or ipRGCs, it utilizes a different photopigment, melanopsine, is much less sensitive to light. The ipRGCs primary role is to signal light for largely subconscious, non-image-forming visual reflexes, such as pupillary constriction, neuroendocrine regulation, and synchronizing daily (*circadian*) physiological rhythms to the light/dark cycle (*circadian photoentrainment*) [69]. These latter effects have barely been studied in regard to mood, but recent investigations on the direct effects of light on sleep and alertness suggest additional pathways through which light could influence mood. Based on our recent findings, we suggest that light, via melanopsin, may exert its antidepressant effect through a modulation of the homeostatic process of sleep [70]. Studies involving human and non-human primates have demonstrated a role for ipRGCs in the primate found that when outer retinal photoreceptive signals were blocked pharmacologically, the PLR persisted in macaques, and that the spectral sensitivity of the residual response was closely matched by the spectral sensitivity of melanopsin, which is maximally sensitive to 483 nm light. In addition, this study found that in both humans and macaques, the melanopsin photoresponse of ipRGCs is responsible for the post-illumination pupillary constriction which is seen following a period of high intensity light stimuli [71].

Chapter 8

Research Activities

8.1 Characterization of the solid state sources

The GaN LED is a solid state light source with high energy efficiency but the technology is not yet fully consolidated, for this reason several research group are focusing their studies on the *Efficiency Droop* that affect this kind of solid state sources. On the other hands is very important to drive in a proper way this new sources.
In this chapter a fully characterization of this solid state source is presented. Starting from the analysis of the GaN chip semiconductor, focusing on the efficiency problem that afflict this sources, the *Droop Efficiency*, presenting the model of the GaN LED on which are modified and simulated the principal parameters that act on the droop effect in order to find a possible combination and solution to a first approach solution. A characterization of the commercial lamps based on the GaN LED, photopic, thermic, electronic and electric measurements, will be presented. The effect of the light emitted by these sourced on the human visual system will conclude the research activity of the present chapter, to complete an implemented simulink model of the pupillary light reflex mechanism will be presented.

8.2 GaN LED

Physical mechanisms causing the efficiency droop in InGaN/GaN blue light-emitting diodes and remedies proposed for droop mitigation are classified and reviewed. Droop mechanisms taken into consideration are Auger recombination, reduced active volume effects, carrier delocalization, and carrier leakage. The latter can in turn be promoted by polarization charges, inefficient hole injection, asymmetry between electron and hole densities and transport properties, lateral current crowding, quantum-well overfly by ballistic electrons, defect-related tunneling, and saturation

of radiative recombination. Reviewed droop remedies include increasing the thickness or number of the quantum wells, improving the lateral current uniformity, engineering the quantum barriers (including multi-layer and graded quantum barriers), using insertion or injection layers, engineering the electron-blocking layer (EBL) (including InAlN, graded, polarization-doped, and superlattice EBL), exploiting reversed polarization (by either inverted epitaxy or N-polar growth), and growing along semi- or non-polar orientations. Numerical device simulations of a reference device are used through the paper as a proof of concept for selected mechanisms and remedies.

8.2.1 Efficiency Droop

The knowledge of key parameters that *controls* the droop is affected by relatively-large uncertainties, including: Auger coefficient (C), band offsets and polarization charges at AlGaN/GaN and InGaN/GaN interfaces, QW capture times. A systematic, sensitivity analysis of IQE vs J curves to droop-controlling parameters may be useful to create correlations between different IQE-vs-J behaviors and parameter ranges. Multiple mechanisms can be active at same time. Effects of droop remedies are not trivial to interpret. Some of them can mitigate one droop mechanism only, leaving the other(s) unchanged. Others can act on different mechanisms in parallel even though they have been thought of as antidotes for a specific one.

Model

The reference device is an InGaN/GaN multi-quantum-well (MQW) LED with the following epitaxial structure (from bottom to top): Si-doped n-region, MQW active region consisting of four periods of 10 nm undoped GaN quantum-barrier (QB) and 3 nm undoped $In_{0.15}Ga_{0.85}N$ quantum-well (QW) layers, undoped 5 nm GaN spacer, 40 nm p-doped $Al_{0.15}Ga_{0.85}N$ electron-blocking layer (EBL), p-region, figure 8.1.

This device has been analyzed by means of a commercial numerical device simulator (Sentaurus Device, Synopsys, Inc.)[72],allowing the effects of varying material- and technology-related parameters influencing the droop to be evaluated. Results of these simulations will be shown to observe deeper insight into some of the droop mechanisms and remedies being reviewed, than finally propose a new path of investigation for innovative droop remedies. In the QWs, separate continuity equations are solved for continuum and bound states, with carrier scattering from continuum into bound states included as recombination/generation terms governed by QW capture times. The QW bound states are solved from a 1D Schrödinger equation. Transport of carriers from(to) outside the QW to(from) the QW continuum states is modeled by thermionic emission, while drift-diffusion transport is adopted for regions outside

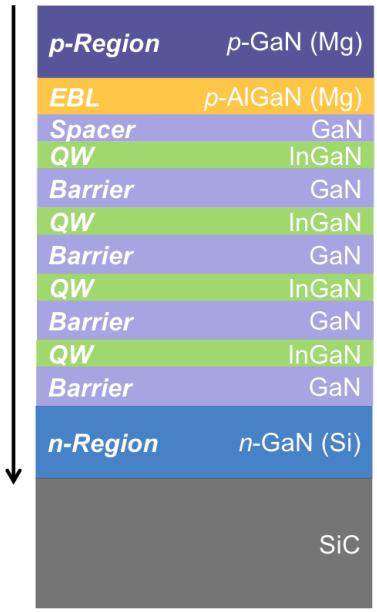

Figure 8.1: The reference device for the droop efficiency simulations.

the QWs. The input parameters that have been kept at their literature values for the different materials in all of the simulations include: *relative dielectric constant* [73], *bandgap* [74], *electron and hole effective masses* [74], *electron and hole doping-dependent mobility* [73]. Shockley-Read-Hall (A) and radiative recombination (B) coefficients have been set to typical values ($A = 2 \times 10^7 s^{-1}, B = 10^11 cm3s^{-1}$). The parameters that have been varied and will therefore be specified along with simulation results are as follows:

1. *InGaN Auger coefficient (C)*
2. *The band offset ratio at AlGaN/GaN interfaces* ($\Delta E_{C1} : \Delta E_{V1}$)
3. *The band offset ratio at InGaN/GaN interfaces* ($\Delta E_{C2} : \Delta E_{V2}$)
4. *The polarization charge densities at AlGaN/GaN interfaces* ($\pm\sigma_1$)
5. *The polarization charge densities at InGaN/GaN interfaces* ($\pm\sigma_2$)
6. *The electron and hole QW capture times* (τ_{QW_e}, τ_{QW_h})

Generally assumed values for parameters (2) and (3) are in the 70:30 to 60:40 range [74]. In literature the values used as reference for parameters (4), (5), and (6) are as follows:

- $\sigma_1* = 6.4 \times 10^12 cm^{-2}$ [75]
- $\sigma_2* = 1.5 \times 10^13 cm^{-2}$ [75]
- $\tau_{QW_e}* = 4ps$ [76], $\tau_{QW_e}* = 2ps$ [76]

As far as σ_1 and σ_2 are concerned, lower estimates have recently been reported in [77]. Unless otherwise stated, ionized doping concentrations of $3 \times 10^17 cm^{-3}(N_A)$ and $5 \times 10^17 cm^{-3}(N_D)$ have been used for p- and n-type doping, respectively. Once defined , based on the theoretic literature values, for each of these 6 parameter it has been attribute 3 values inside a possible range defining 3^6 (729) possible combination of IQE curves, figure 8.2. The combination of all the IQE curves are summrized on the same graph, this curves, divided by group, will describe the droop mechanism related to a particular parameter.

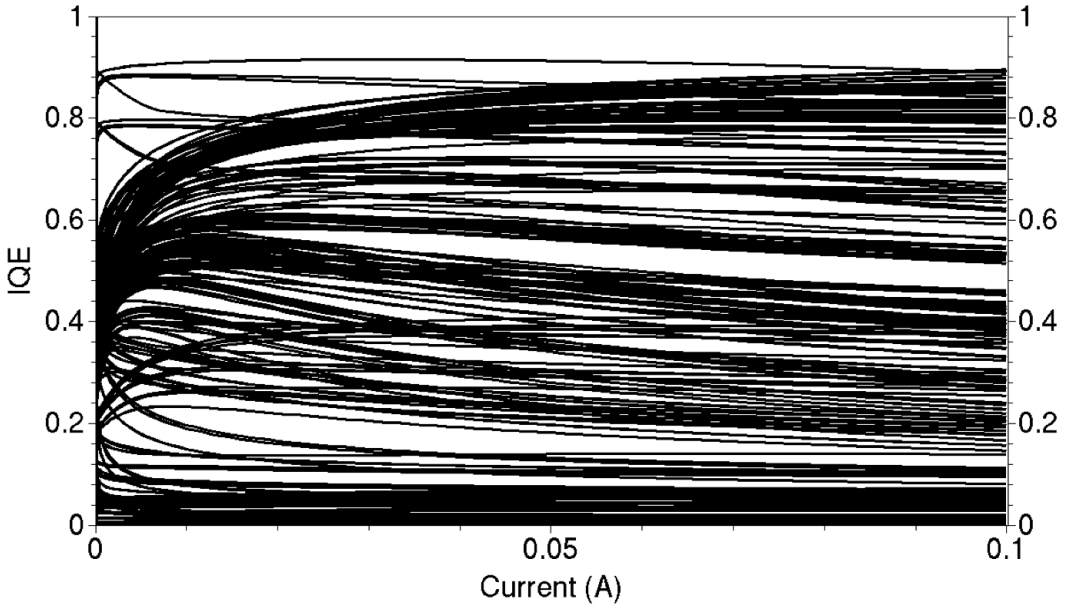

Figure 8.2: IQE considering all the 3^6 combination of parameters.

To analyze the curves obtained by the simulation of the model and understand the different cases of droop efficiency is suitable to follow a guideline as:

- *"Pure" mechanism*
- *Mixed Scenarios*
- *Role of asymmetry*
- *Analysis of (selected) droop remedies*

Pure mechanism

The pure droop mechanism is related to the 6 parameters mentioned before with no relationship and influence between them.
The *Auger recombination* is the most straightforward, high-carrier-density, internal, non-radiative process and one of most debated droop mechanism. It is a three-particle process where an electron from the conduction band recombines with a hole in the valence band, and the excess energy resulting from this recombination is transferred to a third electron (eeh) or hole (hhe) by carrier-carrier interaction. In the figure 8.3 are shown the curves of the IQE vs the driving current, with the other droop influence parameters set to typical literature values. Other effect as electron leakage in not present, the droop curves are the result due to the Auger recombination only. As reported in figure 8.3 the droop effect appears for $C > 10^{-31} cm^6 s^{-1}$, according with the results of the simulation, to be the single cause for large droop effects, Auger recombination C should exceed $10^30 cm^6 s^{-1}$.

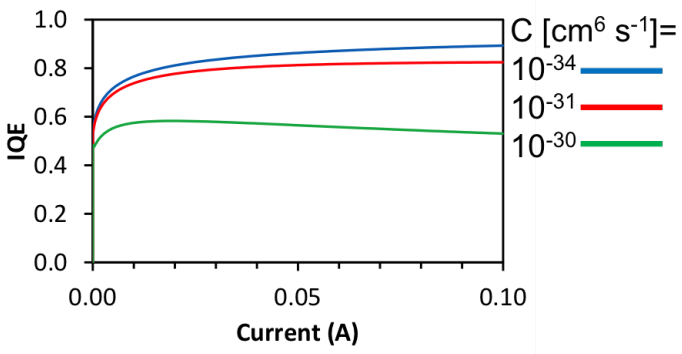

Figure 8.3: IQE curves obtained by modifing only the Auger coefficient.

Concerning the band offset ratio at AlGaN/GaN interfaces, in order for sufficient droop to appear, for the simulator the AlGaN/GaN band offset ratio ($\Delta E_{C1} : \Delta E_{V1}$) should be reduced from theoretical assumed values of 70 : 30 or 60 : 40 to 50 : 50. This assumption results in an electron leakage from the insufficient electron confinement regardless of the effect of polarization fields. The figure 8.4 confirm the indications, Auger recombination C has no role because is kept at a very small value ($10^{34} cm^6 s^{-1}$). As can be noted, no droop is predicted regardless of the σ_1 value if $\Delta E_{C1} : \Delta E_{V1} = 70 : 30$. Droop is instead present due to electron leakage if $\Delta E_{C1} : \Delta E_{V1}$ is decreased to 50 : 50. Larger σ_1 values kill the IQE over the entire current range.

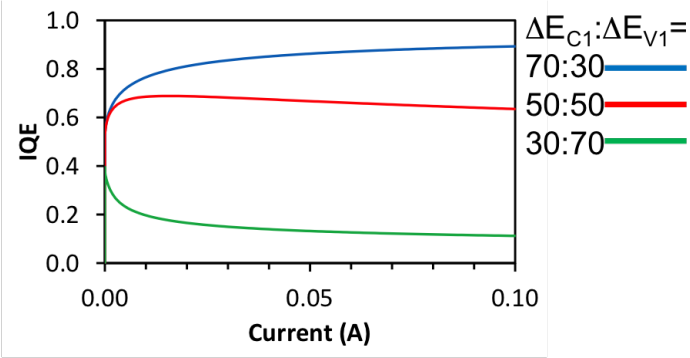

Figure 8.4: Simulated IQE vs driving-current curves for different values of the AlGaN/GaN.

Considering the band offset ratio at InGaN/GaN interfaces ($\Delta E_{C2} : \Delta E_{V2}$), in the figure 8.5 a) are reported the simulated curves and is evident that there is no droop effect even with reversed $\Delta E_{C2} : \Delta E_{V2}$. The results obtained consider $\Delta E_{C1} : \Delta E_{V1} = 70 : 30$. n increases in QBs but this does not translate to electron leakage if EBL confinement capability is intact.

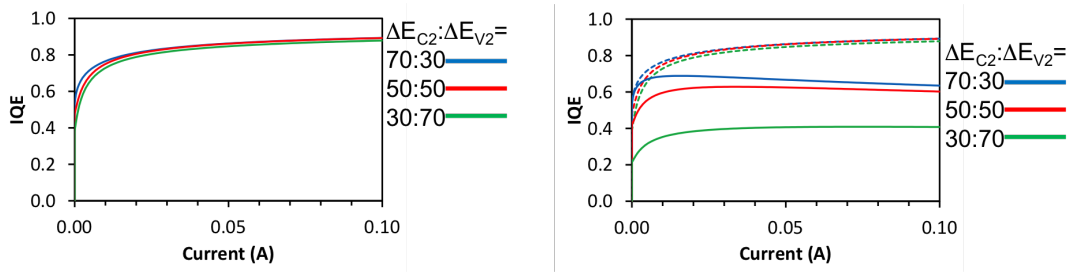

(a) (b)

Figure 8.5: Simulated IQE vs driving-current curves for different values of the InGaN/GaN.

The figure 8.5 b) shows that droop is due to insufficient EBL confinement for $\Delta E_{C2} : \Delta E_{V2} = 70 : 30$ considering $\Delta E_{C1} : \Delta E_{V1} = 50 : 50$. Decreasing $\Delta E_{C2} : \Delta E_{V2}$ reduces the droop, it actually makes electron leakage effective even at low density current J.
The figure 8.6 a) shows that the polarization charge densities $+\sigma_1$ at EBL/spacer attracts electrons into the upper QW making the device more efficient at small current. No droop is predicted if EBL confinement is strong.

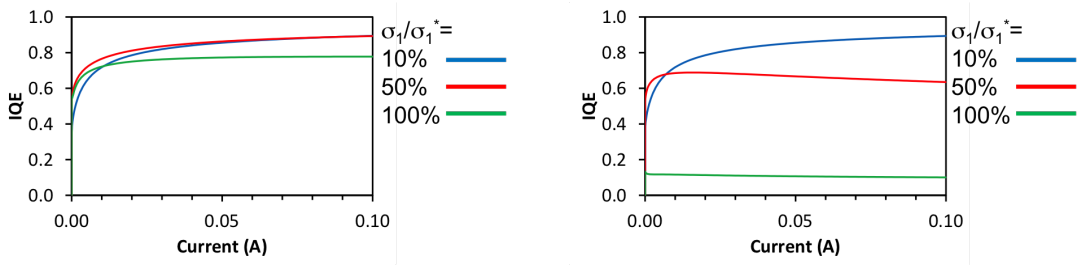

(a) (b)

Figure 8.6: Simulated IQE vs driving-current curves for different values of the polarization charge densities.

Otherwise If $\Delta E_{C1} : \Delta E_{V1} = 50 : 50$, droop is present for $\sigma_1/\sigma_1* = 50\%$ due to electron leakage as the figure 8.6 b) shows. Larger σ_1 values kills IQE regardless of current.
The electron and hole QW capture times $(\tau_{QW_e}, \tau_{QW_h})$ is another parameter that can be considered part of "*Pure*" droop mechanism. The figure 8.7 report the IQE curves versus the driving current with different value of the time capture, in the specific the *Overfly* droop requires τ_{QW} values that are 100 times than those associated with QW phonon-and carrier scattering. Might be representative of defect tunneling under QWs or along structural defects.

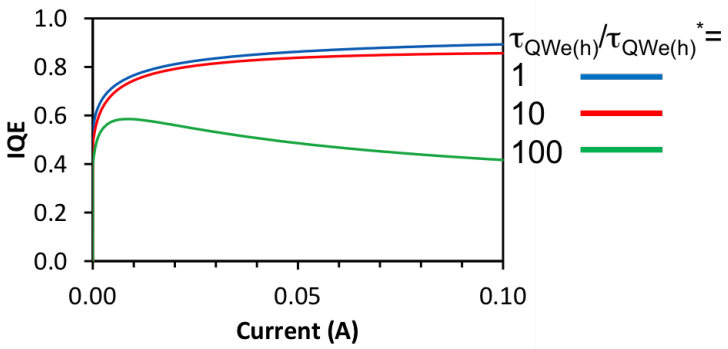

Figure 8.7: Simulated IQE vs driving-current curves for different values of the electron and hole QW capture times.

Mixed scenarios

In this section will be presented the mixed scenarios that describe the 729 IQE vs driving current curves grouped by the main influence of a certain controlling-droop-parameter.

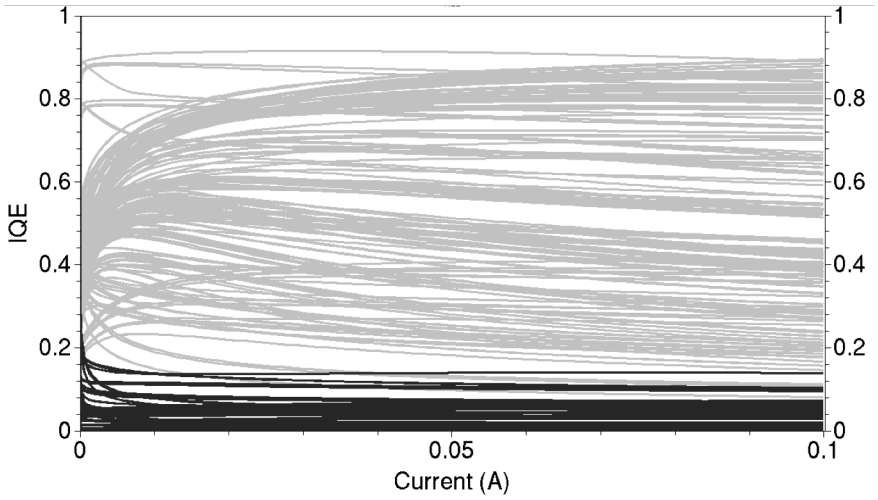

(a)

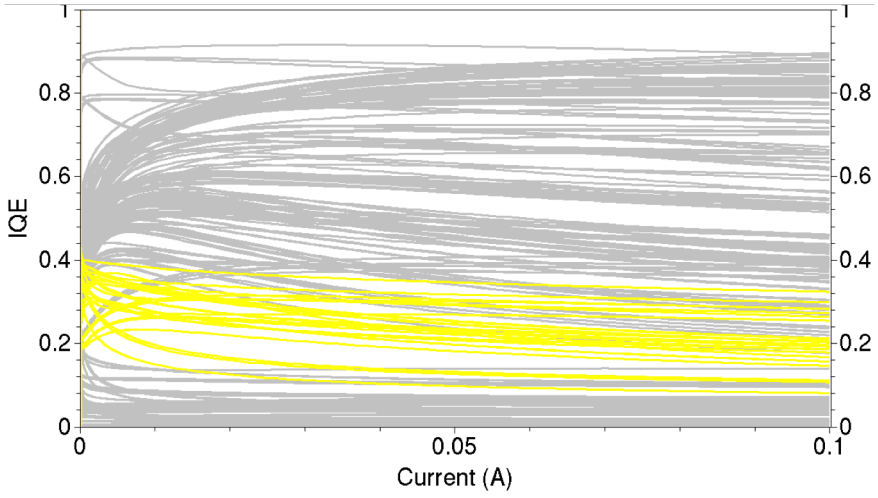

(b)

Figure 8.8: Simulated IQE vs driving-current curves grouped by droop controlling parameters.

The figure 8.8 a) shows the curves generated by the multiple droop mechanisms with *extreme* values for controlling parameters. The figure 8.8 b) report all the curves resulting cause a strong electron leakage.

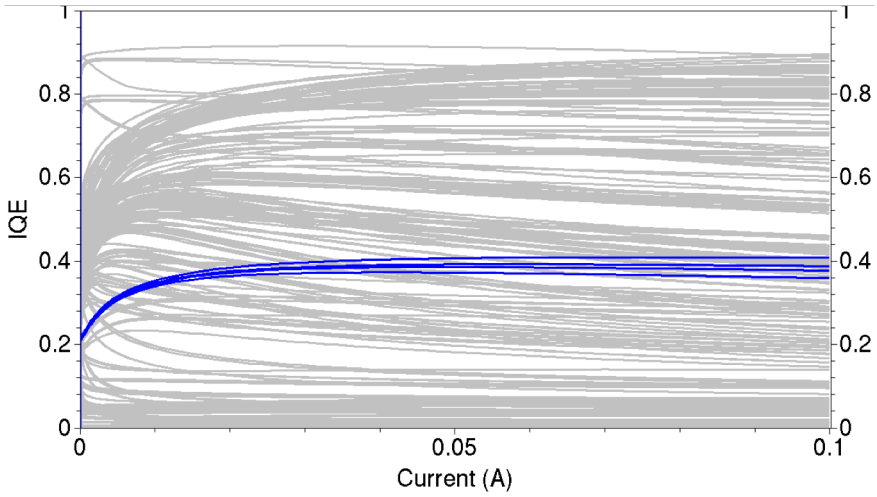

(a)

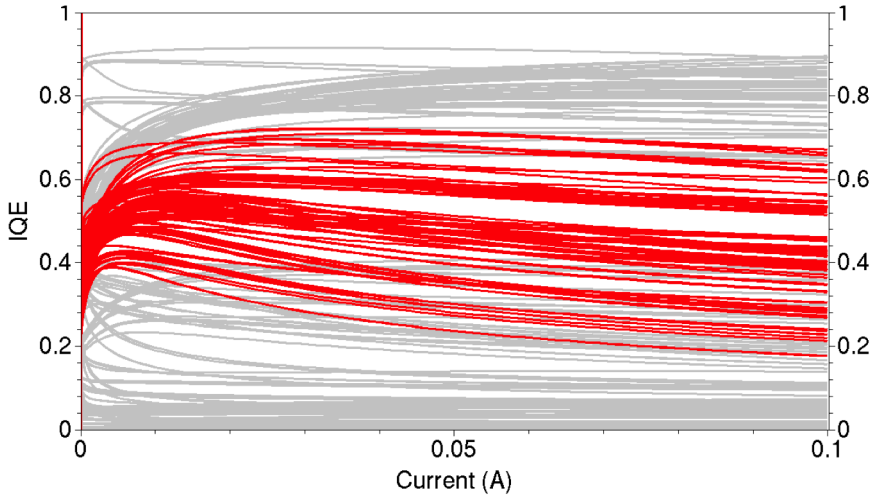

(b)

Figure 8.9: Simulated IQE vs driving-current curves grouped by droop controlling parameters.

The combination of the Auger coefficient C $< 10^{-30} cm^6 s^{-1}$ plus electron leakage, improved hole confinement and reduced electron confinement in QWs generate a small group of curves reported in figure 8.9 a); Pure droop mechanisms with extreme values for controlling parameters or combinations of droop mechanisms with relaxed conditions on controlling parameters identify a large group of simulated curves as shown in figure 8.9 b).

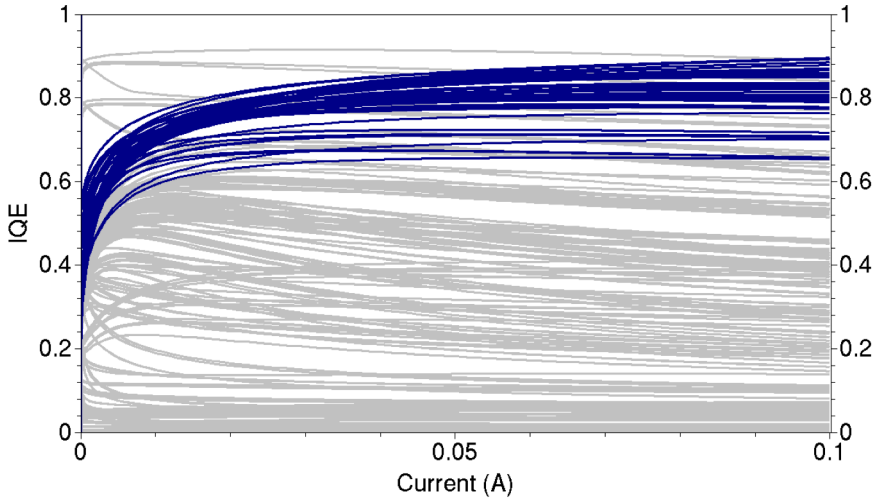

(a)

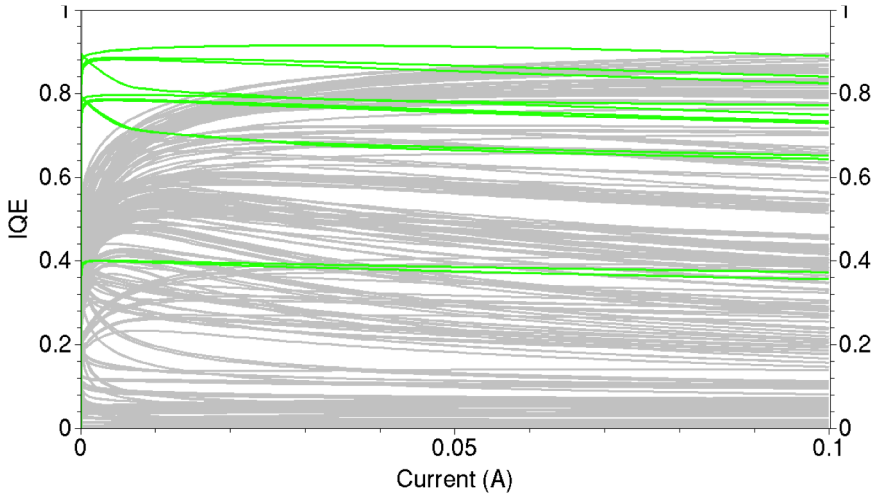

(b)

Figure 8.10: Simulated IQE vs driving-current curves grouped by droop controlling parameters.

In the figure 8.10 a) the curves are partially affected by the droop, the lack of efficiency is evident for low current densities. This results are obtained with all droop-controlling parameters close to their literature/theoretical/common values. The figure 8.10 b) shows a very interesting scenario. The curves present a quasi-constant IQE on the whole interval of current densities, some of them reach also high value of IQE, over 0.8. This curves are obtained with a reduced electron confinement within MQW region combined with effective EBL blocking capability and large polarization charge densities at AlGaN/GaN interfaces σ_1.

Role of asymmetry

Asymmetry in the electron and hole active doping concentration and in carrier transport parameters (mobility and related diffusivities) has been explicitly indicated as a droop cause. The model was modified in order to have no EBL, zero polarization charges ($\sigma_1 = \sigma_2 = 0$), ionized doping densities ($N_A = N_D = 10^{17} cm^3$) equal between n- and p- type, same electron mobility and capture times ($\tau_{QW_e} = \tau_{QW_h} = 4ps$) and finally symmetric InGaN/GaN band offsets ($\Delta E_{C2} : \Delta E_{V2} = 50 : 50$).

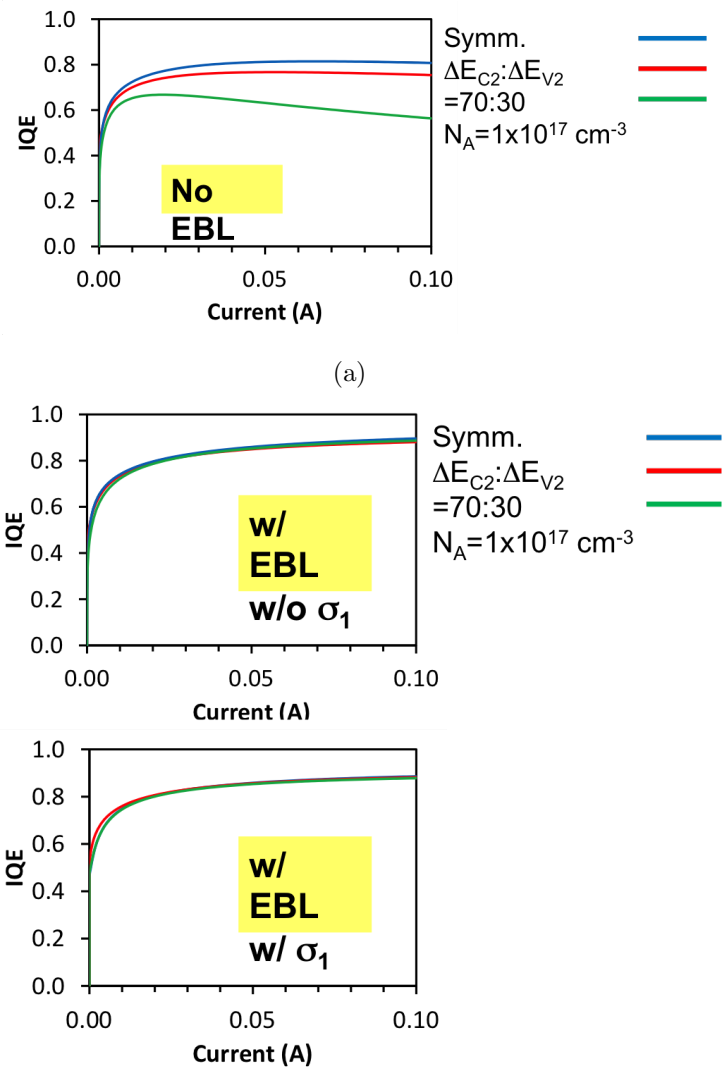

(a)

(b)

Figure 8.11: Simulated IQE vs driving- current curves for a completely symmetric device and for devices implementing only one of the asymmetry factors at a time.

In figure 8.11 a) the asymmetry factors leading to appreciable droop effects only. These specifically are $N_A < N_D$ and $\Delta E_{C2} > \Delta E_{V2}$. To note that a perfectly symmetric LED has no droop, even without EBL. Otherwise by increasing $\Delta E_{C2} >$

ΔE_{V2} from 50 : 50 to 70 : 30 results in a hole-density decrease in the QWs due to weaker hole confinement. The same effect applies when N_A is decreased from $5 \times 10^{17} cm^{-3}$ to $10^{17} cm^{-3}$. In this case, the reason is a smaller hole injection into the active region. In both cases droop is associated with electron leakage. The figure 8.11 b) reports the effect of the EBL with *nominal* electron confinement capability ($\Delta E_{C1} > \Delta E_{V1} = 70 : 30$), to avoid electron leakage, thus suppressing the droop, even in the presence of polarization charges.

Analysis of (selected) droop remedies

One droop solutions is based on the concept of *Reversed Polarization*. The idea is to have polarization charges facilitate electron capture into QWs instead of opposing it. The reversed-polarization concept can easily be tested in the reference device.

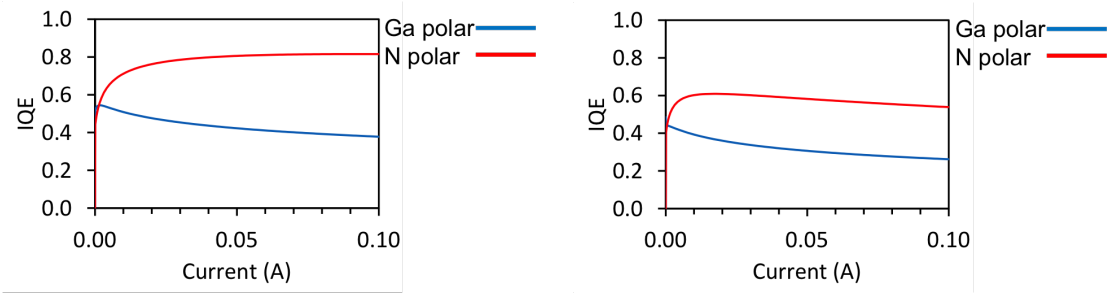

(a) (b)

Figure 8.12: Simulated IQE vs driving- current curves for standard and reversed-polarization.

In the figure 8.12 a) are reported the droop curves for a standard polarization LED in case of weak Auger recombination, in the reference Ga-polar LED, droop is due to a combination of electron leakage and active doping asymmetry. Switching to N polar suppresses the droop effect. The figure 8.12 b) shows the droop curves in case of a reverse-polarization LED and strong Auger recombination. If Auger is added among the droop-causing mechanisms in the Ga-polar LED, switching to N polar increases IQE but does not suppress the droop. Same is expected to take place if other high-carrier-density QW phenomena (like density-activated defect recombination (DADR) or reduced effective volume + Auger) are effective.
Other droop remedies rely on band *Engineering of the EBL*. As the figure 8.13 a) shows in the baseline structure, droop is due to a combination of electron leakage and active doping asymmetry, by increasing N_A almost completely suppresses droop.

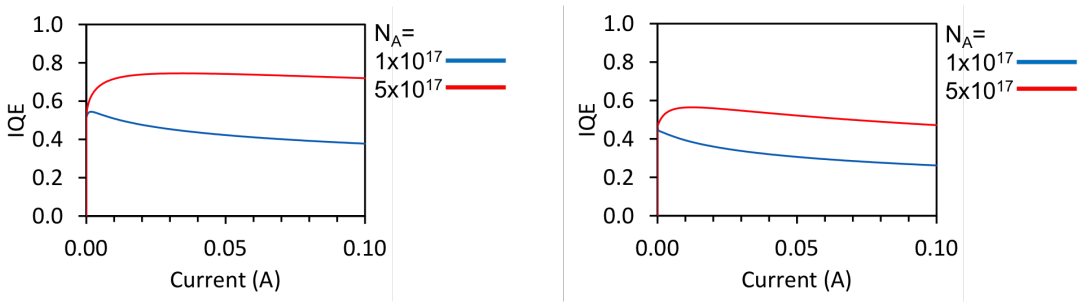

(a) (b)

Figure 8.13: Simulated IQE vs driving- current curves for standard and reversed-polarization.

As reported in figure 8.13 b)similarly to N-polar case, when Auger is added among the droop-causing mechanisms, increasing N_A increases IQE but does not eliminate the droop. Same is expected to take place if other high-carrier- density QW phenomena (like DADR) are effective.

Basic droop mechanisms, such as Auger, carrier leakage (either assisted by polarization charges or by hole-injection impediment or active doping asymmetry), and carrier overfly, appear not to able to explain typically observed droop behaviors, unless somehow *extreme* values for the associated droop-controlling parameters are assumed. Impact of droop-controlling parameters can change depending on values adopted for other parameters.

Due to parameter sensitivity to material/growth/processing conditions, this can contribute to explain difficulties in comparing results from different technologies. In some cases, droop does not show up due to IQE reduction at small currents rather than to actual absence of high-current efficiency reduction mechanism(s).

If multiple droop mechanisms are assumed to be active, conditions on droop-controlling parameters can be relaxed. If this is actually the case in real devices, design of droop remedies and interpretation of results from their implementation during the technology optimization loop may not be trivial, as modifications can either impact different droop mechanisms in parallel or only one.

8.3 Commercial LED lamps

In the following section a full characterization of 10 commercial LED lamps is presented. The figure 8.14 shows the commercial lamps by the name of the manufacturer. As the picture shows the shape the lamps is similar but not the same, almost all the lamps has the E27 plug and few the E14 plug, for the purpose of our studies there is no differences. The diffusive caps of the lamps are some in glass and some in plastics, the light passing through these materials could influence the final amount of radiation measured, this effect is partially considered for the final purpose characterization.

(a) Aster (b) Beghelli (c) GE (d) Isy (e) Kennex

(f) Life (g) Obi (h) Osram (i) Philips (j) Wiva

Figure 8.14: The 10 commercial LED lamps characterized.

The table 8.1 summarize the principal declared parameters of these lamps. Correlated color temperature (CCT), 5 lamps at 3000 k and 5 at 2700, the electrical power and the current absorbed by these lamps is almost the same. To exclude as much as possible the external variables that could influence the characterization. The quality of the diffuser and the number of GaN chip LEDs inside the diffuser determine the luminous flux of the devices, the Beghelli lamp has almost the double luminous flux respect the lowest value declared by GE (General Electric), as it will show after the number of LED of the Beghelli lamp is much higher than the GE.

For each lamp has been done a complete characterization:

- *Photometric*
- *Thermic*
- *Electronic (Converters)*

Model	El.Pow.(W)	CCT (K)	Lum.Flux (lm)	Current (mA)
Aster	4	2700	300	45
Beghelli	4	3000	410	40
GE	4	2700	220	40
Isy	4	2700	250	43
Kennex	4.5	2700	350	49
Life	4	3000	310	40
Obi	4	3000	320	37
Osram	4	2700	250	42
Philips	4	2700	250	35
Wiva	4	2700	250	40

Table 8.1: Productors declared parameter of the LED lamps. The ID number is used to identify the curves measured with the proper lamps

- *Electric (quality of the light emitted versus a disturbed electrical stimulus as input)*

The photometric characterization includes the measurement of all the main optical parameters of a chip LED or a LED lamp. By measuring the spectrum is possible to obtain information, such as intensity of the light emitted in relation to the angle of emission, the light intensity referred to each wavelength emitted (as explained before the white light is a multiple composition of many wavelengths), the color rendering and the chromaticity coordinates of the light emitted. The thermal characterization is based on the detection of the total temperature of the lamps, then the identification of the areas subjected to higher temperatures, thus defining the higher point temperature. An analysis of the electronics converters is presented, the design of the converters is an important point for the total efficiency and quality parameters of the lamp. Finally it has been tested the electric conversion capability to light quality emission of the electronic converters. Over the nominal tension supply for the lamps it has been applied electrical flicker frequencies, low and high frequencies, with different modulation depth, the optical response of the lamps is measured in order to verify and quantify the optical flicker signal.

8.3.1 Optical characterization

The light spectra of the 10 sources is measured by a spectrometer (SP-100 CSA Group, Orb Optronix) able to measure 380-780 nm, optical bandwidth of 4 nm and wavelength binning resolution of 1 nm. The spectrometer, fixed at about 1 mt , is coupled perpendicularly with an horizontal type-C goniometer equipped with precise

stage motors that guarantee high repeatability and movement precision. The figure 8.15 shows the spectrometer and the goniometer.

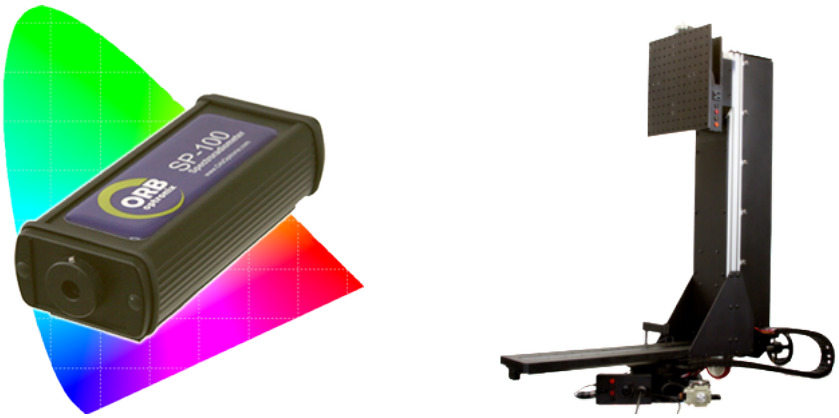

(a) (b)

Figure 8.15: Equipment used to perform the photometric characterization pf the LED lamps, The spectrometer to measure the light a), the goniometer b) to move the source.

The optical characterization includes the measurement of several parameters, all obtained by using the described instruments with a single step measurement. The photometric characterization includes the evaluation of many light properties, in the specific:

- *Optic power spectrum*
- *Color Rendering Index (CRI)*
- *Polar diagram*
- *CIE 1931 chromatic coordinate diagram*

All the measurements are performed with a distance of about 1 meter from the cosine corrector applied to the entrance of the spectrometer and the diffusive caps of the lamps.

Optical power spectrum

The figure 8.16 shows the optical power spectrum of the 10 lamps. All the devices are GaN chip LED based sources, and the spectrum measured is typical of these LED chips. The blue peak of the GaN is evident at around 455 to 460 nm, a second bigger peak around the green optical frequencies is the maximum emission of the phosphor that cover the GaN chip. The intensity of the blue emission is lower than

the emission of the phosphors, that difference explain the CCT of the light emitted. A cold white is obtained with a big high emission of the blue peak in confront to the phosphor curve, viceversa if the phosphor peak is higher than the blue one we obtain warm white. As it will be explained the chromatic coordinates quantify and identify the light measured, also the CCT.

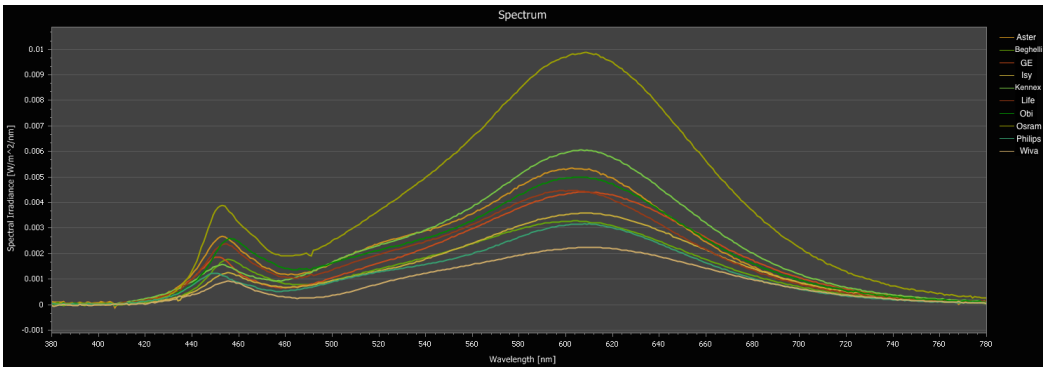

Figure 8.16: Optical power spectrum of the 10 Led Lamps

Color Rendering Index (CRI)

Color rendering is defined as the *effect of an illuminant on the colour appearance of objects by conscious or unconscious comparison with their colour appearance under a reference illuminant* (CIE 17.4, International Lighting Vocabulary). The General Color Rendering Index *Ra* is calculated in accordance with CIE 13.3-1995, Method of Measuring and Specifying Colour Rendering Properties of Light Sources. It is the arithmetic mean (i.e., average) of the Specific Color Rendering Indices for each test color, figure 8.17, and is usually referred to simply as the CRI value of a test illuminant. Eight pastel test colors are used to determine the color shifts and hence the Specific Color Rendering Indices for a test illuminant. Six additional colors are sometimes used for special purposes, but they are not used for calculating *Ra*.

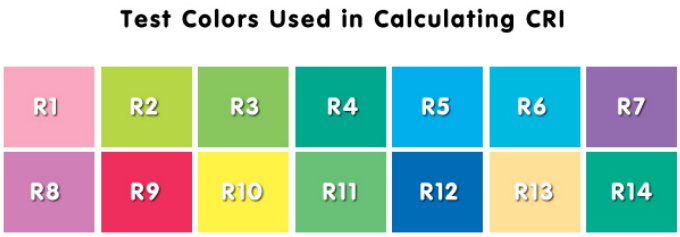

Figure 8.17: CRI test color with the identificative code for each color.

The figure 8.18 shows the color rendering index of the commercial led lamps. The General Color Rendering Index *Ra* is in line with the literature value of the

LED lamps. For each test color the value reached by the lamps is very similar, the *R9* value that identify the RED colors, the CRI of all the lamps is very poor. Few lamps has a slightly better value for *R9* but still largely under an acceptable value of 80%.

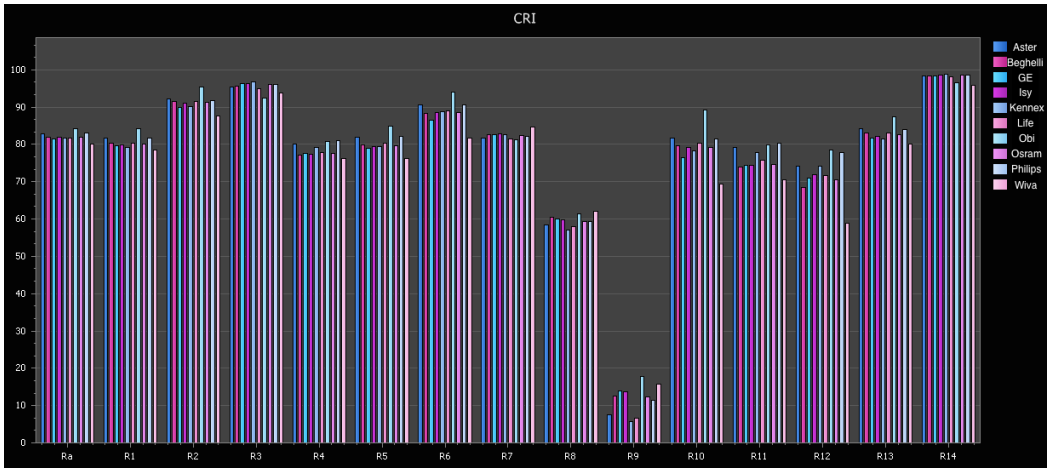

Figure 8.18: Color rendering index of the LED Lamps.

CIE 1931

The CIE 1931 color spaces are the first defined quantitative links between physical pure colors (i.e. wavelengths) in the electromagnetic visible spectrum, and physiological perceived colors in human color vision. It characterizes colors by a luminance parameter Y and two color coordinates x and y which specify the point on the chromaticity diagram. Based on the fact that the human eye has three different types of color sensitive cones, the response of the eye is best described in terms of three "tristimulus values".

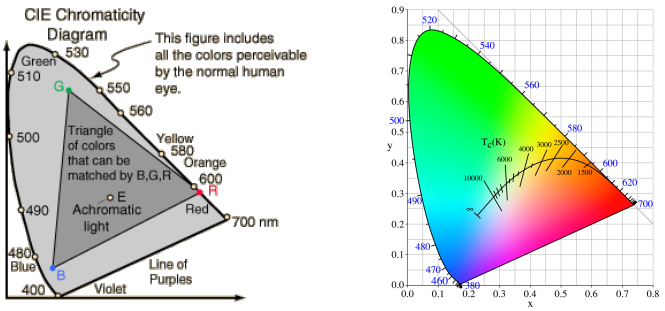

(a) (b)

Figure 8.19: CIE 1931 diagram to characterize colors by two coordinates. a) identification of the RGB colors, b) an example of the CIE 1931 diagram with expressed the CCT lines

However, once this is accomplished, it is found that any color can be expressed in terms of the two color coordinates x and y, the colors which can be matched by combining a given set of three primary colors (such as the blue, green, and red of a color television screen) are represented on the chromaticity diagram by a triangle, see figure 8.19 a), joining the coordinates for the three colors. The mathematical relationships that define these color spaces are essential tools for color management. They allow one to translate different physical responses to visible radiation in color inks, illuminated displays, and recording devices such as digital cameras into a universal human color vision response. In figure 8.20 ten points for each lamp are defined with 2 coordinates and identify the color and the CCT of the light emitted by the lamps.

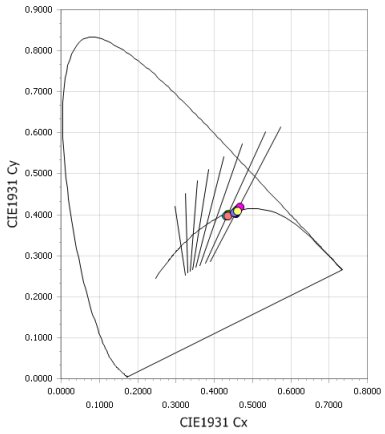

Figure 8.20: Chromatic coordinates on the CIE 1931 diagram of the commercial lamp light measured.

The differences between the points are the different CCT, as mentioned 5 lamps with 3000 K and 5 with 2700 K, the different disposition of the chip LEDs inside the diffuser, the thickness, material and shape of the diffusers.

Polar diagram

The polar luminous intensity graph, polar diagram, illustrate the distribution of luminous intensity, in candelas, for the transverse and axial planes of the luminaries, provides a guide to the type of distribution expected from the luminaries over the angle, for example wide, narrow, direct, indirect etc. in addition to intensity.
The figure 8.21 shows the polar luminous intensity distribution of the commercial lamps analyzed, the intensity of the light emitted it has been measured with angles from -90° to 90° with a step of 2°.

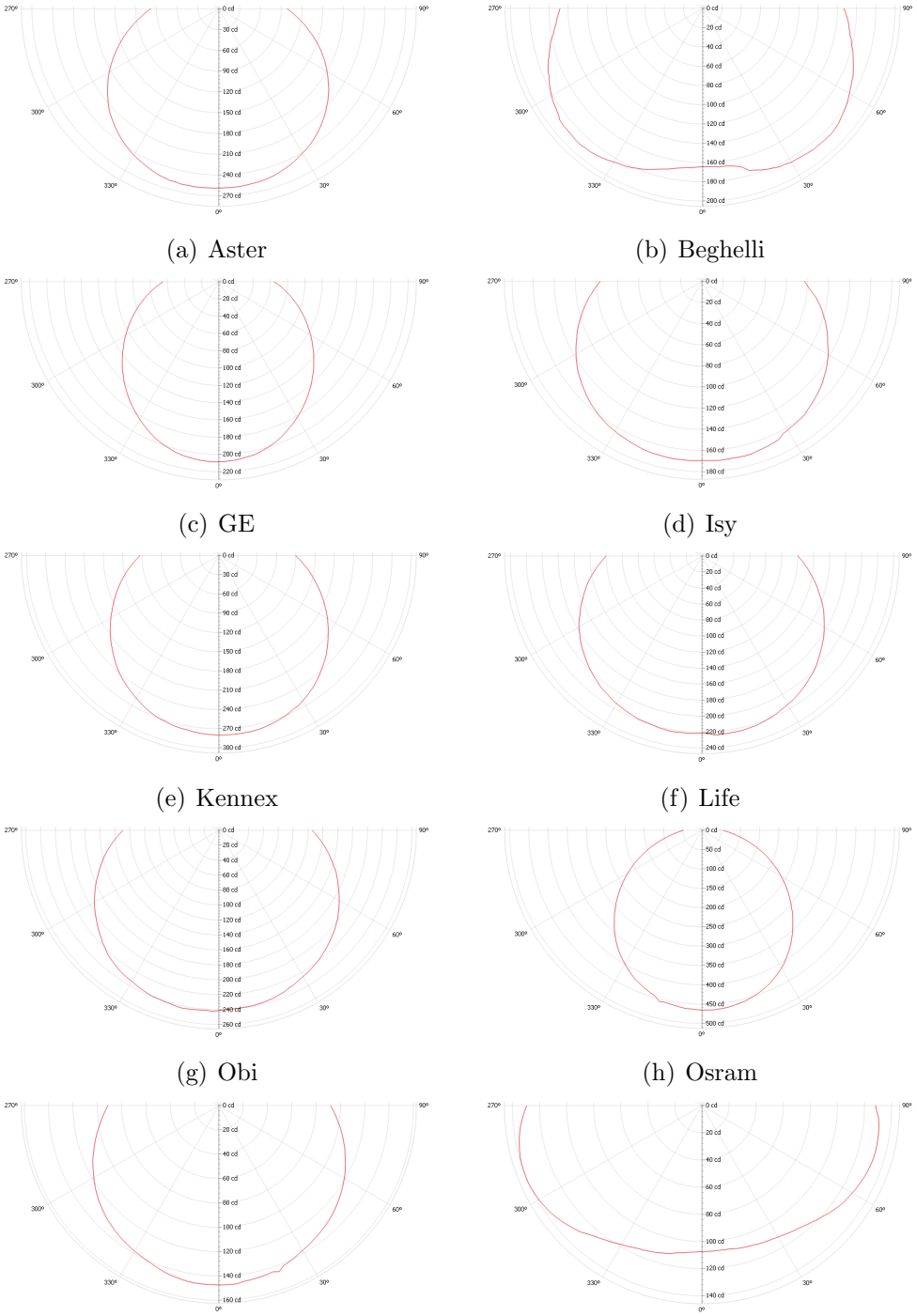

(a) Aster (b) Beghelli

(c) GE (d) Isy

(e) Kennex (f) Life

(g) Obi (h) Osram

(i) Philips (j) Wiva

Figure 8.21: Polar diagrams of the 10 commercial lamps.

The shape of the curve measured is function of the light intensity detected by the spectrometer and the angle orientation of the lamp. The light emitted is influenced by the material quality, shape, of the diffuser, disposition of the LEDs. For most of the lamps tested the LEDs are fixed on the same plane (see section 8.3.3), perpendicular to the spectrometer observation direction. The LEDs are symmetrically

fixed on the perpendicular support.
For all the lamps except 2 models (Beghelli and Wiva) the polar luminous intensity graph as a similar shape if the luminous intensity is not considered. The polar graph of Beghelli and Wiva is diffrent, the light emission at 0° is lower that the side of the lamps. For the Beghelli model this effect is due to the physical disposition of the chip LEDs on the holder, figure 8.22 a), only few LED are fixed on the same observation axis of the spectrometer. The different technology of the Wiva lamp, based on wire chip led, justify the strong difference on the polar graph respect to the other lamps. The wire LEDs usually are disposed longitudinally, or almost longitudinally 8.22 b), respect the axis of the lamp and the spectrometer observation.

(a) Beghelli LEDs (b) Wire LEDs

Figure 8.22: The LED disposition on the Beghelli lamp holder a), a wire LED lamp b).

Another way to observe the light intensity distribution over the solid angle is the cartesian luminous intensity graph, the diagram indicates the distribution of luminous intensities in candelas of the luminarie, a visual guide to the type of distribution expected from the luminarie or lamps, for example, narrow or wide beam etc. in addition to intensity. This diagram is useful when the light intensity change rapidly within a small angular area.
The commercial lamps cartesian luminous intensity graph, figure 8.23, present for the most of the lamps a gaussian like form of the intensity versus the angle. As for the previous polar graph the Beghelli and Wiva models have less emission at 0° due, for Beghelli model, to the bigger number of LEDs fixed on the side of the holder, figure 8.22 a), the wire LED technology of the Wiva lamp allow higher emissions on the side of the lamp 8.22 b).

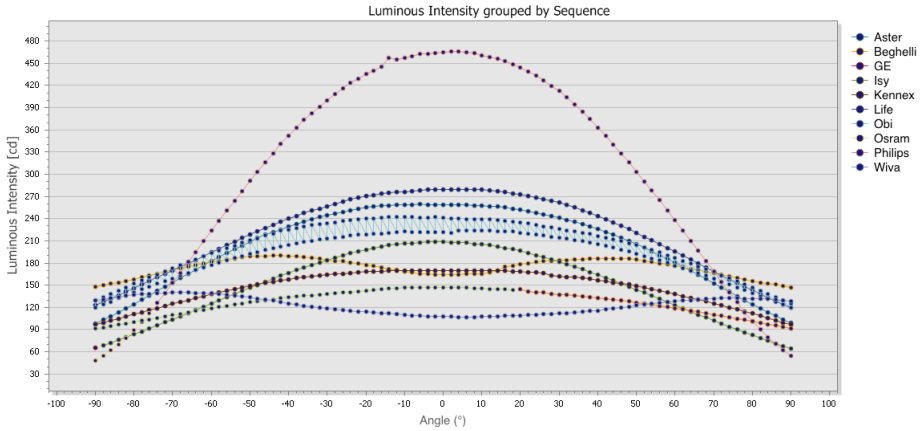

Figure 8.23: Cartesian luminous intensity graph of the commercial lamps.

8.3.2 Thermal characterization

The thermal characterization has been performed with the thermal camera FLIR T620, spectral sensitivity 7.5 to 14 μm, temperature range -40 °C to 650 °C with a thermal sensitivity <0.04 °C at 30 °C, with a field of view (FOV) of 25° x 19°, minimum focus distance of 0.82 ft (0.25 m) than FOV Match where digital image FOV adapts to the IR lens finally the detector is a focal plane array (FPA) uncooled microbolometer of 640 x 480 pixels. The figure 8.24 shows the thermal images of the 10 lamps after 30 minutes of warm up time.

The average temperature of the lamps is 70,2 °C with some particular cases with 91,2 °C highest temperature and 48,9 °C the lowest. In 9 cases the peak of temperature happen in correspondence of the electronics housing, the high temperature is due from the heat contribution of the chip LED and mainly the electronics, except in one case where the peak of temperature close to the top of the diffuser. This effect could be produced by the wire technology adopted by the Wiva constructor, where all the 5 wire led are connected to one and all the supply current flow through this point.

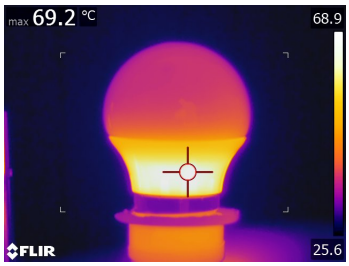

(a) Aster

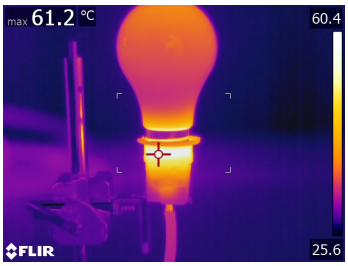

(b) Beghelli

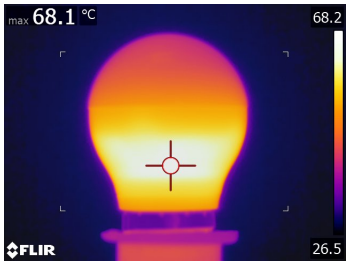

(c) GE

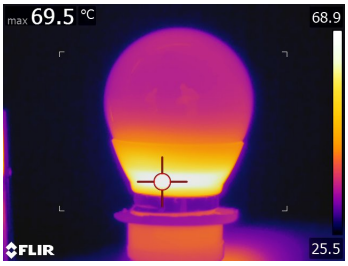

(d) Isy

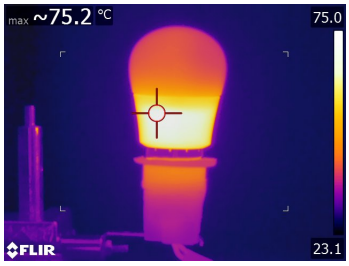

(e) Kennex

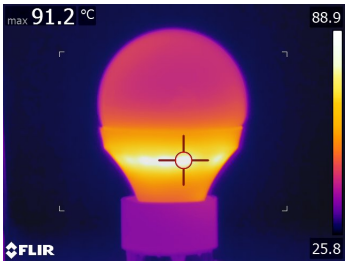

(f) Life

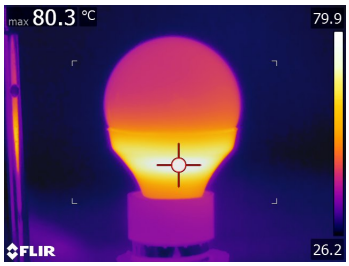

(g) Obi

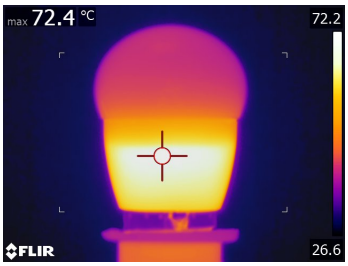

(h) Osram

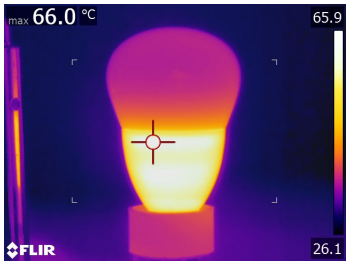

(i) Philips

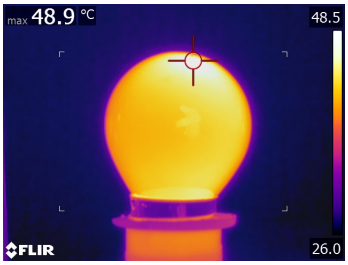

(j) Wiva

Figure 8.24: Thermal images of the lamps.

8.3.3 Electronic converters

Why use the converters? Is necessary to rectifier and adjust the tension of the network to achieve values proper to provide the right current over the threshold voltage of the LEDs, but generally a passive rectifier introduces harmonics, figure 8.25 in order to control the light intensity, average current, to protect the user from hazards and allow a rational use of energy (renewable).

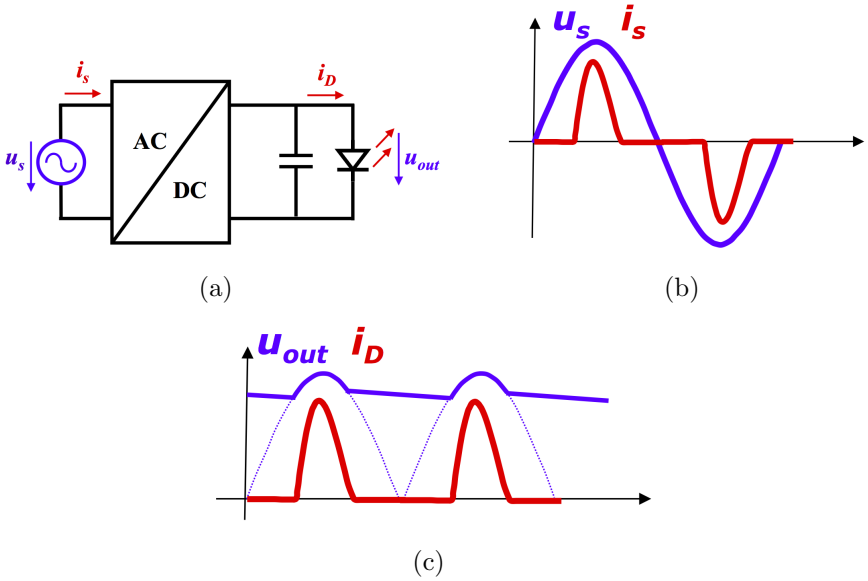

Figure 8.25: Block diagram of a simple converter a), input waveform b) and output signal c)

A typical classification for the converters is by power. From 3 W to 10 W the converter is an integrated single stage converter, current control (primary or secondary) without intensity variation designed for replacing incandescent lamps and decorative lighting, then from 10 W to 50 W AC/DC single-stage converters with intensity control and chromaticity for again replacing incandescent lamps and indoor or outdoor decorative lighting, for powers starting from 50 W and over the drivers are designed for AC/DC mono/multi-stage with intensity control and chromaticity properly used for public, industrial lighting and for example shopping centers. Then finally for solar application converters DC/DC charge/discharge battery with LED and photovoltaic Maximum Power Point Tracking (MPPT) devices.
The figure 8.26 shows two typical configuration of non-isolated converters designed for low power applications < 10 W.

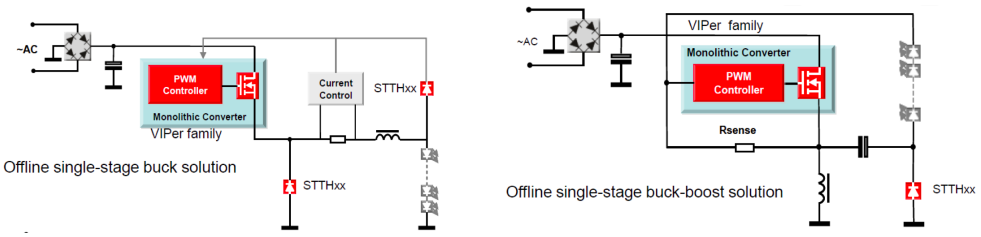

(a) (b)

Figure 8.26: Offline single stage drivers configurations

These converters are suitable for bulb replacement and lamp retrofit applications, the AC/DC solution for LED driving are *Buck*, *Buck-Boost* and *Flyback* configurations. For medium power 10 W to 50 W the figure 8.27 showS isolated Flyback configuration typically used.

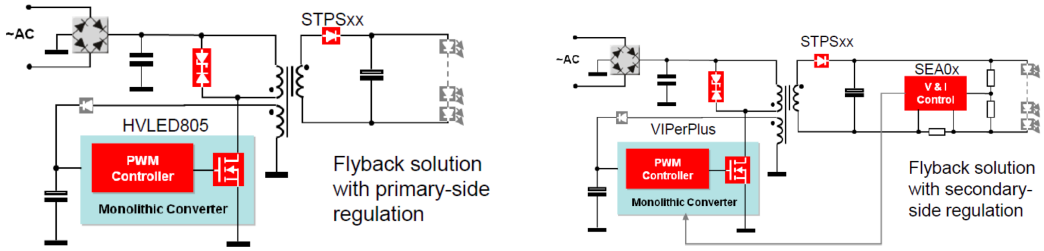

(a) (b)

Figure 8.27: Flyback primary a) and secondary b) stage drivers configurations

The main application for these converters are: tube lamp and bulb replacements, architectural and decorative lighting than finally street lighting, the AC/DC solution for LED driving is *Flyback*. For high power $>$ 50 W converters the figure 8.28 shows the isolated configuration.

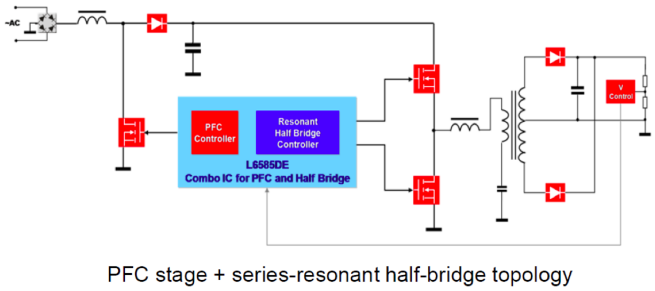

Figure 8.28: Power Factor Correction (PFC) and resonant half-bridge.

The key features of the PFC + resonant half-bridge topology, are the extended temperature range, zero voltage switching and symmetrical topology, post-regulation with dimming solutions and EN5015d EN61000-3-2 compliant, the main benefits of

this converter topology is suitable for outdoor applications, very high efficiency > 92%, dimmable solutions and satisfies the relevant lighting regulations.
The commercial lamps converters are thus studied, mainly the dominant configuration is the not isolated <10 W and only in two cases the not isolated 10 W to 50 W solution was adopted. For each lamp will show the circuit.
The figure 8.29 a) shows the Aster model schematic, carachterized by a bridge rectifier and a current passive filter with a capacitor and resistance in parallel to regulate the right amount of Leds current no PWM controller, 8.29 b), the source head is composed by 8 LEDs in series. This configuration is often used for many lamps studied.

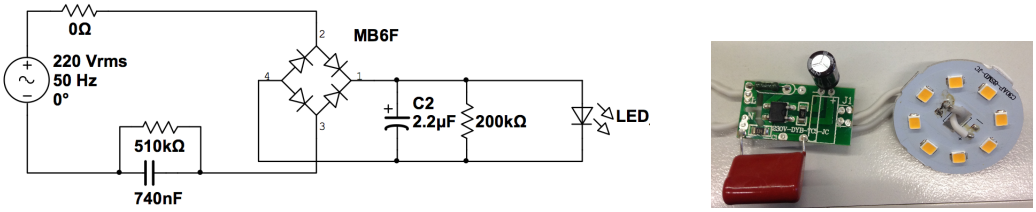

(a) Aster (b) PCB

Figure 8.29: Schematic of the converter a) and picture of the components and LEDs.

As for the Aster also as is possible to see the figure 8.30 the basic schematic is analogue to the model above, one interesting particularity is the shape of the PCB 8.30 c) as to emulate and input inductance right after the AC supply contacts. The number of LEDs connected to this electronics is 24 LED in series.

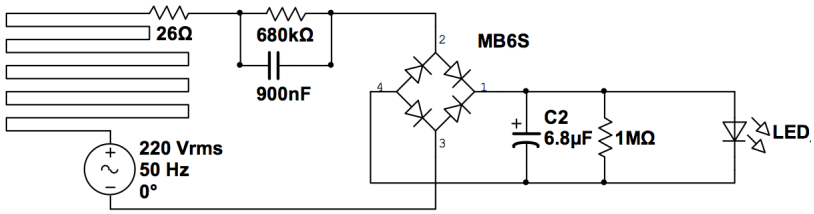

(a) Beghelli

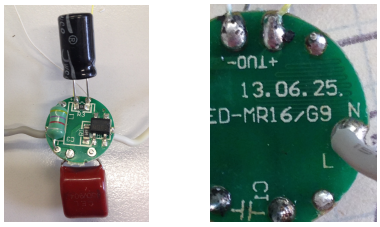

(b) Front (c) Back

Figure 8.30: Schematic of the Beghelli converter a) the front of the PCB b) and the back c).

The figure 8.31 shows that the circuit design for GE lamp follow the *Flayback solution with primary-side regulation*, as mentioned before this architecture is typical used for powers between 10 W to 50 W. Probably this configuration is not perfectly suitable for this application but the electric to optical signal quality conversion , as showed in the following paragraph 8.3.4, is good.

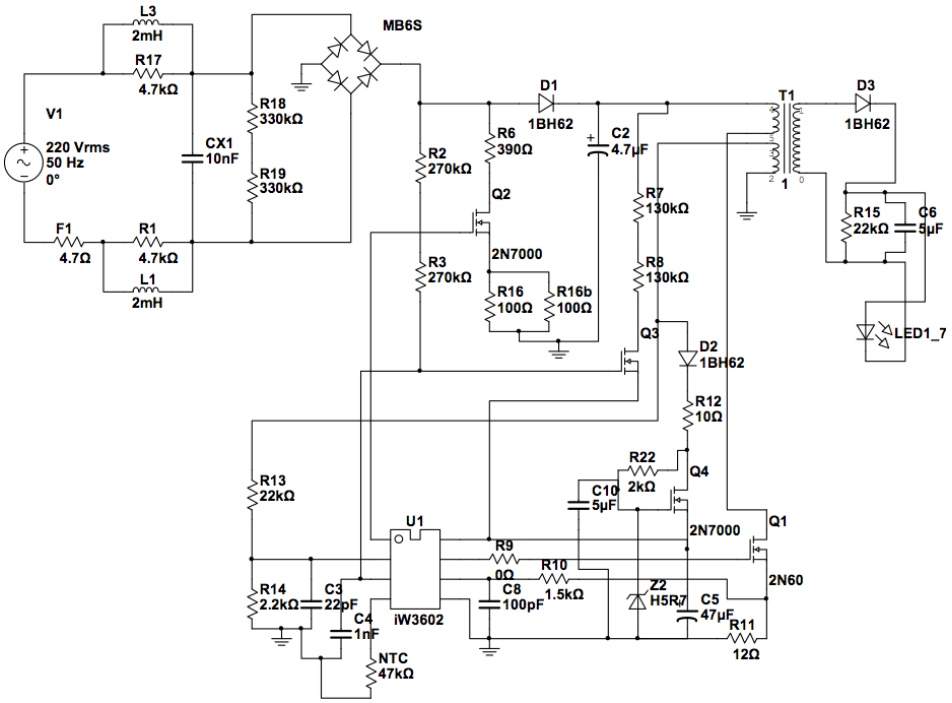

(a) Ge

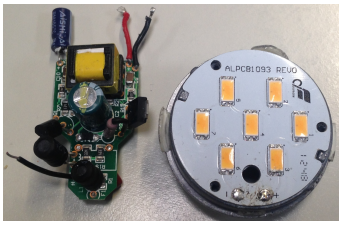

(b) Front

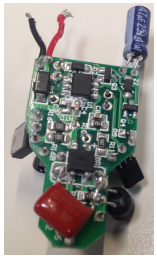

(c) Back

Figure 8.31: Schematic of the Ge converter a) and picture of the components and LEDs.

The figure 8.32 shows the schematic of the Isy model that is analog to the Aster, with small differences concerning the passive components. The number of LED used in series is 6. Same consideration can be expressed for the Kennex model 8.33, the converters design is the same, in the case of the Kennex model the LEDs are 9. The number of LEDs influence the luminous intensity, as mentioned before, as the figure 8.21 d) and e) the luminous intensity of the Kennex, equipped with 9 LEDs, is more than 100*cd* higher respect to the Isy one.

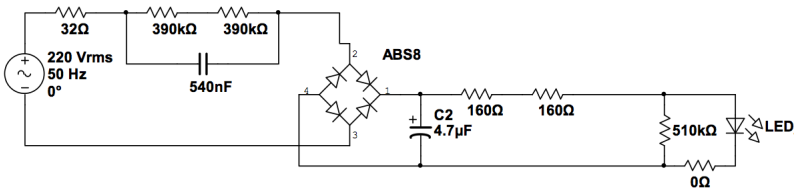

(a) Isy

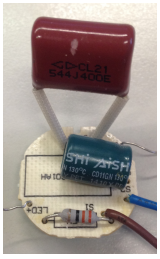

(b) Front

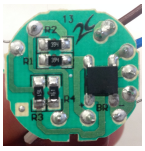

(c) Back

(d) LEDs

Figure 8.32: Schematic of the Isy converter a) and picture of the components and LEDs.

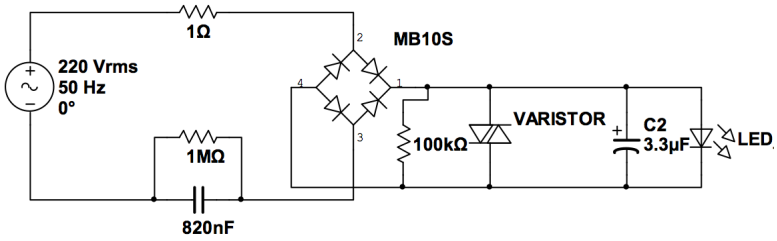

(a) Kennex

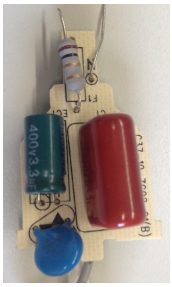

(b) Front

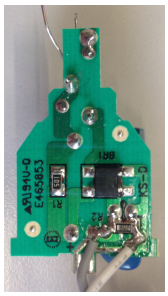

(c) Back

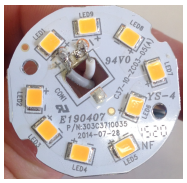

(d) LEDs

Figure 8.33: Schematic of the Kennex converter a) and picture of the components and LEDs.

In the case of the Life model, 8.34, the bridge rectifier is builded with discrete diode components unlike to the rest of the lamps that mount a solid integrated chip. For the final utilization the result is analog to the integrated choice. The Obi model circuit, in figure 8.35, follow the not isolated solution with a bridge rectifier chip integrated as the most schematics adopted in the lamps studied.

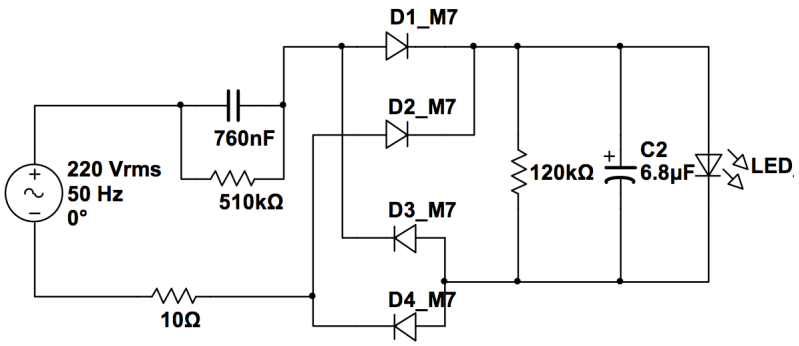

(a) Life

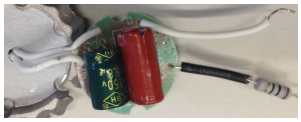

(b) LEDs

Figure 8.34: Schematic of the Life converter a) and picture of the components and LEDs.

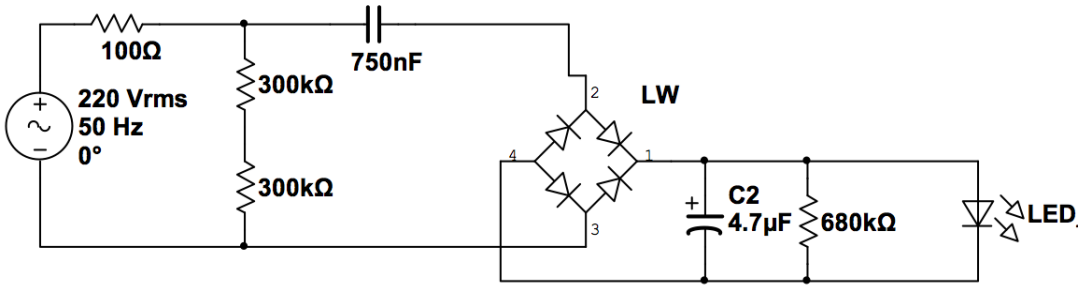

(a) Obi

(b) Front

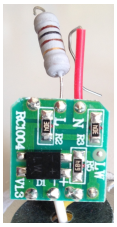

(c) Back

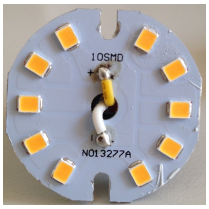

(d) LEDs

Figure 8.35: Schematic of the Obi converter a) and picture of the components and LEDs.

As for the GE model also Osram, 8.36, adopted the *Flyback solution with primary side regulation*, the converter is not designed for these power configuration otherwise has a good ability to filter electric fliker disturbs from the supply net.

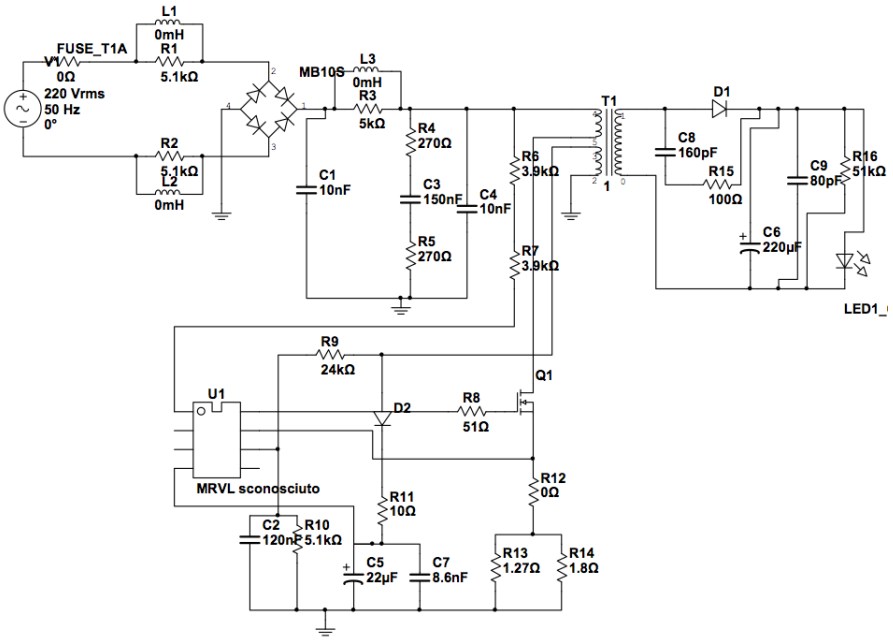

(a) Osram

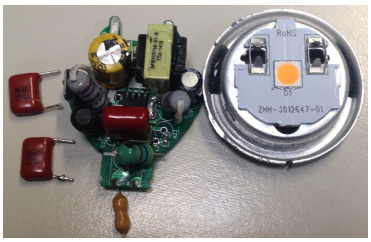

(b) Front & LEDs

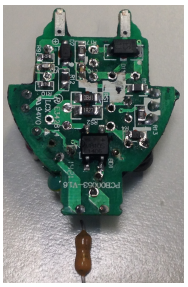

(c) Back

Figure 8.36: Schematic of the Osram converter a) and picture of the components and LEDs.

The Philips design circuit, 8.37, is a simple *Offline single-stage buck solution* with a *Non-isolated Buck Offline LED Driver* chip. Thanks to this integrated circuit the current provided to the LEDs is constant with no fluctuation. As the following section will describe the Philips converter is able to filter all the frequencies, in the range of the test parameters.

Finally the Wiva design circuit, 8.38, follow the simple not isolated configuration adopted from the main design circuit of the lamps tested.

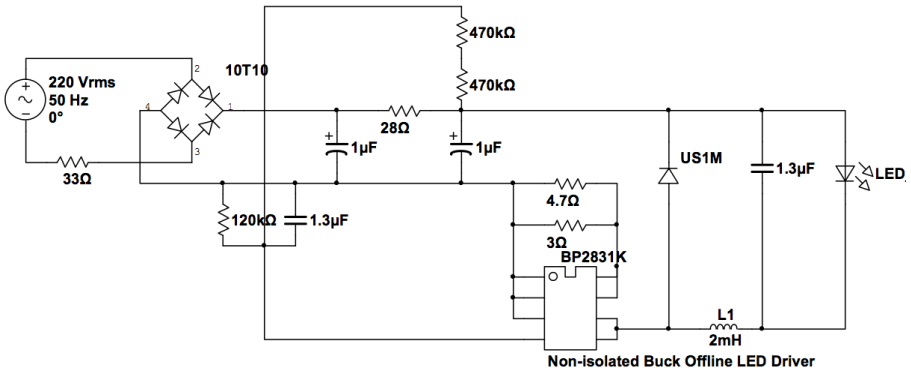

(a) Philips

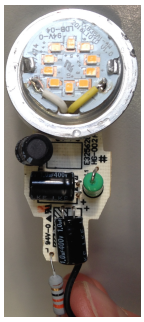

(b) Front

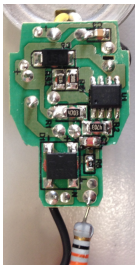

(c) Back

Figure 8.37: Schematic of the Philips converter a) and picture of the components and LEDs.

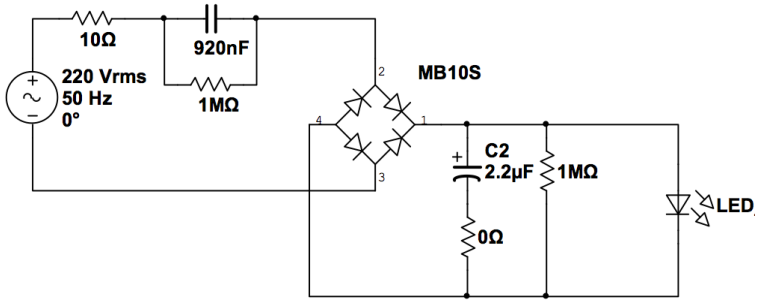

(a) Wiva

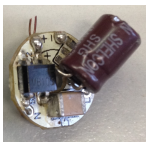

(b) Front

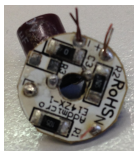

(c) Back

Figure 8.38: Schematic of the Wiva converter a) and picture of the components and LEDs.

8.3.4 Electrical characterization

The electrical characterization consists in a test designed to the observation of two LED lamps behaviors: one is closely related to the design of the converters previously

presented; the second is measuring the light emitted by the LEDs. To the supply power, 220 V to 50 Hz, has been added high and low frequency components to test the filtering goodness of the electronic devices, by using a dedicated power source (Agilent 6813b). The final goal is to measure, with fast photodiode (FEMTO-OE-200-IO-Fast, FEMTO) and a 32-channel spectrometer (HAMAMATSU H8353), the spectrum of light emitted by the GaN LED to quantify the visual sensation induced by the light stimulus fluctuations with time, the flicker 7.2.
The test consists of two measuring campaigns: 1 with low frequencies, from 2 Hz to 20 Hz with a step of 2 Hz, overlap with the power supply at 50 Hz; in the second campaign of measures it has been superimposed high frequency electric signal,160, 490 and 950 Hz. Thus the generated light stimulus was acquired through the instrument, described earlier, connected to two different optical fiber to access at the completely obscured environment where is located the lamp under test. For each bulb spectrum was acquired for 2 seconds with the Hamamatsu, and for a second with the Fempto. The data acquired with the fast photodiode are analyzed by performing Fast Fourier Transform (FFT) and highlighting the frequency response of the emitted light. Furthermore, the data provided by the spectrometer are elaborated to obtaining the optical spectrum for each frequency, in case of low frequencies, and the normalized amplitude of the FFT in function of the wavelength and frequencies, for high frequencies. The FFT obtained for high frequencies is normalized by the FFT of the 450 wavelength, typical for GaN LEDs, in order to evaluate a possible influence of the frequencies on the time response of the phosphors. Regarding the two experiments are reported the most significant cases over the 10 LED lamps and confronted with an obsolete incandescent light bulb 100 W and a quasi-obsolete fluorescent lamp of 20 W.

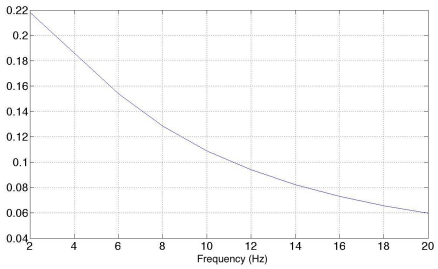

(a) 100 W

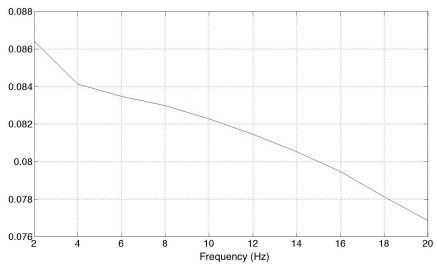

(b) Fluorescent

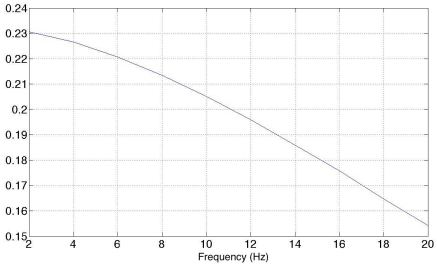

(c) Beghelli

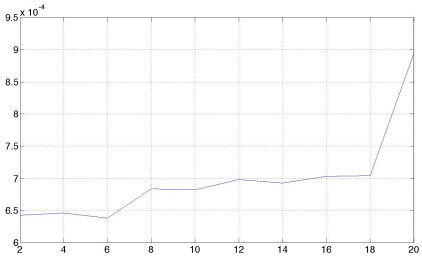

(d) Philips

Figure 8.39: Normalized frequency response for each frequency tested.

Experiment 1 (Low Frequencies): The figure 8.39 shows the maximum amplitude of the FFT, calculated for each frequency, and then summarized in a graph for each lamp. The figure a) the incandescent lamp behaves as a natural low pass filter, gradually decreasing the amplitude to values around to 0.16 for frequencies of 20 Hz. The amplitude in the case of the fluorescent lamp b) is very low, also this source is behaving like a lowpass filter. The situation changes significantly in the case of the Beghelli LED lamp c), in which it can be seen that the amplitude of the FFT is very high even at 20 Hz, with a small reduction. Finally, the situation has been change significantly for the Philips LED lamp in which the width is several orders of magnitude lower than those previously seen. The difference takes place in the design of the the converters of the LED bulbs that determines the quality of the outgoing optical beam. From this point of view, the LED light bulb Beghelli behaves even worsely compared to an incandescent bulb.

Figure 8.40 shows the spectra of the lamps for each Flicker frequency. The

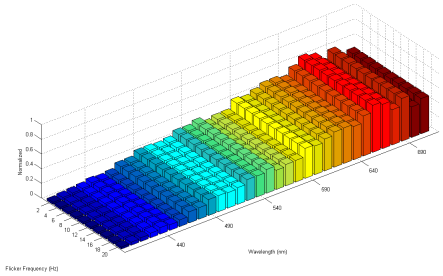

(a) 100 W

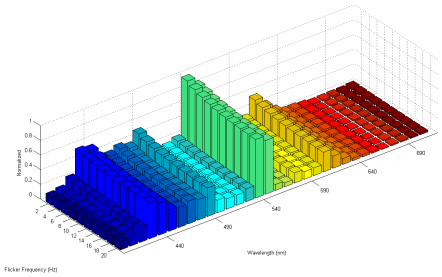

(b) Fluorescent

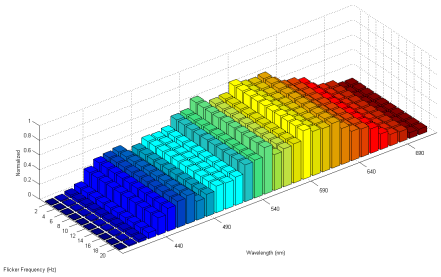

(c) Beghelli

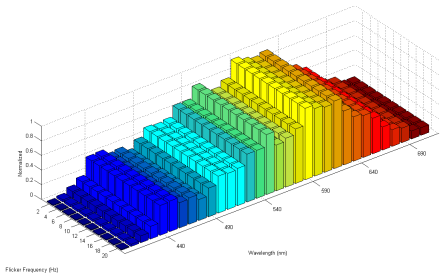

(d) Philips

Figure 8.40: 3D spectrum of the lamps for each frequency.

spectral components of each lamps do not vary with the frequency. The differences between the spectra are strictly related with the nature of the optical source.

Experiment 2 (High Frequencies): has been chosen three frequencies, 160, 490 and 950 Hz, to be superimposed to the standard power supply frequency to observe the reaction of the light sources and observe if high frequency could cause the flicker effect. The graphs shown in the following figure are not easy to interpret, each of the 32 channel FFT is normalized with the FFT of 450 nm channel, typical frequency of the Gan LED.

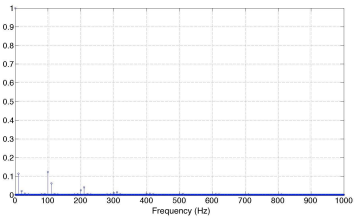

(a) 160 Hz

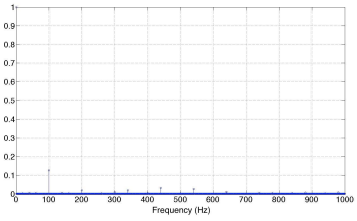

(b) 490 Hz

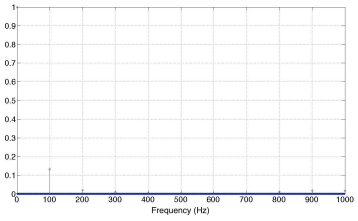

(c) 950 Hz

Figure 8.41: Frequency response of the Beghelli lamp.

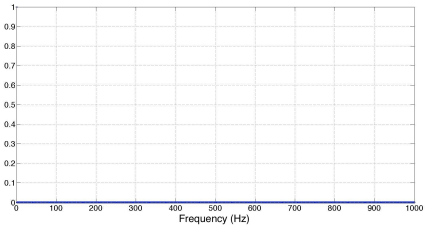

(a) 160 Hz

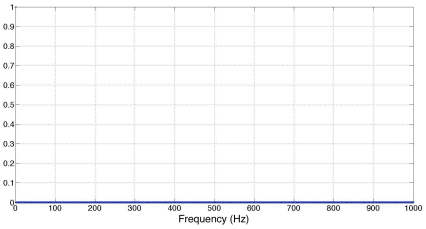

(b) 490 Hz

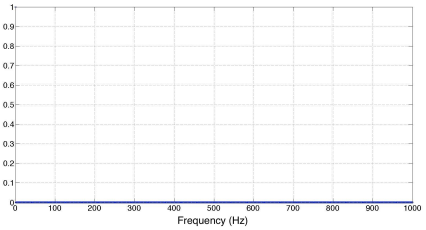

(c) 950 Hz

Figure 8.42: Frequency response of the Philips.

In the Figure 8.41 is possible to observe the FFT for Beghelli source. As you can observe the resulting frequencies are varied, it can be inferred that the electronics of the device is not quality to ensure a light beam without flicker. On the other hands the spectra presented for the lamp Philips does not have any frequency component. Although as it can be seen in the figure 8.42 a frequency component has been detected by the spectrometer. The resulting spectral component is very low and not perceptible, by the observation of the experimental data is evident that the spectrum is almost continuous and therefore absent of flicker. The figure 8.43 shows that can occur frequencies different from those used to power the device as shown before. This interaction between the supply and the superposed high frequency than normalized with the FFT of the 450 nm channel.

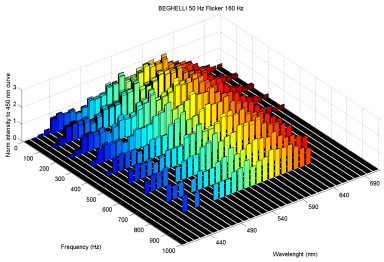

(a) 160 Hz

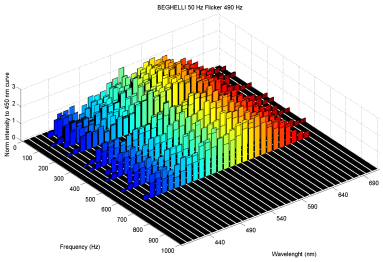

(b) 490 Hz

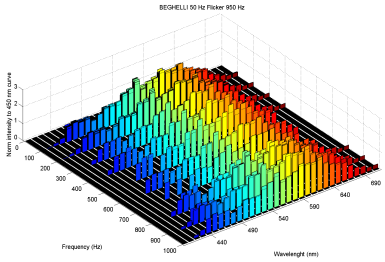

(c) 950 Hz

Figure 8.43: Frequency response, normalized with the 450 nm FFT, in function of the wavelenght of the Beghelli LED lamp.

The normalization for the frequency spectrum corresponding to the channel at 450 nm allows to process the data to observe if the spectrum assumes changes with the frequency. It is also interesting to observe that the obtained frequencies are compositions of the frequencies used to induce flicker with the 50 Hz of the supply power. It is evident that the Philips LED lamp presents some frequencies components but as it has been reported in graph 8.44 the contribute is absent thanks to the electronics that are able to filter any frequency, what the graph snows is an amplification of background noise and in evidence a 100 Hz generated by the electronics of the lamp that rectifier the 50 Hz of the power supply.

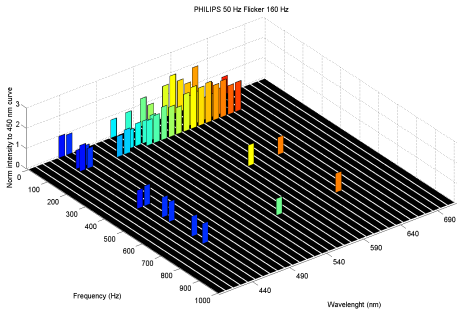

(a) 160 Hz

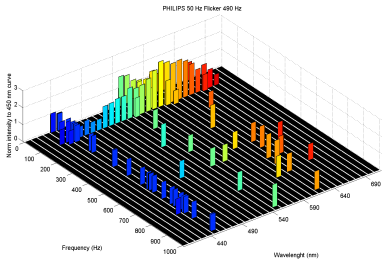

(b) 490 Hz

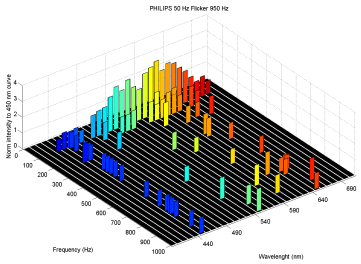

(c) 950 Hz

Figure 8.44: requency response, normalized with the 450 nm FFT, in function of the wavelenght of the Philips LED lamp.

The final goal of this analysis would be to observe high-frequency optical time changes contribution of phosphors. They have a decay time that depends on the type of phosphor, the chemical composition The lamp used at high frequencies it may occur in a sort of color temperature change. As the graphs shows the spectrum plotted has the same normalized amplitude for each frequencies, probably to see differences of color temperature caused by the time decay of the phosphors is necessary to induce a flicker with higher frequencies.

8.4 Eye model response due to a flicker stimulus

This section is focused on the explanation of the novel, binocular model of the pupillary light reflex and on its implementation in Simulink developed. First, a general view of the model is given, and its general working principles are explained. It is explained that some key elements are the spectral sensitivity of the photoreceptors placed on the retina, the modulation inputs from both parasympathetic and sympathetic systems and the iris muscle mechanical properties. It is evinced how the model puts together the response of the retina containing the four classical photoreceptors: rods, S-, M-, L-cones, and one novel melanopsin-containing ipRGCs, which contributes to the circadian rhythms, with a dynamical answer of two antagonist muscles: the dilatator and the constrictor determined by the interaction of the parasympathetic and the sympathetic nervous system, which take into account the intrinsic non-linarites of this complex system. Then, each block is explained into details and it is given an insight into the modeling of each component of the pupillary light reflex. Finally, the pupillary polychromatic response will be modeled and the obtained curves are reported.

8.4.1 Main Blocks

Three main blocks describe the pupillary light reflex pathway in the proposed model. The controlled variable is the *pupil area*, thus the amount of light that reaches the retina and this is possible thanks to the opening or closure of the diameter of the pupil, reaction driven by the muscles placed into the pupil iris. The pupillary system dynamic, nonlinear, with negative feedback and an overview of the general control system of the PLR is shown in Fig. 8.45.

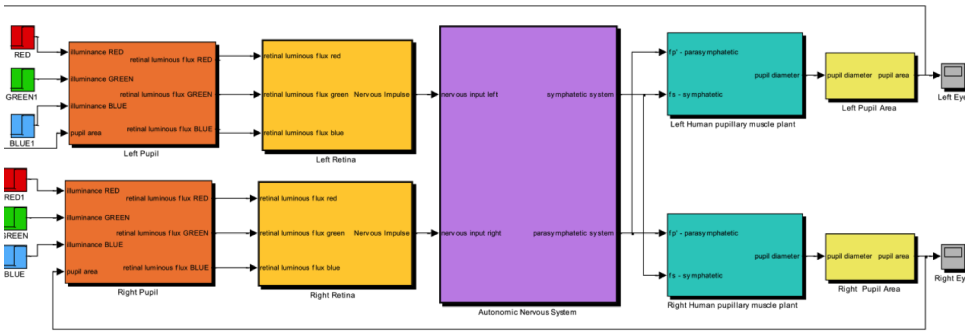

Figure 8.45: Main blocks of the Eye model.

The values of luminance are the input variables of the model for each of the three main colors: green, red, blue (RGB). The input luminance of the RGB light allow to create different levels of intensity for each color, than select all the color desired by

mixing the RGB input signals. The *pupil diameter* is the parameter which controls the amount of light on the retina. The mail block that identify the model are:

1. *Pupil* (Left and Right)
2. *Retina*
3. *Autonomous Nervous System*
4. *Human Papillary Plant*
    - *Model of the Sphinter Muscle*
    - *Model of the Dilator Muscle*
5. *Pupil Area* (Left and Right)

The first blocks, named *Pupil* (Left and Right) in orange, calculates the irradiance on the retina as a function of the colored light stimulus (RGB blocks) and of the pupil area, as feedback calculated as a trivial function of the diameter by the last block called *Pupil Area*, and gives as an output a luminous intensity. The other main blocks are the *Retina* (Left and Right) in dark yellow, which converts the light stimulus as illuminance into an electric signal, that travel to the *Autonomous Nervous System* block in violet, which converts the electric stimula from the retina into signals proper for the muscles controls, the outputs of the block run both into the mechanical model of the iris for both eye (*Human Papillary plant* blocks in green), which converts the nervous stimuli into the pupil diameter, finally in the *Pupil Area*, blocks in yellow, from the diameter we obtain the area approximating the pupil as a circle.
The model, developed in Simulink environment, require to setup properly the configuration parameters, specially the solver with a discrete fixed simulation steps for more accurate, but slow, results.

8.4.2 Pupil Block

The first block of the model simply calculate the luminous intensity on the retina by multiplying the luminance of the RGB stimola, the inputs of the model, with the area of the pupil. The figure 8.46 shows the process in the block. The area of the pupil is a feedback signal provided from the *Pupil Area* block, is the output signal of the model, for each eye, that is routed to the input port of the model to regulate the amount of the light intensity on the retina.

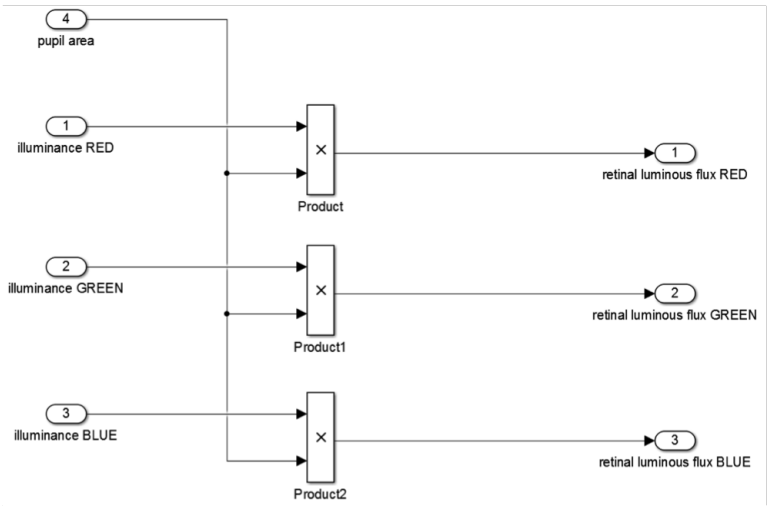

Figure 8.46: Pupil block of the model.

8.4.3 Retina Block

This block implements the response of the retina due mainly to the reaction of the photoreceptors to the light stimulus. In the chapter xxx it has been explained the physiology of the retina, the different types of photoreceptors and the spectral sensitivity theory. The spectral sensitivity is the fundamental concept at the base to model this block, every photoreceptor has a specific reaction to light that can be modelled. The *Retina Block* is composed by three sub-blocks, as the figure 8.47 shows, that receive as input the peak wavelengths of the light source and the luminous flux of the light stimulus. The answer of each color block is converted into a nervous impulse and then the sum of the three RGB outputs is calculated and exploited as the input for the following block, the *Autonomous Nervous System*. It can be hypothesized that optimal selection of the light intensity, wavelength, and duration can influence the contribution of rods, cones, and melanopsin to the overall activity of the melanopsin-expressing retinal ganglion cells, which drive the pupil light reflex. Light wavelength and intensity are important differentiating parameters.

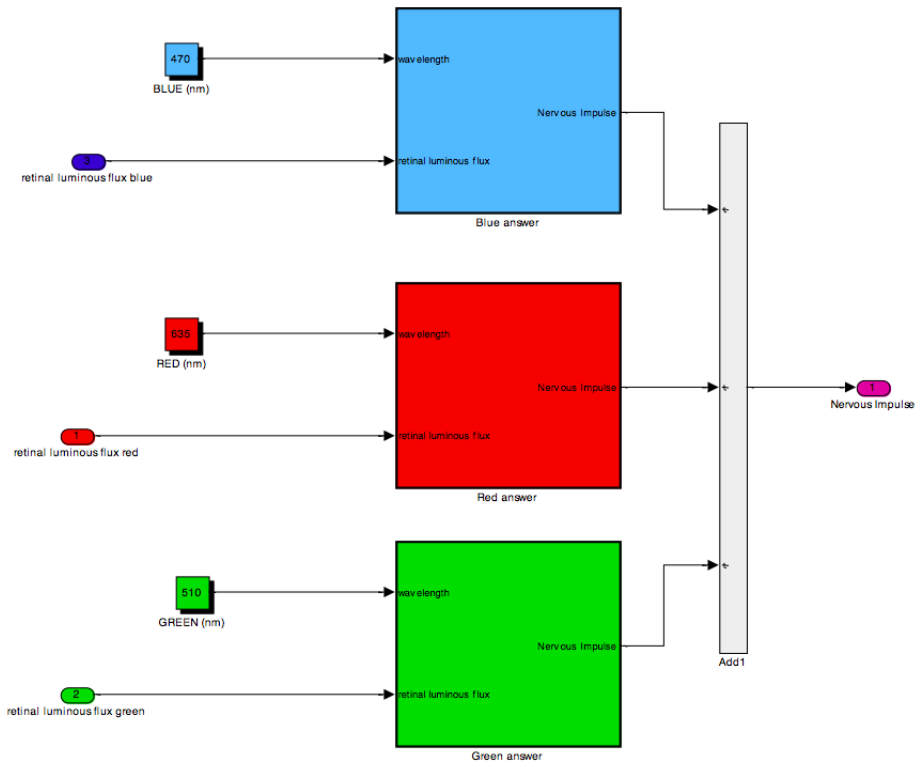

Figure 8.47: The block modelling the retina.

As in the human eye, the light stimulus has to be converted by the photoreceptors in an electric signal, as the figure 8.48 A shows the retinal ganglion cells, (ipRGC) that are connected to the outer retinal rod and cone photoreceptors via the conventional retinal circuitry. In the image are shown the major connections with one cone bipolar cells (on CBCs) connecting them to cone and, via amacrine cells (All) and rod bipolar cells (RCB), rod photoreceptors. As a consequence, the firing pattern of ipRGCs can be influenced by both intrinsic melanopsin photoreception and extrinsic signals originating in rods and each of the spectrally distinct cone classes (shown in red, green, and blue). This feature is conceptualized in a much simplified form as a number of photoreceptive mechanism depicted as R for rod opsin, M for melan opsin, SC for S cone opsin, MC for M cone opsin and LC for L cone opsin, each of which absorbs light according to its own spectral sensitivity profile, as shown in the image 8.48 B) as plots of sensitivity against wavelength from 400 to 700 nm to generate a distinct measure of illuminance. These five input signals are then combined by the retinal wiring, and within the ipRGC itself, to produce an integrated signal that is send to non-image-forming centers of the brain. As each of the five representations of weighted irradiance is produced by a photopigment with its own spectral sensitivity profile, their relative significance for the integrated output defines the wavelength dependence of this signal, and hence of downstream

responses [78].

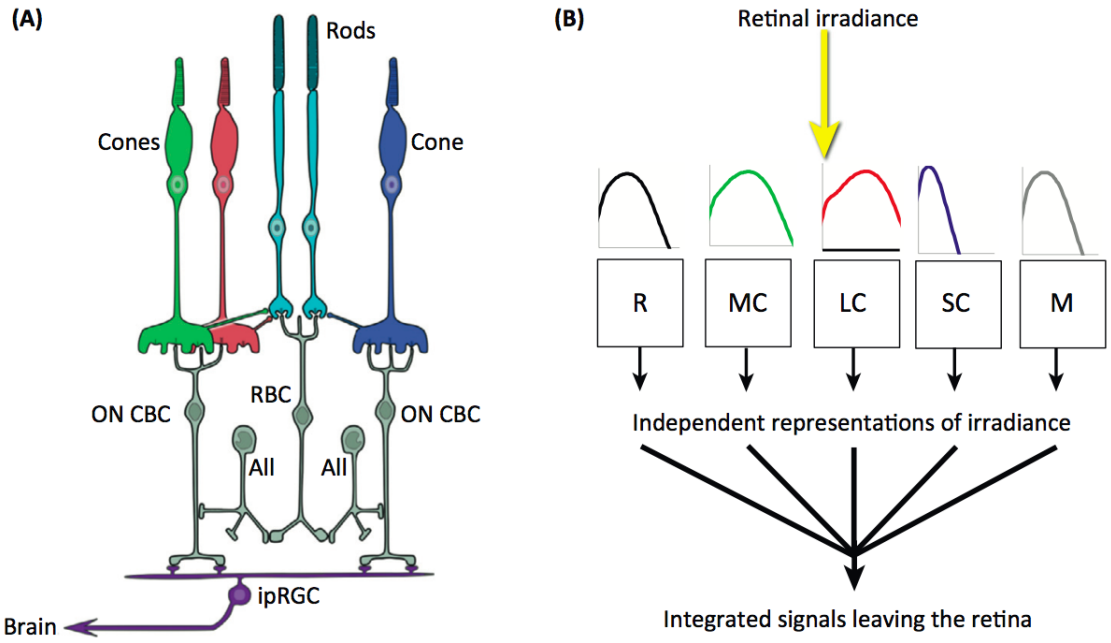

Figure 8.48: Photoreceptors and sensitivity.

The spectral sensitivity of each photoreceptor can be approximated with a gaussian distribution, in order to implement the answer of each one, the five functions have been created with a curve fitting procedure. First, five values for each wavelength have been acquired from the curve, as it can be observed for the L cones from the graph in figure 8.49 [1].

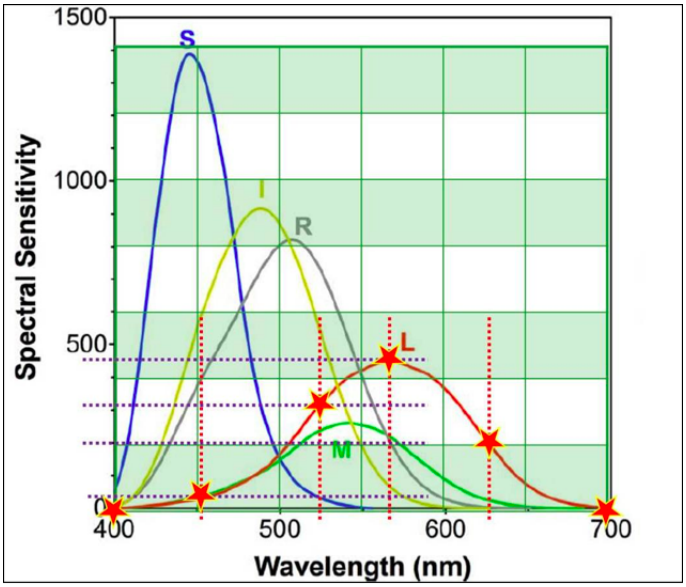

Figure 8.49: Spectral sensitivity for each photoreceptor.

Then, the X values and Y values are used for generating the distribution through the Curve Fitting Tool (Matlab), the following relative function 8.1 is used than the fundamental parameters to build the Gaussian distribution are obtained for each curve.

$$f(x) = a_1 \frac{(-(x - b_1))^2}{c_1} + a_2 \frac{(-(x - b_2))^2}{c_2} \tag{8.1}$$

One the parameters are obtained the function is implemented in Simulink, in figure 8.50 the case for L cones, the same procedure is performed for all the other four Gaussian distributions of each photoreceptor.

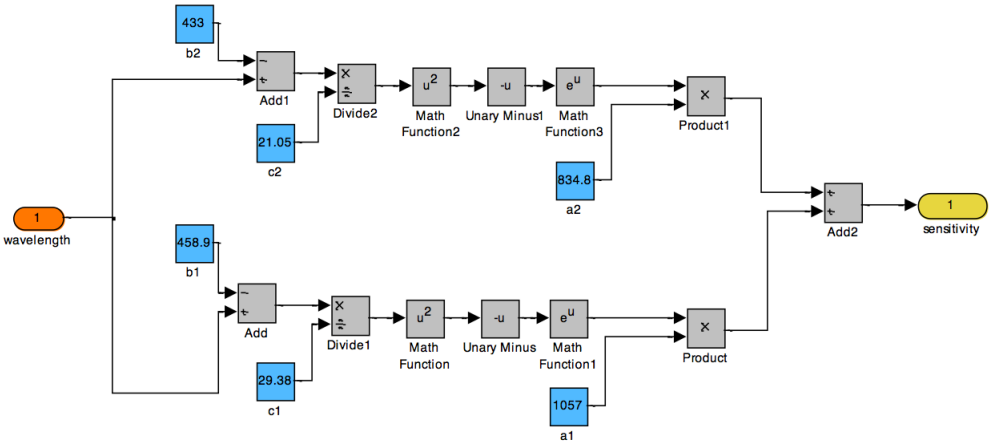

Figure 8.50: SImulink model of L cones curve of sensitivity.

The block of RGB colors contains the five photoreceptors spectral sensitivity which control the retinal luminous flux, as the figure 8.51 shows, the total contribution of the five photoreceptors is also compared to zero to avoid negative answers and then the total nervous impulse is passed to the next block of the model.

The model developed is able to calculate simultaneously the nervous signals generated by hundreds of the retinal output neurones that transmit information about the outside visual world to the brain.

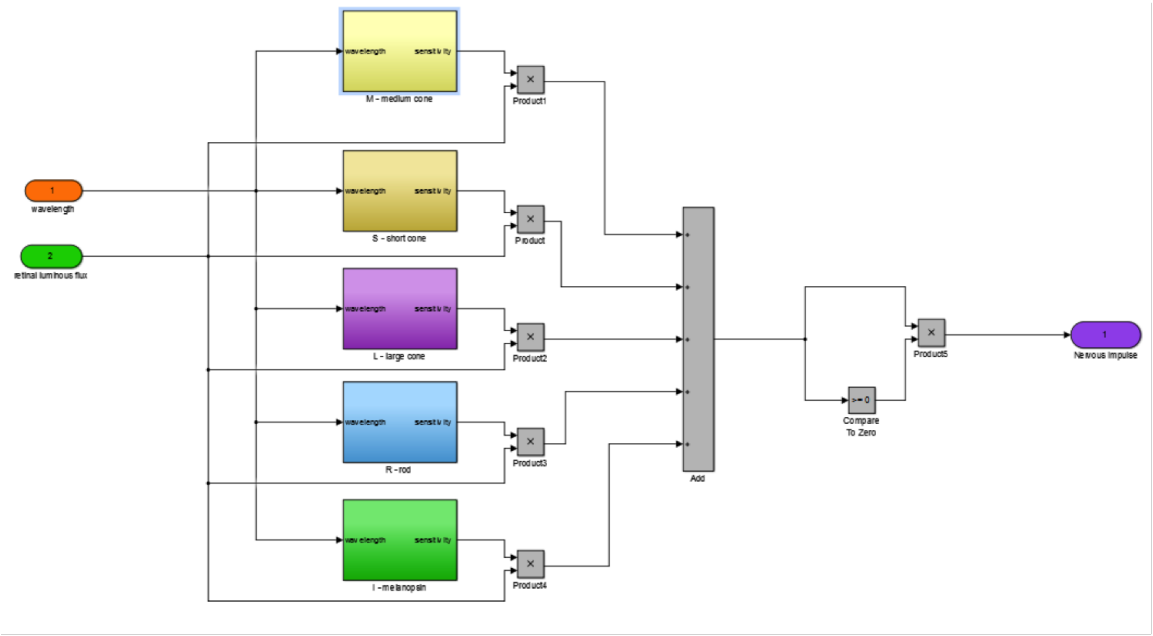

Figure 8.51: Photoreceptors spectral modulation.

8.4.4 Autonomic Nervous System (ANS) Block

Once the light has been converted into a nervous impulse the autonomous nervous system analyses this information. As it has been explained in chapters xxx the ANS is composed by the sympathetic system that innervates the iris dilator muscle and the parasympathetic system that innervates the sphincter muscle. The size of the pupil is controlled by the antagonist functions of these two parts of the autonomous nervous system. It has been demonstrated by Usui and Hirata [46] after experiments conducted on animals that the response curves of these parts of brain can be described through two antagonist sigmoid functions, as in figure 8.52. A possible method for estimate the autonomous nervous impulse to the muscle plant as described in the previous paragraph. The model generates consistent results with the experimental data and it was used to monitor autonomic nervous activity.

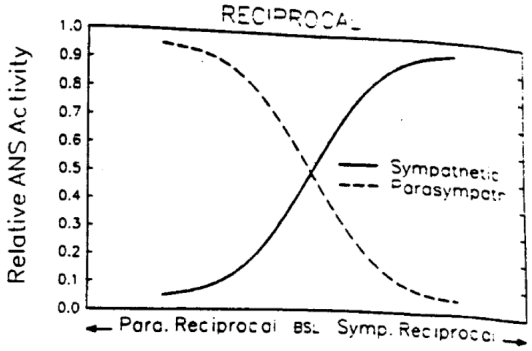

Figure 8.52: Autonomic Nervous System activity.

The nervous system controls both eyes and the effect induced on one of them can be observed on the other eye. For example is easy to see the effect o the pupil light reflex by illuminating with a white light both eyes of a subject and after 30 seconds one eye is suddenly closed: it can be clearly observed that the diameter of the other pupil (still illuminated with the same light) increases at the same simultaneously. The input of the nervous block is an average of the signals of each eye and this operation has been implemented in the left part of ANS block as the figure 8.53 shows.

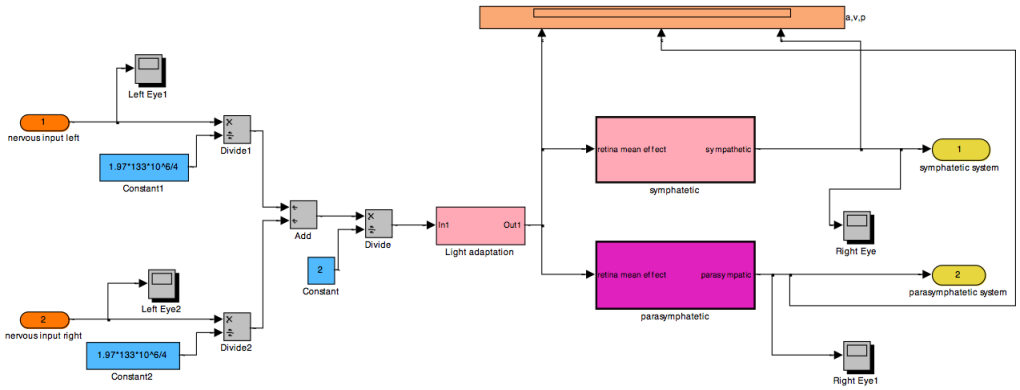

Figure 8.53: Autonomic Nervous System Simulink model.

Then, the two sigmoidal functions are implemented. To model the behaviour of the sympathetic and parasympathetic systems described in figure 8.52, is necessary to implement two sigmoidal functions that follows the shape of the ANS answer. In the specific the function that controls the parasympathetic answer is modelled with the following hyperbolic function:

$$y = \frac{tanh(\frac{x-0.5}{0.2}) + 1}{2} \tag{8.2}$$

In the figure 8.54 is possible to observe the Simulink code implementing the parasympathetic response.

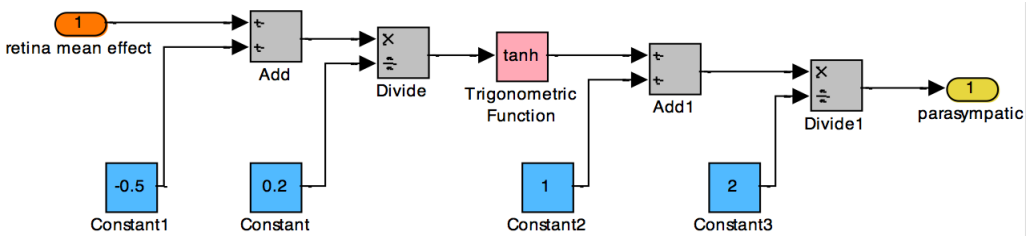

Figure 8.54: Parasymphatetic system answer Simulink model.

The same procedure was followed for the sympathetic system which is the antagonist function than the equation is expressed as following:

$$y = \frac{tanh(\frac{x-0.5}{0.2}) + 1}{2} - 1 \tag{8.3}$$

and the figure 8.55 shows the simulink code implemented for the symphatetic answer.

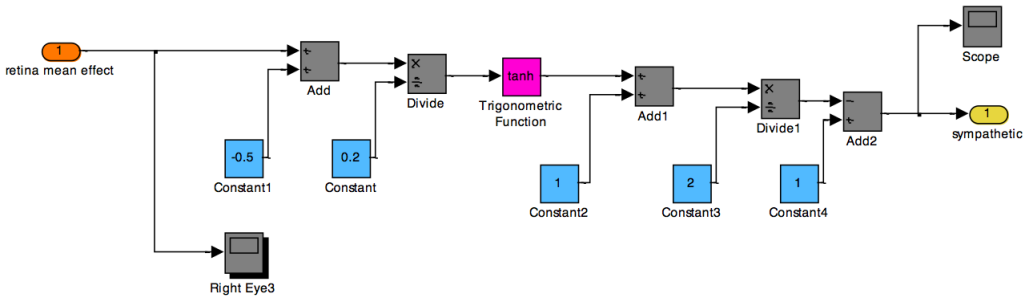

Figure 8.55: Symphatetic system answer Simulink model.

As known to achieve a stability level of pupil diameter, or area, is necessary to keep the eye under fixed condition of light or dark for a certain period. This procedure is usually called *Light Adaptation*, this behaviour of the visual system can be observed on experimental data, for example in figure 8.56, the test consist on 3 minutes of dark adaptation, than 3 minutes of fixed light stimulus than finally other 3 minutes of dark recovery. During 3 minutes of fixed light stimulus is possible to see that the pupil radius slowly increase.

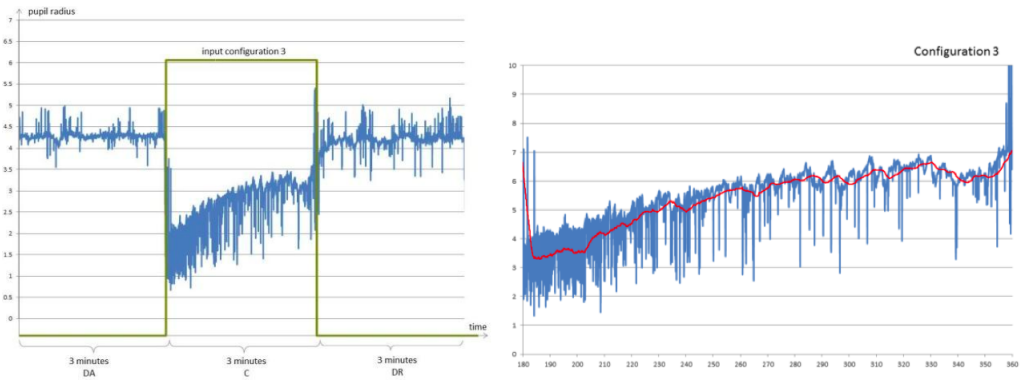

Figure 8.56: Experimemntal data on the light adaptation, on the left all the procedure test, on right the light adaptation.

This behavior has to be modeled by means of a dynamic block called light adaptation, as in the red curve. The logic of this function is to reduce the light intensity perceived by the ANS slowly, because the effect is comparable with an addiction to the light stimulus of the ANS.
To obtain a behavior close to the experimental data, a quantity of retinal stimulus is

subtracted from the initial input. If there is enough light to activate this mechanism, the first comparison block gives 1 logical as an output and this output divided per a constant (here 70), which is useful to tune the speed of the phenomenon, then it is integrated. This integration is limited and acts like a trigger because when the light is not strong enough the curve will go to zero. The last math function is used to determine the shape of the curve and the intensity of the phenomenon. The figure 8.57 shows the dynamic Light Adaptation sub-block.

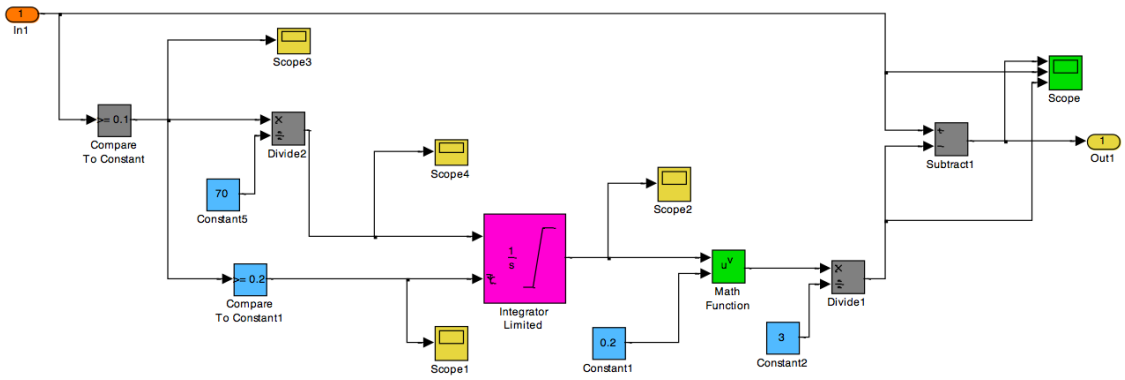

Figure 8.57: Light Adaptation Block.

8.4.5 Human Pupillary Plant

As explained in the previous chapter, anatomy and physiology of the two antagonist muscles, the dilatator muscle is placed radially and is innervated by the sympathetic nervous system. The radial muscle contracts to dilate the pupil and is controlled by the cillary ganglion and by the Edinger-Westphal nucleus of the third nerve. The parasympathetic nervous system innervates the sphincter muscles that are placed circularly these muscles contract to constrict the pupil. The superior cervical ganglion and the spinal cord control these muscles. This complex system has to be also modeled, in 1995 Usui and Hirata [46] create a model of the iris muscle using viscous and elastic components and adopting the results of skeletal muscle, the result was a new homeomorphic biomechanical model for the human pupillary muscle plant. The constrictor and dilator were modeled using the same basic mechanic units including an elastic element, a viscous element, and an active contractile element. Although the results were consistent with the observed data, this model was overly complicated with a total of 19 equations. Even with all dependent equations being combined, the model still consisted of three independent second-order delay differential equations. Therefore, it was impractical to design a robust inverse algorithm to obtain model parameters from experimental data and the ANS answer it was individuate. The sphincter and the dilator, accordingly to the model developed by

Usui and Hirata, can be modeled as a mass, spring, dumper dynamic system, figure 8.58 exploiting the equilibrium between the sphincter and the dilator tensions. E_s and E_d represent the parasympathetic and sympathetic nervous activities to the sphincter and the dilator. X is pupil radius and x_{max} is the maximum pupil radius.

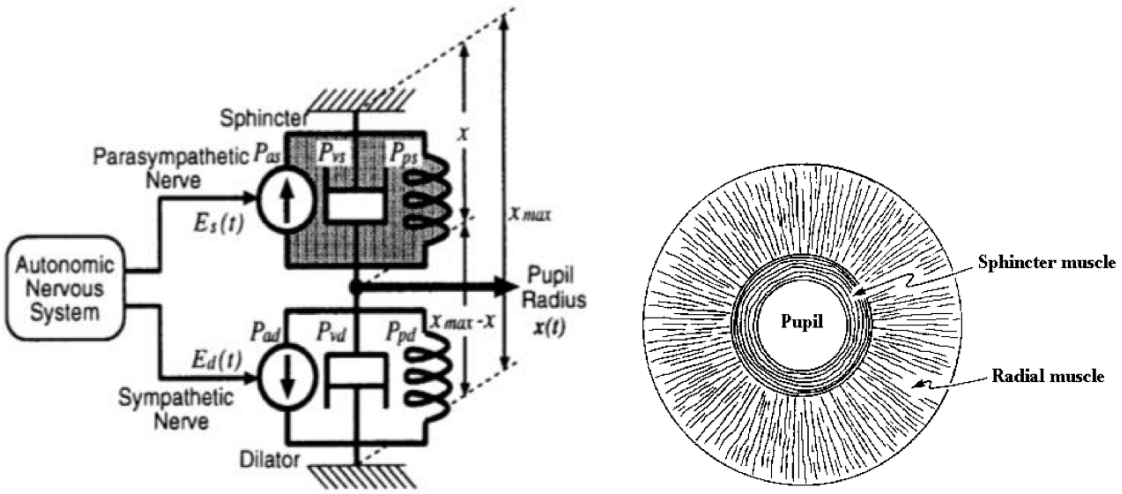

Figure 8.58: Non linear dynamical model for pupillary muscle plant.

The table 8.2 shows the principal muscles parameters involved to the pupillary light reflex.

Principal pupillary muscles reflex parameters	
Minimum constriction	1.5 mm
Maximum constriction	9 mm
Time of reaction	0.2 s
Response peaking	0.5 to 1.0 s
Circular muscle fibers	PNS (the peripheral nervous system) neurons sphincter pupillae parasympathetic innervation
Radial muscle fibers	SNS (sympathetic nervous system) neurons dilator pupillae sympathetic innervation

Table 8.2: Principal parameters of the two muscle fibers involved to the constriction and dilatation of the pupil.

The study conducted by Usui and Hirata was focused on obtaining the visco-elastic properties of the iris sphincter and dilator muscles. In order to obtain these properties, two kinds of experiments were performed: the isometric contraction experiment and the isotonic quick release experiment. The length tension relationship was obtained from the first experiment. This relationship clarified the contribution of each muscle in determining the statics of the pupil. The viscous and serial elastic

properties were obtained from the second experiment. For better understanding how the muscle and the nervous system behave together, a brief description of the reaction is presented in the next table 8.3, where the initial diameter D_{int}, the relative one δD and the muscle tensions (V_c constriction and V_d dilatation) are explained towards the arrows which can increase or decrease as the behavior of the element.

Description of the muscles-nervous system behaviour				
Parasympathetic activation	↓↓	↓↓	↓↓	↓↓
Parasympathetic inhibition	↑↑	↓	↓	↑
Sympathetic activation	↑↑	⟶	↓	↑↑
Sympathetic inhibition	↓↓	↓↓	⟶	↓↓

Table 8.3: Reaction of the muscles related to the nervous system input.

The length (pupil diameter)-tension curves of the sphincter and dilatator muscles are available thanks to the model and tests developed by Usui and Hirata. As the figure 8.59 shows, the normalized neural inputs from the sympathetic E_{dstat} and parasympathetic E_{sstat}, which are varied from the minimal 0 to the maximal 1 by 0.1 steps, act on the muscles forces and diameter of the pupil. The nonlinear functions of the two pupil muscles, sphincter and dilatator, behavior is essential to create a Simulink model. The following image represents the relation between the muscles, the nervous impulse and the diameter.

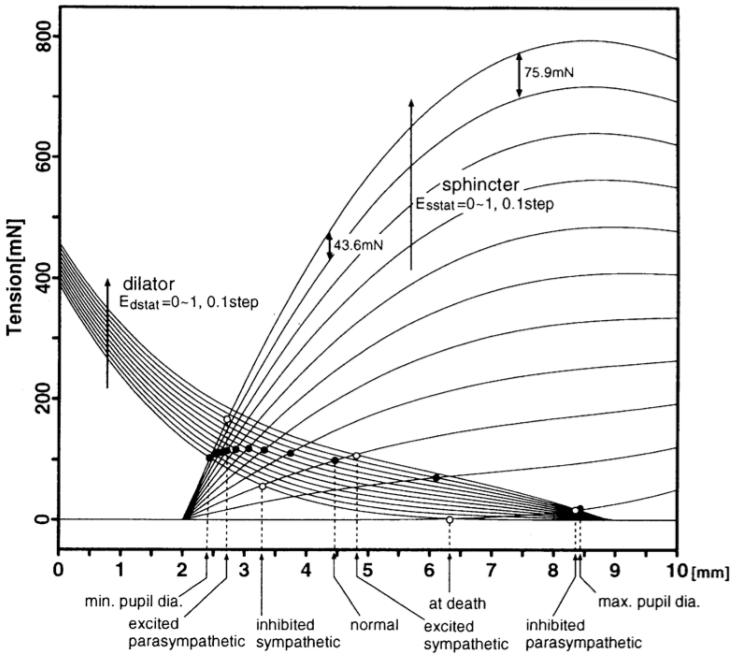

Figure 8.59: Nonlinear functions between the muscles, the nervous impulse and the diameter.

The figure 8.60 shows the Simulink model of the *Human Pupillary Plant*. This block, which describes the behavior of the human muscle's plant, receives as an input the nervous impulses from the *Autonomous Nervous System* and gives as an output the diameter of the pupil. The correct aperture of the pupil is a combination of forces acting on the muscles of the iris, this forces are of three types:

- Two active forces of the antagonist muscles
- Viscous resistance
- Inertial forces

The sum of these variables divided by the medium mass of the moving parts of the iris is the acceleration. By integrating the acceleration, the velocity is obtained and finally after another integration block the diameter is obtained. Another important parameter is the time delay which is given by the spatial distribution of the elements of the pupillary light reflex. The value of this time lag is of 180ms. This is a parameter found experimentally from tests on rabbits made by different laboratories which studied also the mechanical properties of the iris muscles. It is very interesting to observe in simulation that the oscillations obtained from the PLR answer are at the frequency of the time delay block (Transport Delay block in Simulink). The bottoming up blocks are inserted to avoid negative muscles responses.

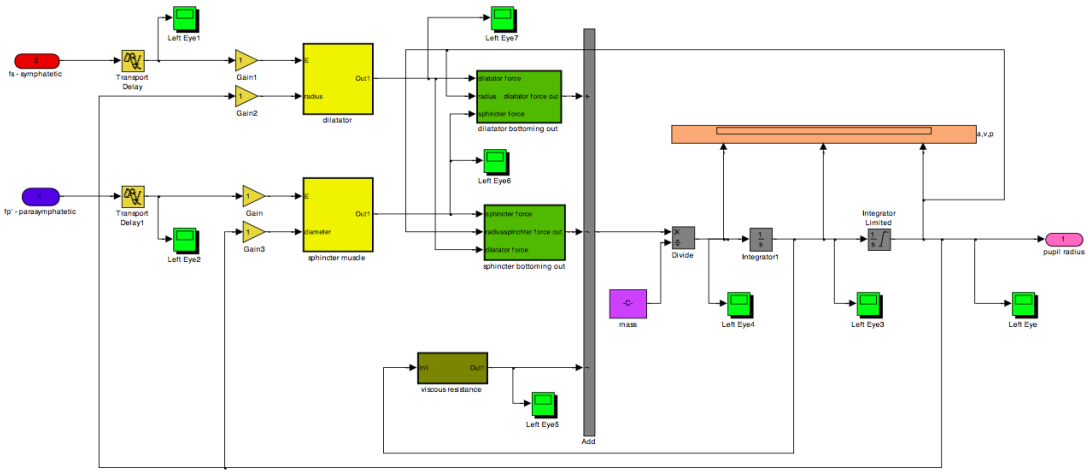

Figure 8.60: Pupillary muscle plant block in Simulink.

After a general view of the *Human Pupillary Muscle Plant* block the following sections will explain in details the most important parts of the model.

Sphincter Muscle

On the base of Usui and Hirata studies the functions that model the two forces are calculated from the curves obtained by the scientist. Two different procedures

are exploited for each muscle. Regarding the sphincter, 10 values of the forces are extracted for each step of nervous tension, as can be observed for one curve in figure 8.61.

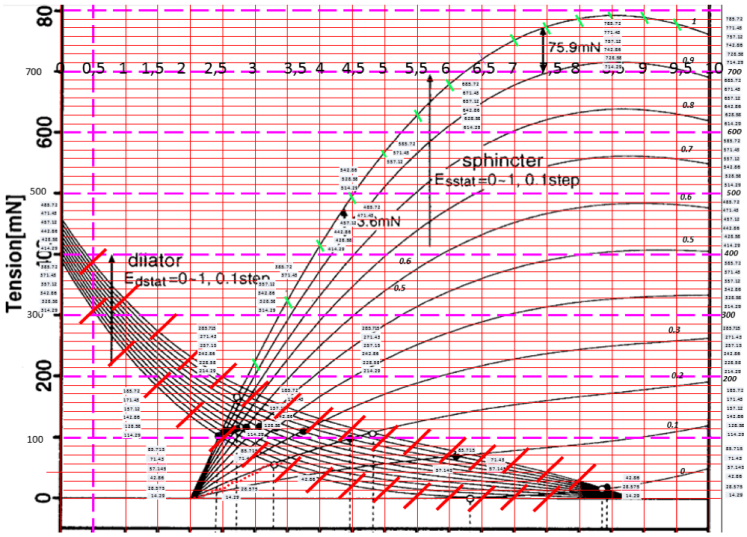

Figure 8.61: Force curves from the Usui and Hirata data.

The value extrapolated from the graph compose an array containing the values of the forces and the matrix obtained as a function of diameter and nervous impulses is calculated by using MatLab and the Curve Fitting tool, a fourth grade polynomial function is obtained and the equation is:

$$f(x,y) = p00+p10*x+p01*y+p20*x^2+p11*x*y+p30*x^3+p21*x^2*y+p40*x^4+p31*x^3*y \tag{8.4}$$

Where the variable x is the diameter y is the nervous impulse an $f(x,y)$ is the force of the sphincter muscle. The table 8.4 shows the coefficients (with 95% confidence bounds) calculated.

Coefficient of the polynomial function	
p00	28.22 (15.52, 40.91)
p10	72.72 (-86.9, -58.54)
p01	-35.34 (-55.93, -14.75)
p20	35.02 (29.96, 40.07)
p11	-0.4675 (-18.75, 17.81)
p30	-5.644 (-6.353, -4.935)
p21	38.15 (33.84, 42.45)
p40	0.2916 (0.2571, 0.326)
p31	-3.108 (-3.391, -2.825)

Table 8.4: Coefficient of the four grade polynomial function calculated for the sphincter.

Once obtained the coefficient of the polynomial function is possible to implement the model in Simulink as the figure 8.62 show.

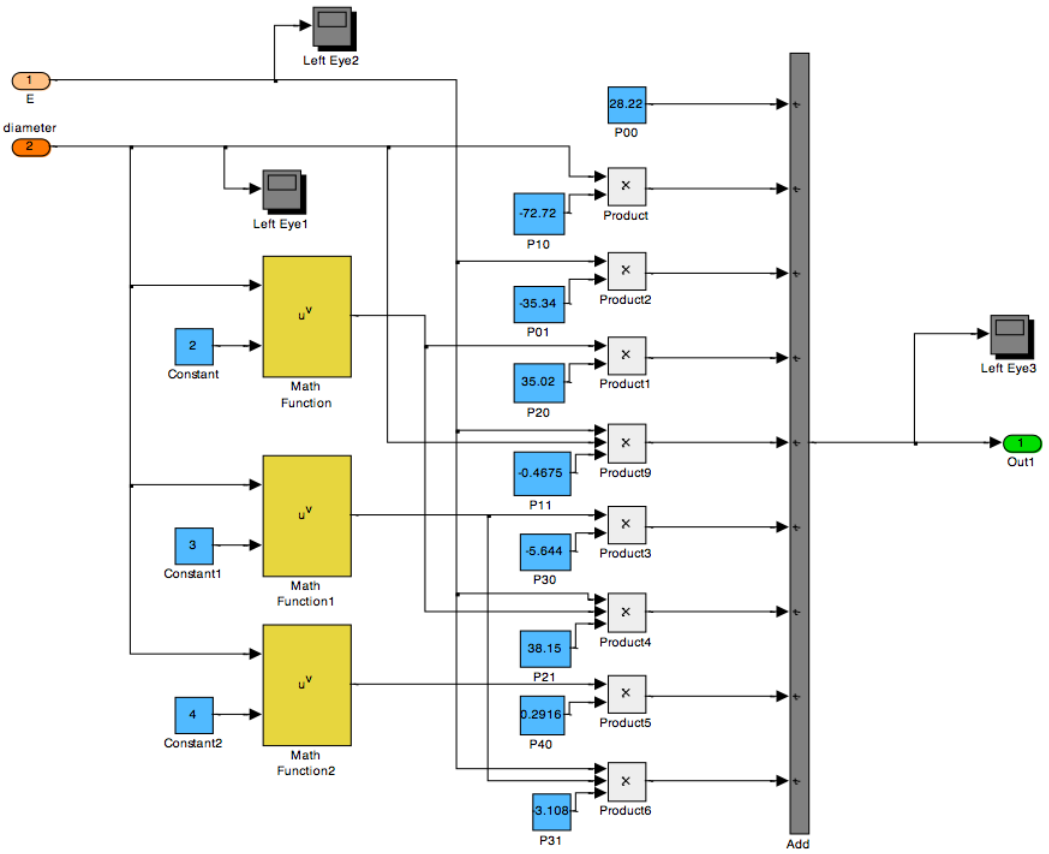

Figure 8.62: Simulink sphincter answer.

Dilator Muscle

As the sphincter muscle the same method is used for the dilator with a difference in the calculus of the force. In this case the points obtained from the curve are the ones on the minimum and maximum value of the nervous impulse, as it can be seen from the red and green dots in the figure 8.63. By using MatLab the data are elaborated but in this specific case through two for loops the interval is divided automatically in the values for each force, assuming a linear interpolating function.

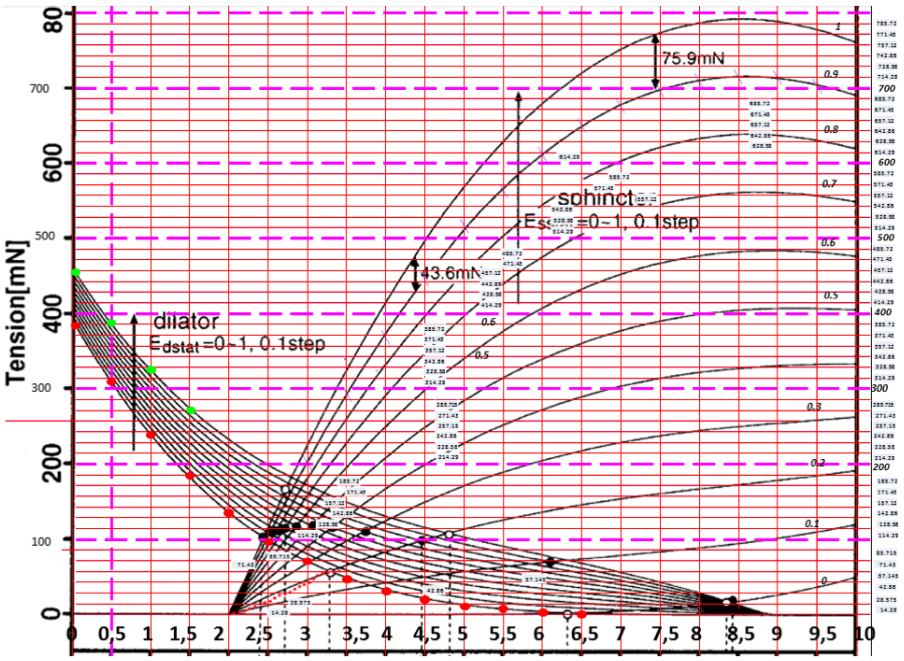

Figure 8.63: Force curves from the Usui and Hirata data.

Once obtained the array of forces value the final plot for the two forces has been obtained and also the 3D curves are presented in the following pictures 8.64 and the 3D plot 8.65:.

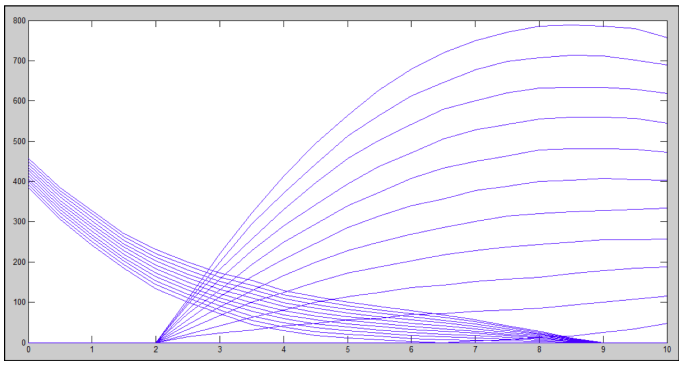

Figure 8.64: Sphincter and dilator curves.

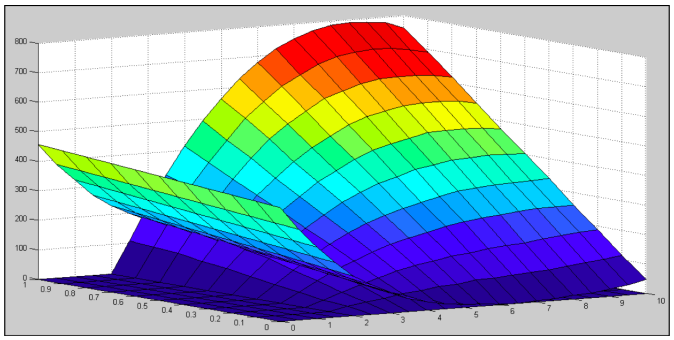

Figure 8.65: Sphincter and dilator 3D curves.

Once the force is obtained the three arrays are used in the Curve Fitting Tool in order to obtain the polynomial function of the dilatator which is next implemented in Simulink. The polynomial model is expressing the $f(x, y)$, the dilatator function related to the variable x, the diameter and y which is the nervous impulse as the following equation:

$$f(x,y) = p00 + p10 * x + p01 * y + p20 * x^2 + p11 * x * y + p30 * x^3 + p21 * x^2 * y \quad (8.5)$$

The coefficients (with 95% confidence bounds) are resumed in the table 8.5:

Coefficient of the polynomial function	
p00	376.9 (372.7, 381.1)
p10	-154.8 (-157.6, -152)
p01	74.82 (68.17, 81.46)
p20	20.59 (20.03, 21.16)
p11	15.04 (11.96, 18.11)
p30	-0.8893 (-0.924, -0.853)
p21	-2.462 (-2.76, -2.165)

Table 8.5: Coefficient of the polynomial function calculated for dilatator.

The figure 8.66 shows the polynomial function model of the dilatator implemented in Simulink.

Viscosity

As introduced before is important to model all the forces acting on the pupillary light reflex, the viscous resistance is one of them and can be expressed though the following equation:

$$F_{viscous} = sign(u) * abs(u) * k \quad (8.6)$$

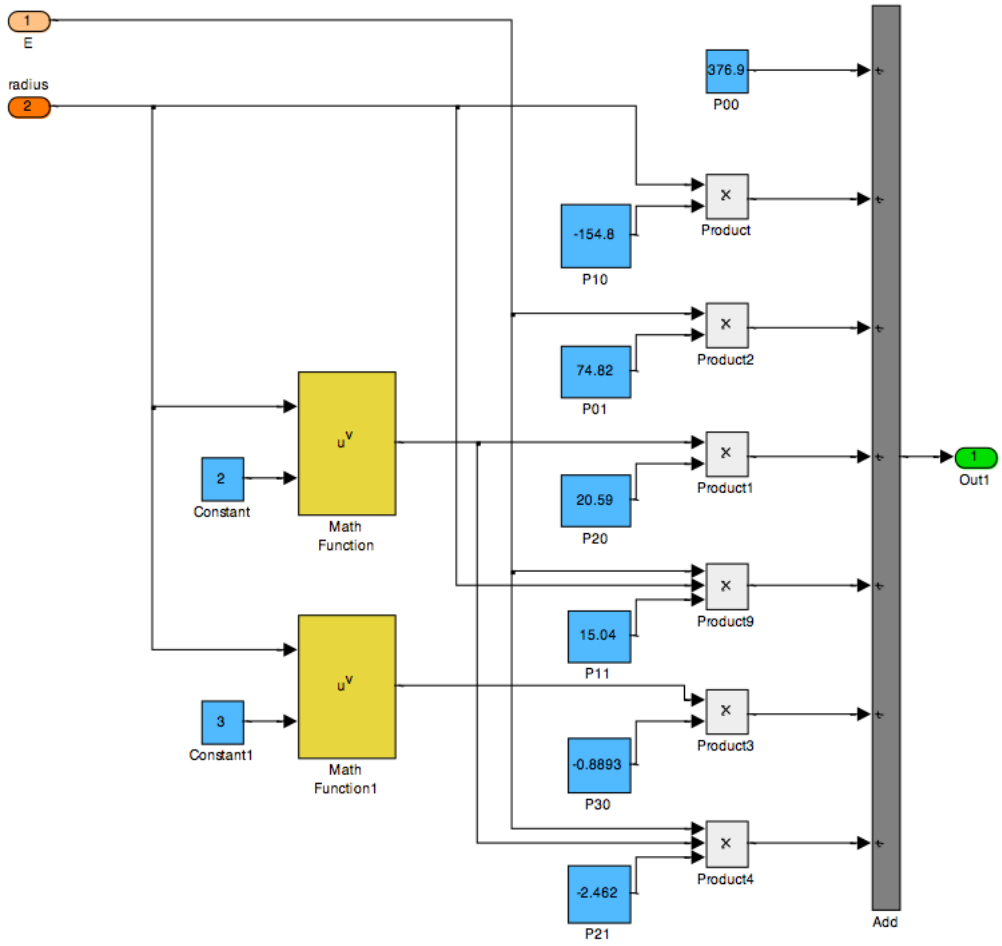

Figure 8.66: Simulink dilatator answer.

This force is a very important element, is able to determine the quality of the final pupil answer pass to the next block that calculate the final diameter. The model is a non Newtonian fluid, corresponding to a pseudoplastic fluid, with a decrease of viscosity as a function of the fluid speed. The figure 8.67 shows the model of viscosity implemented in MatLab.

Bottoming Up Block

This block is added in both muscle to avoid forces that would overwhelm the physical limits. Is a block of control on the value of forces calculated previously. The figure 8.68 shows the Simulink model of this control block.

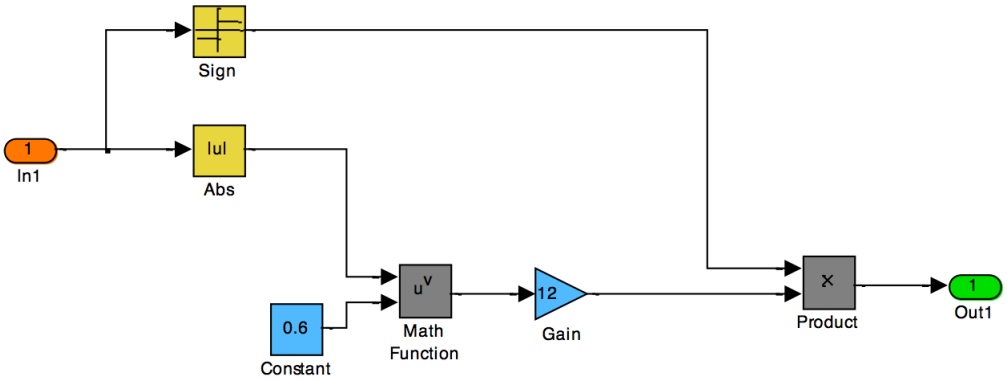

Figure 8.67: Simulink viscosity answer.

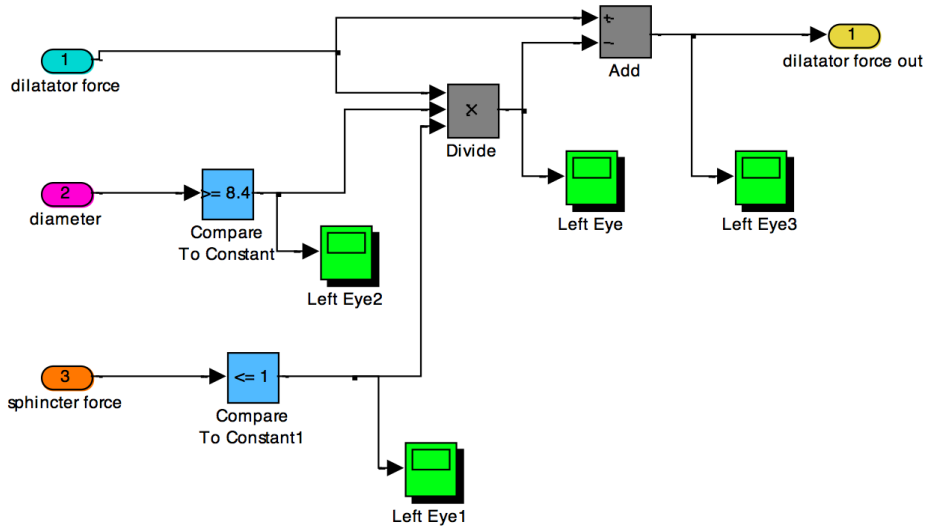

Figure 8.68: Simulink bottoming up model.

8.4.6 Preliminary Results

A repeating sequence is given as an input to the model in order to obtain the variations of the pupil diameter and to test the model. The light intensity given is shown in figure 8.69.

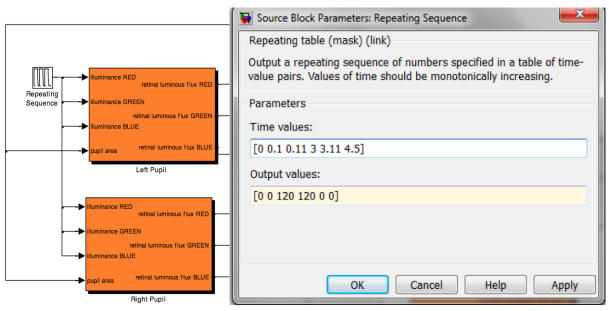

Figure 8.69: Input sequence in the configuration panel of the model.

The results obtained from the model can be observed in the figure 8.70. The x asis represents the simulation time while on the y is expressed the pupil diameter. It can be seen that the model replicates very well the answer obtained through the experimental data. At the beginning the diameter of the pupil is around 8 mm. When occur the light stimulus the pupil decreases the diameter as expected. During the period of stimulus, called light adaptation, it can be observed how the model reacts similarly to the real response and follows the function explained the previous paragraphs. When the light is turned off, the pupil increases its diameter and returns to the initial condition.

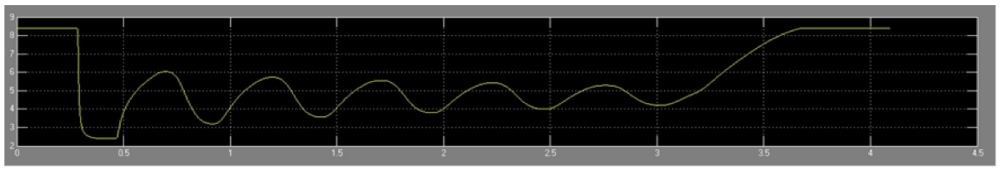

Figure 8.70: Pupil diameter responses to a colored light stimulus.

A preliminary test was done using a solver time step of 100 μs to allow the convergence of the model, the simulation time is very long, to have a fast response the test was done with 0.1 seconds of dark adaptation, 3 seconds of light adaptation and 1.5 seconds of dark recovery. The figure 8.71 shows the preliminary test protocol and the output response of the model.

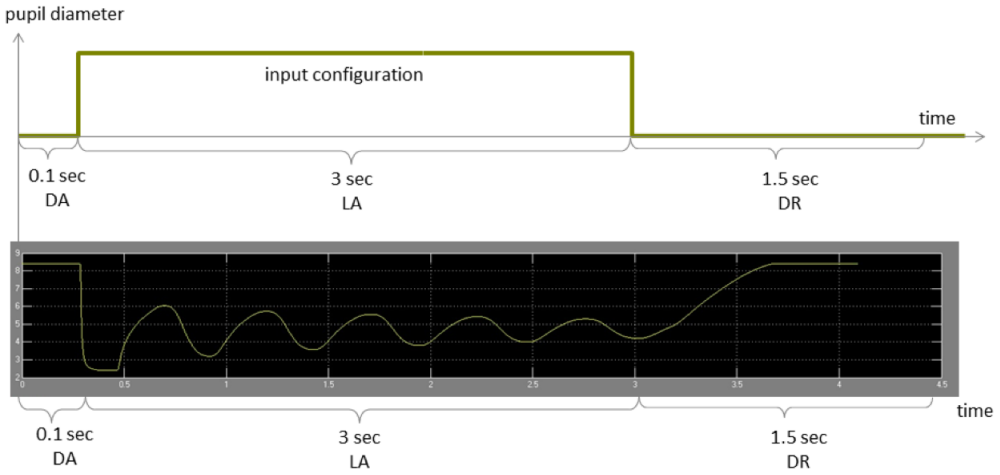

Figure 8.71: Input and Output of the PLR model.

In order to see the response to the chromatic inputs, the output of one color configuration is shown in figure8.72. The first curve represents the acceleration, the next the velocity and the third is the diameter. It can be observed that the model represents well the observed data and that it describes the light adaptation and the oscillations in an accurate way.

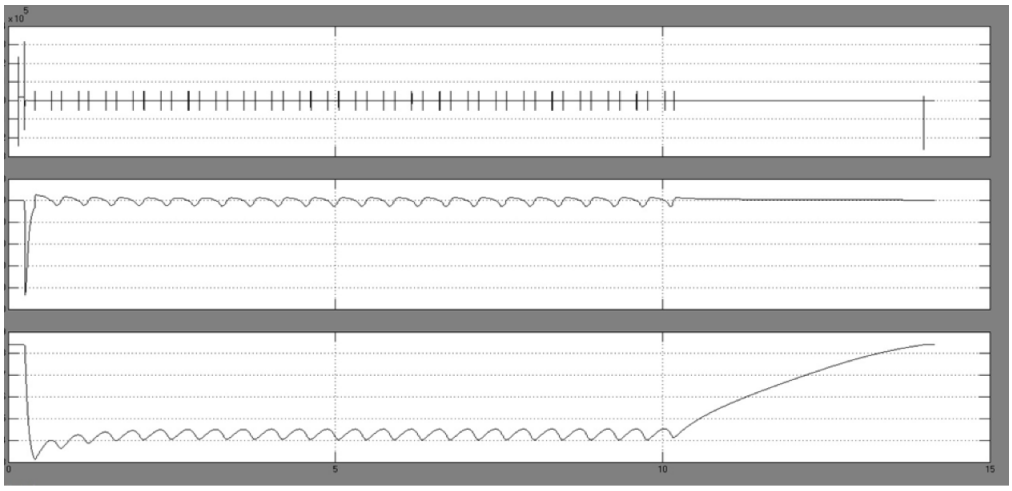

Figure 8.72: Acceleration, Velocity and diameter of the pupil in color configuration 0% Red+100% Green+100% Blue.

In order to confirm the correct functionality of the model related to real data experiments, a protocol test was applied to a voluntary subject, by using the flickermeter developed, a complete description of device in the chapter xxx. The figure 8.74 shows the results of one measurement where the eye, after a dark adaptation of 3 minutes with a luminance less than 0.1 cd/m^2, is illuminated with a fixed RGB light stimulus (120 cd/m^2 of red, 120 cd/m^2 of green and 0 cd/m^2 of blue) for 3 minutes than finally 3 minutes again of dark recovery.

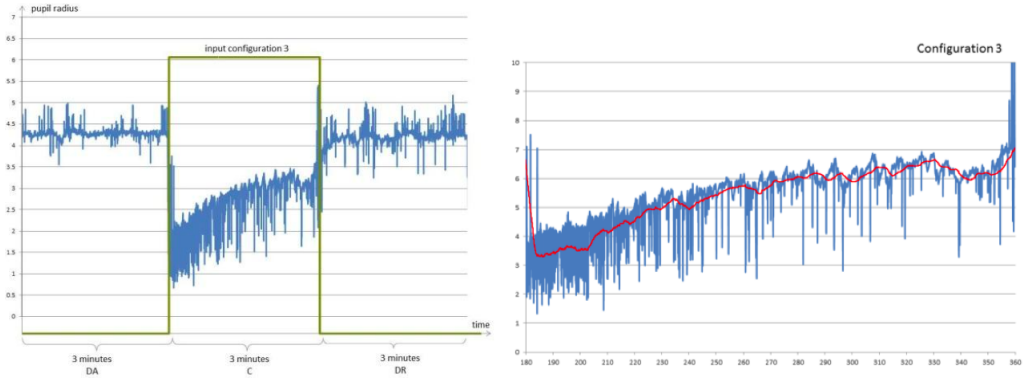

Figure 8.73: Measurement on a 25 years old voluntary male.

The same input parameters (luminance and colors) are applied to the model. The figure 8.74 shows the results of the model. The output is similar to the experimental data but with half of the effective simulation time due to the time step parameter very small. This is a good starting point to improve and obtain a model able to give an answer related to a multicolor light stimulus.

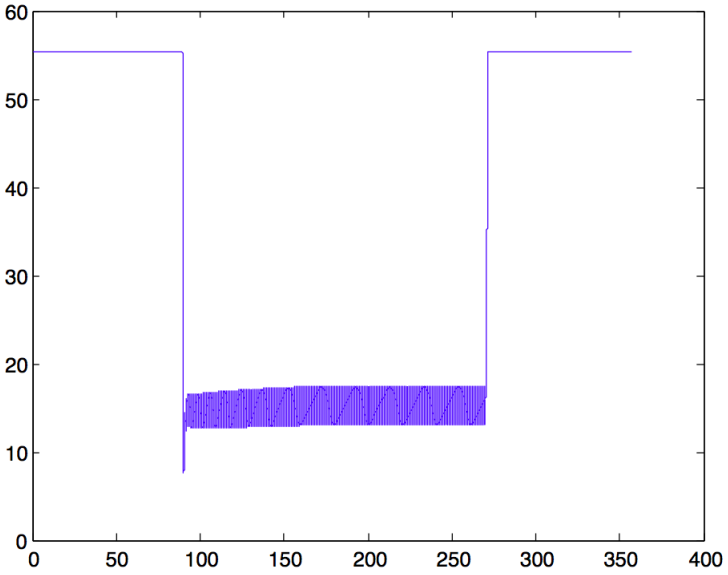

Figure 8.74: Measurement on a 25 years old voluntary male, in x the time in seconds, in y the area of the pupil.

The figure 8.75 shows transition between the 2 states, from dark to light stimulus and from the light stimulus to a dark condition. The model behave similarly to the real data but with a stable and constant signal because the real measurement (see figure 8.74 is affected of noise due to the software calculation artifacts.

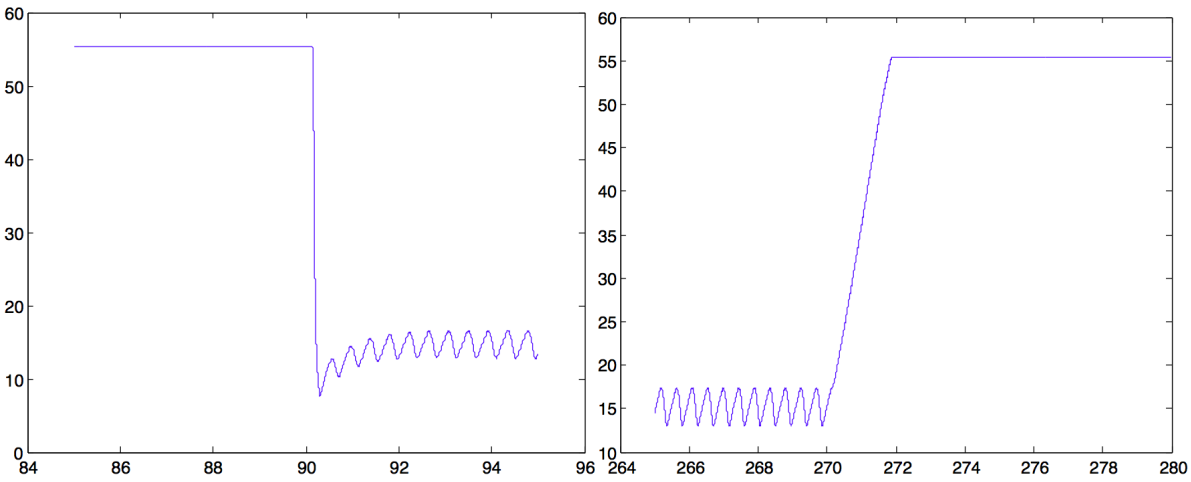

(a) (b)

Figure 8.75: Particular of the transition from the dark and light adaptation A, then from light adaptation and dark recovery B.

8.5 Polychromatic Flickermeter

Numerous researches on chromatic pupillometry are ongoing, no commercially devices are available and no standardized protocols have been defined for clinical usage. The existing approaches have relied on either off-the-shelf proprietary laboratory equipment. Moreover, based on our experience, the integration of the light stimulator and recording camera into a single measuring system might ensure the immediate use, better repeatability and provide a first step toward a clinical use of this technique.

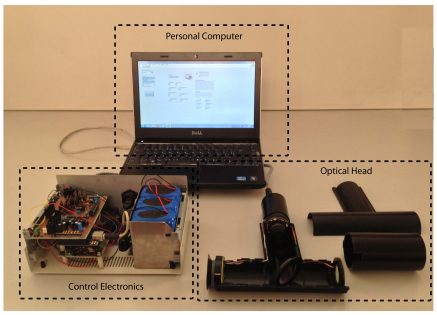

Figure 8.76: Picture of the developed pupillometer.

The developed system, shown in figure 8.76, is able to generate light stimulus with defined color, frequency, modulation and intensity on a fixed target that diffuses the light to the eye while infrared images of the pupil are continuously recorded.

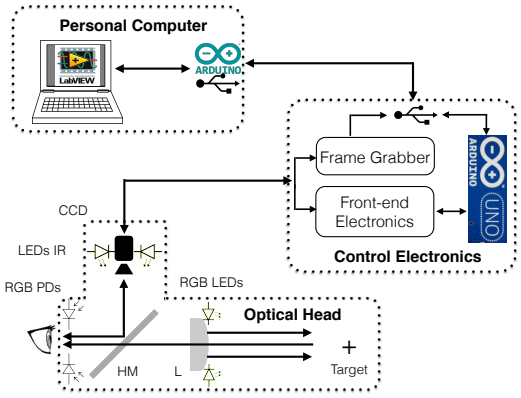

Figure 8.77: Schematic block diagram of the developed system. It consists of three main blocks. The Computer interface through a PC, the electronic to generate the control signals and finally the optical part.

As shown in the block diagram presented in figure 8.77, the system consists of three main parts:

1. *Computer interface*
2. *Control Electronics*
3. *Optical Head*

8.5.1 Optical Head

The optical head is realized by fast prototyping through the PolyJet Technology. This technique is used to print the custom shell to shore up the optical parts conferring robustness, excellent ambient light isolation, and reliability of the measurements. An image target, printed on a paper and fixed inside the optical head, diffuses back the light generated from three RGB LEDs (SFT825N-S, Seoul Semiconductors), as the figure 8.78 shows, then a plano convex lens (LA1031-A, Thorlabs) keeps in focus the target image and guides the flicker stimulus to the eye.

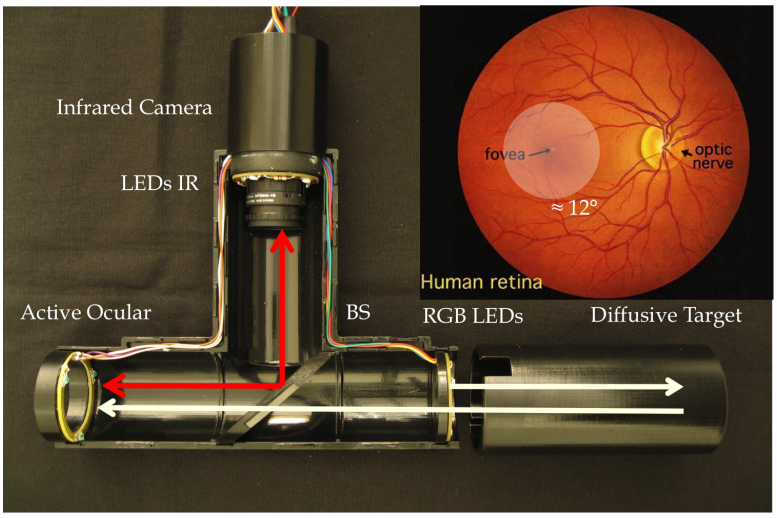

Figure 8.78: The Optical Head of the system and all the optical parts.

The subject under examination looks into an active ocular where the light intensity and color are detected by three RGB photodiodes (S9702, Hamamtsu Photonics); these signals are used as feedback control for the RGB LEDs drivers. A CCD camera (XC-EI50CE, Sony), equipped with a 25mm focal length objective (HF25HA-1B, Fujifilm), records 30 frame/sec of the eye with a resolution of 752 (H) $\times$ 582 (V) pixels. Four near-infrared LEDs (850 nm) (SFH 4253, OSRAM Opto Semiconductors) are fixed on a circular support around the camera objective to illuminate the eye; this not visible illumination does not alter the pupil status. A

45° hot mirror (TS64-470, Edmund Optics) allows the visible light to pass through while radiation in the wavelength range 750 nm ÷ 1150 nm is reflected.

8.5.2 Control Electronics

The control electronics is connected to the optical head through a multipolar cable that carries the signals from the RGB photodiodes, the CCD video output and provides the camera and the near-infrared/RGB LEDs power supply. The control electronics consists of three electronic cards, one frame grabber and a battery pack. The current signals for the RGB LEDs are generated by the board shown in figure 8.79; this board includes two voltage regulators, a low-pass filter, an analog switch and a MOSFET output stage to drive the LEDs.

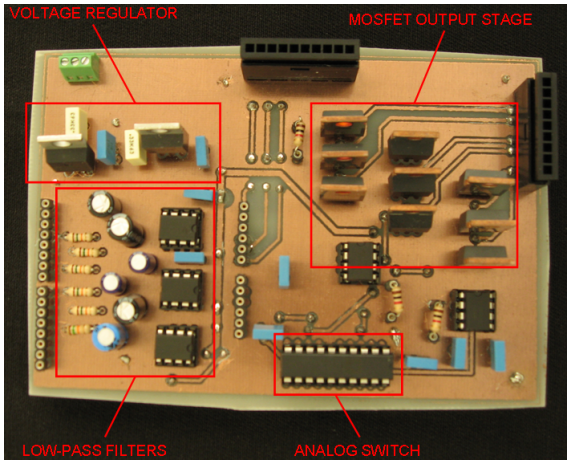

Figure 8.79: The control electronic board is able to provide stable reference voltages that combined with the signals generated by the arduino module are used to polarized the RGB LEDs at constant current.

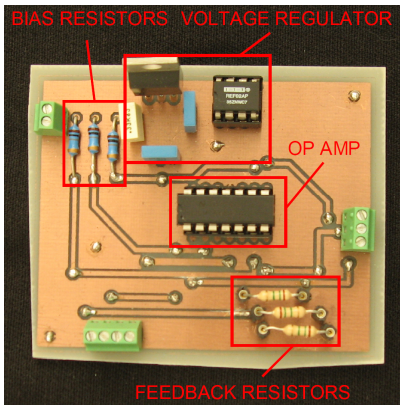

Figure 8.80: The electronic board used to convert and amplify the RGB photodiodes.

The second electronic board, figure 8.80, is devoted to the conversion and properly amplification of the RGB photodiodes outputs. The third card generates the digital signal used to control the flicker characteristics. To this purpose a module ARDUINO UNO (figure 8.81) has been implemented in the system. For each RGB color, ARDUINO generates a pulse-width modulation (PWM) signal, then two low-pass filter stages are used to generate the mean value representative the high or low level voltage; these two levels allow the user to set the modulation depth.

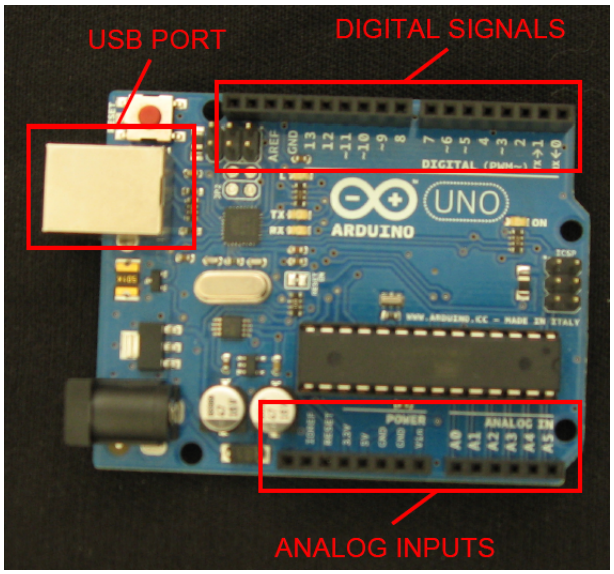

Figure 8.81: The ARDUINO module used to control the timing of the system and to communicate with the personal computer.

The communication between ARDUINO and the PC is via 8 bit words through a serial port on the physical USB channel. A frame grabber (2250, Sensoray) processes the video signal generated by the CCD. A 21 V battery pack (3 $\times$ 7.2 V for 10 Ah each) provides the energy to the whole system except for the frame grabber that is powered via the USB port.

8.5.3 Computer Interface

A LabView graphic user interface was developed to control the system whereas a second software, in Matlab, has been implemented for the video processing. The system control software controls all the RGB LEDs parameters via PC. The flicker frequency, intensity, depths of the modulation and color are sent to ARDUINO with 1 byte word. A single 8 bit word is used also to read the RGB photodiodes signals converted and amplified; this information provides the intensity of the LEDs light emitted for each of the different colors approximately on the same plane of the examined eye. The frequency commutation of the flicker stimulus is generated by

the analog switch square signals that control the high and low levels. The main front panel of the software is showed in figure 8.82.

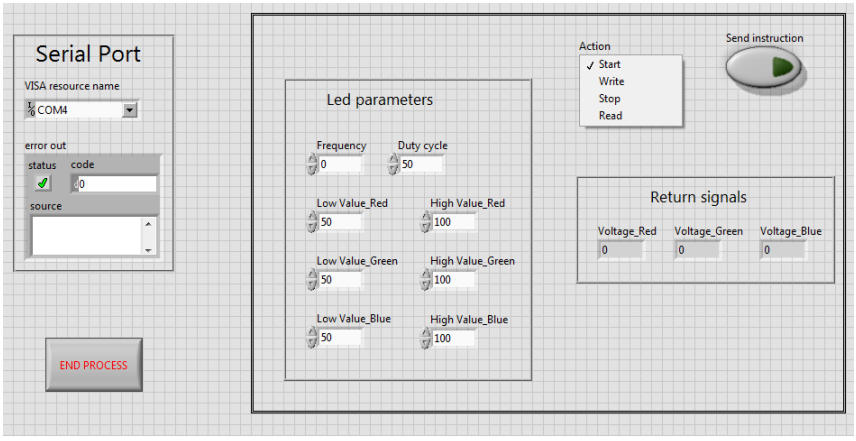

Figure 8.82: The developed LabView front panel. The user enters all the parameters to generate the desired flicker stimulus by regulating the frequency, duty cycle and the intensity color.

Once the program is launched, a second ARDUINO control software configures the communication serial port and waits to perform one of 4 instructions shown in figure 8.83. The instruction START turns on all the LEDs and indicates that the system is ready whereas STOP turns off all the LEDs and any operation until a new START command is received; the WRITE instruction allows us to manage all the flicker parameters as frequency, duty cycle and the 6 levels for the three intensity colors.

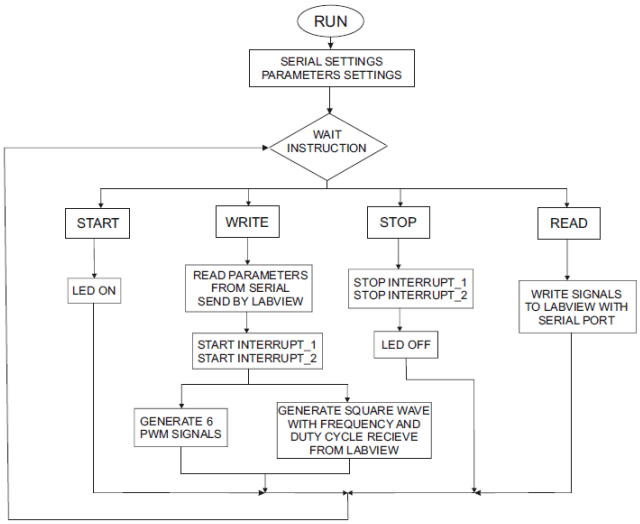

Figure 8.83: Block diagram of LabView front panel. It shows the basic instruction executed by the firmware on ARDUINO.

Through these commands, the user can control the whole system, and is facilitated in the execution of the analysis protocols. From the previous version of the software [12], the image processing algorithm has been modified radically. The new image processing software, under Matlab environment, is a modified version of the Starburst Algorithm eye tracking software [79]. The algorithm computes the pupil area by calculating the best elliptical fitting.

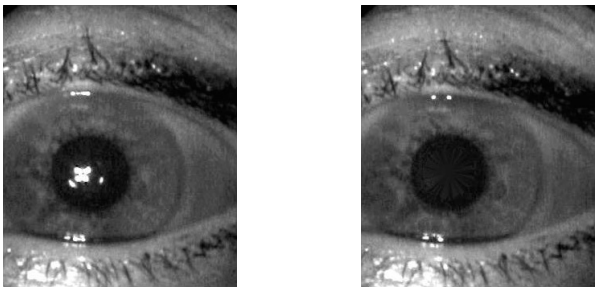

(a) (b)

Figure 8.84: Two explicative frame of the image processing software: a) the original frame. b) The same frame with the corneal reflection removed.

For each frame, after locating and removing corneal reflections (figure 8.84 *a* and *b*), the software detects the pupil edge point located using an iterative feature-based technique: the Random Sample Consensus (RANSAC) paradigm [80]. An ellipse is fitted to a subset of detected edge. The block diagram of the analysis procedure is shown in figure 8.86.

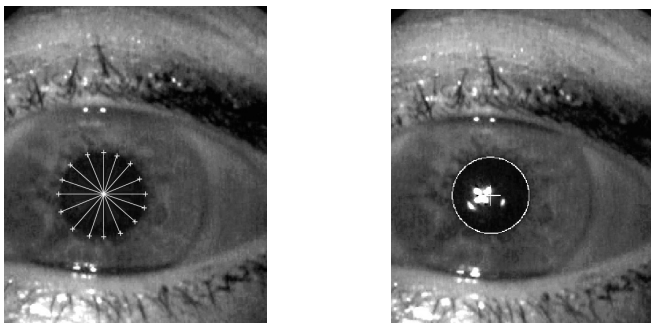

(a) (b)

Figure 8.85: Two frame of the image processing software, fitting and calculation of the pupil parameters. a) the pupil edge candidates (crosses) are detected along rays extending from about the center (user selected) of the pupil. b) Best-fitting ellipse using model-based optimization.

The threshold and the center of the pupil is selected manually on the first frame loaded, for the other frames an adaptive threshold technique is applied. To reduce the noise a 5×5 Gaussian filter with a standard deviation of 2 pixels is applied

to the selected frame. The software follows the rays extending from the starting point (center) figure 8.85 *a*, calculates the intensity derivative at each point then, if major of the threshold, places a feature point. Afterward, for each feature point, the derivative intensity along rays is calculated returning towards to the start point: if the derivative is major than threshold a new feature point is placed. Once a set of candidate feature points are detected, the RANSAC paradigm is used for the model fitting. To increase the fit accuracy a model-based optimization (Nelder-Mead Simplex) is used, figure 8.85 *b* shows an example of the fitting result. Finally from the model, the diameter of the pupil is calculated based on the ellipse parameters, the major axis is considered. This process is repeated frame by frame, thus allowing to determine the average diameter associated with the pupil.

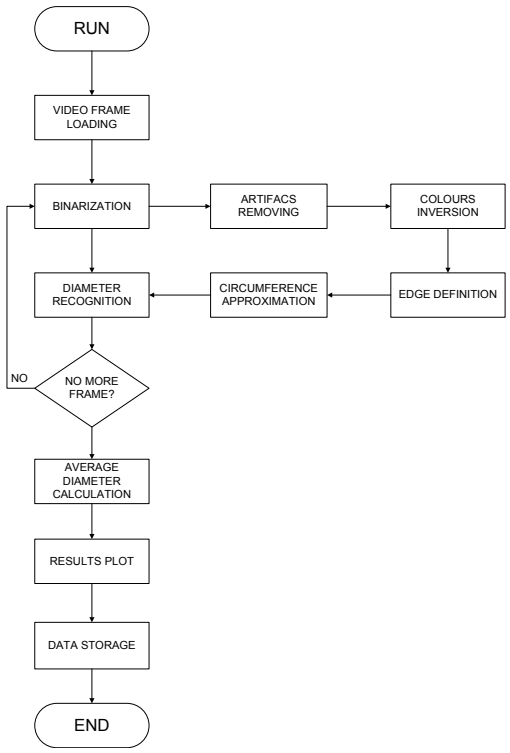

Figure 8.86: Block diagram of the imaging processing software.

8.5.4 System Characterization

The whole system has been characterized in terms of:

- *spectra of the RGB stimuli*
- *luminance for each RGB channel as a function of the digital code set in the LabView virtual instrument*

- *correctness of the generated flicker waveform sequence*

All these measurements have been performed at the same plane of the examined eye. Three different calibrated instruments have been used to perform the characterization:

- *spectra have been acquired using a photonic multichannel analyzer (PMA-11, Hamamatsu)*
- *luminance was measured by a portable photometer (HD 9221, Delta Ohm) equipped with a proper optical head (HD 9221/S3, Delta Ohm)*
- *waveforms of the flicker stimulus was acquired using a fast silicon photodiode module (FEMTO-OE-200-IO-Fast, FEMTO)*

All the characterization measurements have been performed after a suitable warm-up time of the instrument (about 20 mins) in the same dark room where the experiments on human beings have been performed.
First activities have been aimed at characterizing the developed pupillometer according to the measurement procedure presented. After a proper warm-up time of the instrument, the spectra, the luminances as a function of the digital code set in the LabView software and the waveform of the flicker produced by the RGB LED were acquired. The normalized spectral intensity of each single RGB channel as it impinges on the pupil aperture is shown in the figure 8.87. Peak wavelengths are located at 460 *nm* for the blue channel (bold line), 538 nm for the green channel (dash line) and 645 nm for the red channel (dash-dot line). Moreover, as shown in figure 8.87, the full width at half maximum (FWHM) of the green emission (47 nm) is larger than the FWHM of blue (23 nm) and red (20 nm) emission.

The relation between the variable code (0-128) used to set the luminance of each RGB channel (blue bold line, green *diamond* dash line and red or dash-dot line) and the corresponding luminance at the same plane of the examined eye is shown in figure 8.88. First part of the range just compensates the off-set and other non-ideality of the current drivers thus till to a value of about 10, no significant luminance irradiate the eye. After which, for code values above this range, the non-linearity observed are mainly due to the LED sources. A proper look-up table in the virtual instrument allows mapping these non-linearities.

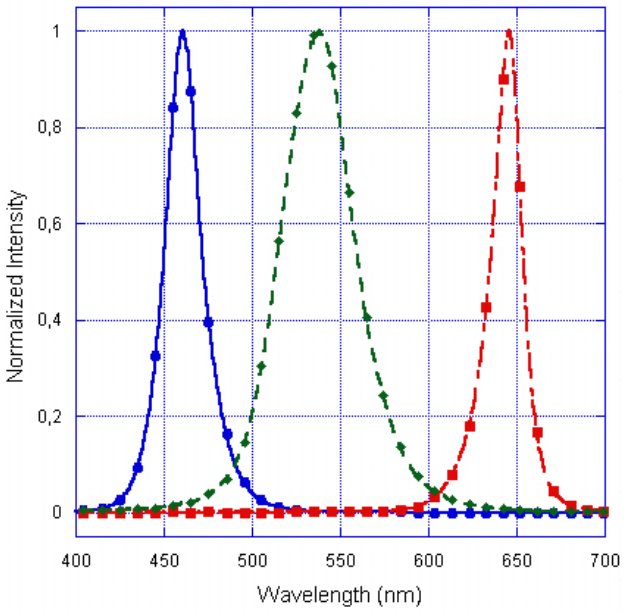

Figure 8.87: Normalized spectral intensity of each single RGB channel as it impinges on the pupil aperture.

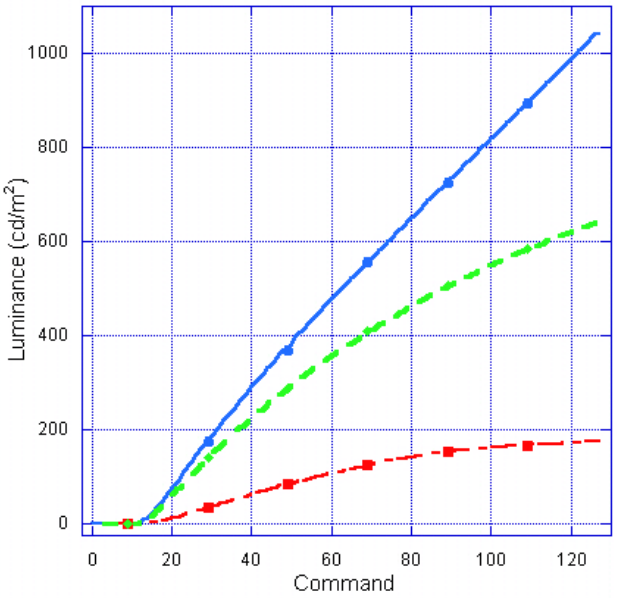

Figure 8.88: Relation between the variable code (0-128) used to set the luminance of each RGB channel and the corresponding luminance at the same plane of the examined eye.

Even if the maximum luminance achievable from the red channel is lower than the luminance generated by the other two channels, this value is sufficient to guarantee a photopic stimulus. The maximum luminance achievable from the red channel was taken as a reference to determine the equiluminance condition during the mea-

surement protocol. Of course, even if the other channels would allow obtaining more intense stimuli, the maximum luminance of the red channel represents the instrument limit for equiluminance experiments. Dynamic behavior of the stimulus has been verified by using a fast response photodiode module. As an example, the module output recorded when a green flicker signal was generated for 12 seconds is shown in figure 8.89. During this period the frequency of the stimulus (2, 8, 10, 14 and 20 Hz) was changed every 2 seconds. The first and the last 2 seconds simulate to the adaptation and the rest phases of the protocol. Note as the luminance, in these rest periods, is the 50% of the flicker peak intensity whereas the duty-cycle of the waveform is the 50%. Hence equiluminance condition is maintained during all the 14 seconds.

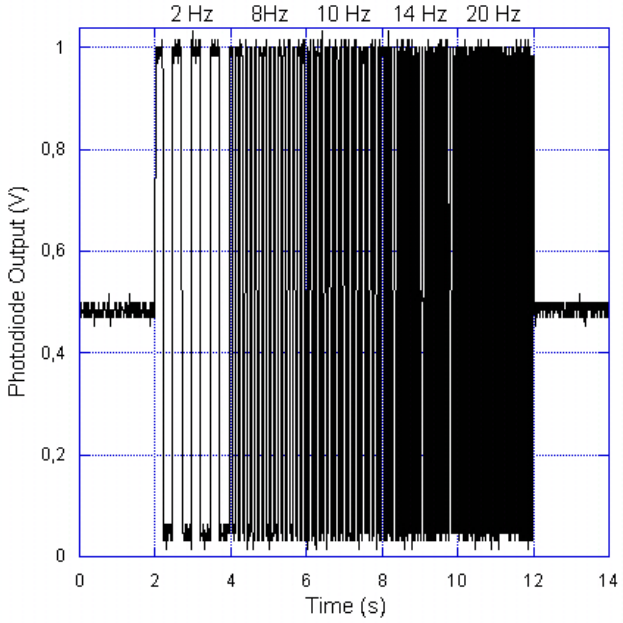

Figure 8.89: Fast photodiode module output recorded when a green flicker signal was generated for 12 seconds.

8.6 Flickermeter measurements

8.6.1 Annoyance

Preliminary experimental activity (Part 1)

Three adult voluntaries with not known visual abnormalities were selected for this preliminary study. The age of the subjects varied from 23 to 28 years. Each subject has voluntarily agreed to the study and has been adequately informed of the protocol used for the measurements. The preliminary protocol adopted for the experimental

activity is shown in figure 8.91, and consists in: a first epoch where the volunteers were asked to seat in a dark condition environment for 30 minutes to maximize the sensibility of the eye; a second period where the LEDs light illuminates the eye without flickering for 90 seconds: the last 30 seconds are recorded by the camera to compute the reference diameter R_f used to normalize the subsequent measurements. In the third epoch, four flicker stimuli having frequencies 1-5-10-20 Hz, respectively, are supplied in sequence for 90 s each.

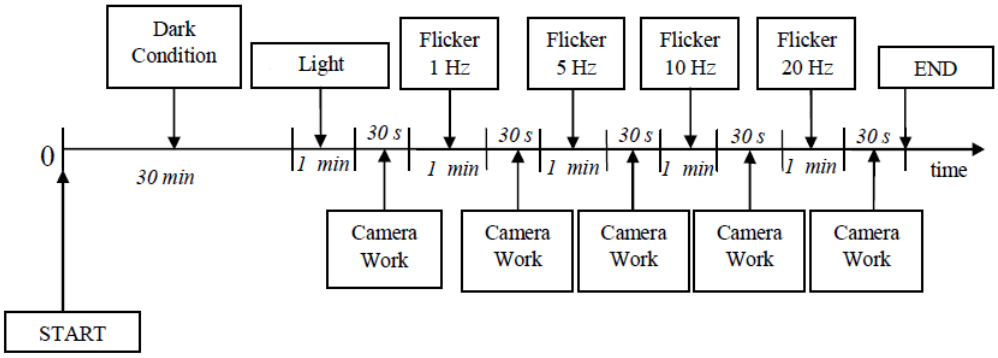

Figure 8.90: Time sequence of the preliminary protocol. After 30 minutes of dark adaptation, the eye of the subject under test is illuminated with 1 minute and 30 seconds of constant light to record a reference pupil dimeter. Afterward for each flicker frequency, the eye is stimulated for 1 minute and 30 seconds. For the image analysis only the last 30 seconds of each epoch is computed.

The first 60 are used to allow the adaptation of the pupil, thereafter the pupil images are recorded for the remaining 30 s. During all the experiment the average light luminance at the eye plane was maintained constant. As shown in figure 8.91, in this preliminary test the eye was stimulated by a white light whose spectrum is the combination of the RED ($623 \pm 3nm$), GREEN ($527 \pm 7mn$) and BLUE ($460 \pm 5nm$) colors.

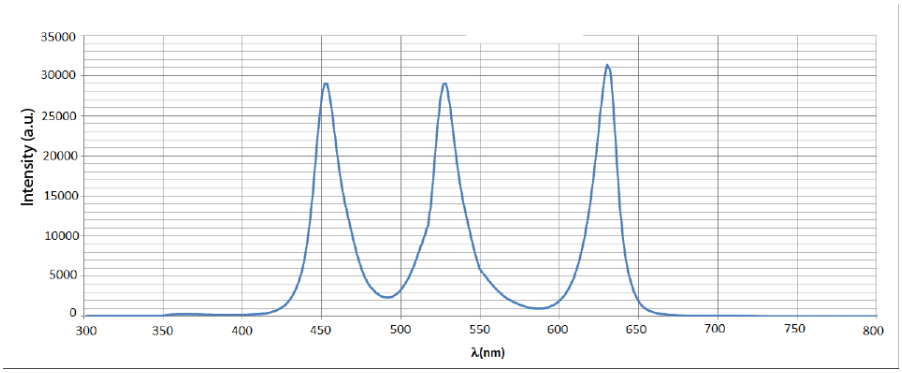

Figure 8.91: Spectrum of the white stimulus.

Since the average light luminance during the experiment was maintained constant, the pupil should remain unperturbed. Nevertheless, as reported in our previous papers [12, 13, 17, 81], flicker of the light induced a pupil contraction.

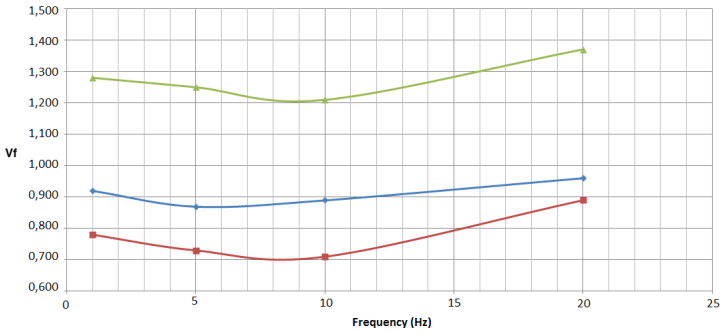

Figure 8.92: The average normalized pupil diameter as a function of the flicker frequency as recorded for the three subjects.

The pupil responses to flicker stimuli for the three subjects are shown in figure 8.92. The average normalized pupil diameter V_f is calculated as the ratio between the pupil diameter recorded at the frequency f and the reference pupil diameter R_f acquired during the continuous illumination. The inter-subjects average pupil diameter (RPD) shown in figure 8.93 is calculated as:

$$RPD = \frac{1}{N} \sum_{k=1}^{N} V_f, k \tag{8.7}$$

where N=3 is the number of subjects. Averaging the pupil diameters recorded from the three subjects, the maximum pupil contraction at the flicker frequency of about 8 Hz is emphasized. This result are consistent with our previous study performed with green stimuli [13].

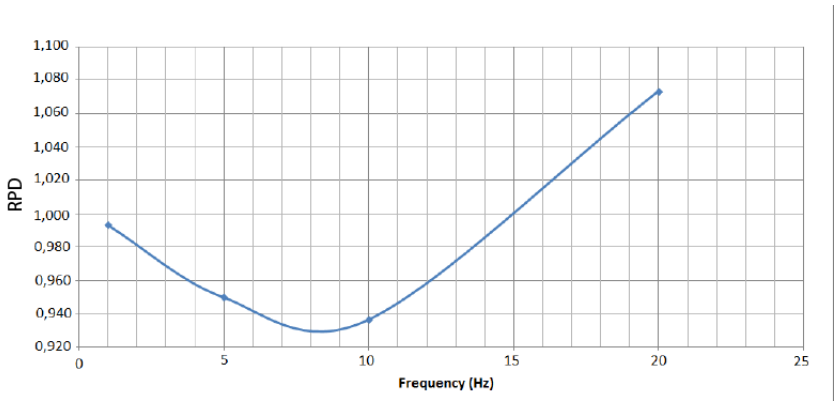

Figure 8.93: Average pupil diameter as a function of the flicker frequency. The maximum pupil contraction was recorded at the flicker frequency of about 8 Hz.

Preliminary experimental activity (Part 2)

The pupillary responses to equiluminant RGB flickering stimuli in the range 3-20 Hz were acquired. The effect of each single RGB chromatic component was evaluated separately in three successive epochs i.e. red, green and blue epoch. To maintain photopic vision regime, during each epoch the average luminance of the stimulus was maintained constant to a value of 86 cd/m2. The visual angle subtended by the stimulus was about 12° and its homogeneity better than 5%. To minimize accommodation artifacts, a fixation target was presented to the right eye (examined eye) of the subject while the left is open and covered by the left hand. To evaluate variability, both within the same subject (intra- subject variability) and among subjects (inter-subject variability), two experiments were performed. The intra-subject variability was investigated in a single subject study. The selected voluntary was 49 years old and had normal vision. A set of ten tests was performed in ten consecutive days at about the same time of day. The subject has voluntarily agreed to the study and has been adequately informed of the protocol used for the measurements. Inter-subject data were collected from fifteen subjects aged between 24 to 42 years old. The voluntaries consisted of 11 males and 4 females. All subjects had normal or corrected-to normal vision. Each subject has voluntarily agreed to the study and has been adequately informed of the protocol used for the measurements. For both the experiments measurement protocol was the same. The volunteer was asked to seat in a quite and dark condition environment for 5 minutes to maximize the sensibility of the eye. After this rest period the first measurement epoch started with the green stimulus. Steady illumination was presented to the eye for 4 minutes and during the last 30 seconds the pupil image was recorded. This information was used to calculate the average pupil area at the rest condition. Afterward, six flicker stimuli having frequencies 3-5-8-10-15-20 Hz, respectively, were supplied in sequence for 90 s each.

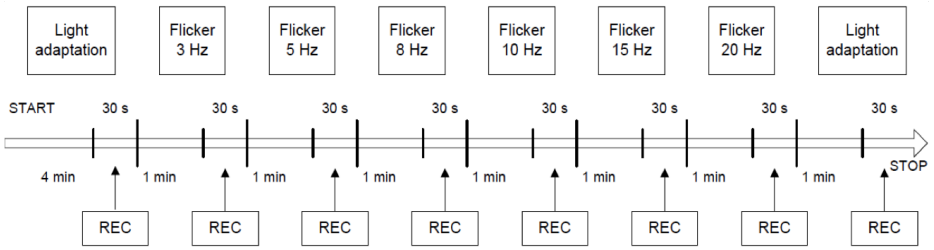

Figure 8.94: Annoyance protocol measurement for intra and inter-subject test.

The first 60 are used to allow the adaptation of the pupil, thereafter the pupil images were recorded only for the remaining 30 s. Finally, a second rest period of 90 s at steady illumination was presented to the eye and during the last 30 seconds

the pupil image was recorded 8.94. Also this information was used to calculate the average pupil area at the rest condition. The same measurement scheme was used for the blue and red epochs. Between one epoch and the other, the voluntary was asked to relax by closing his eyes. For each test, the normalized pupil area $PA(f)$ was calculated as the ratio between the time averaged pupil area recorded, $PA(t)$, when the flicker frequency was f and the reference time averaged pupil area acquired during initial ($PA_{base,i}$) and final rest periods ($PA_{base,r}$) , i.e. steady illumination, see the formula 8.8

$$PA(f) = \frac{PA(t)}{\frac{PA_{base,i}+PA_{base,r}}{2}} \tag{8.8}$$

Hence, for each flicker frequency, the intra-subject and inter-subject average $PA(f)$ and type A measurement uncertainty were evaluated [82]. As said in the previous Section, the measurement procedure and protocol was applied for performing intra-subject as well as inter-subject tests. Figure 8.95 shows, for the former case and for each color, the plots of the mean values of the $PA(f)$ vs. flicker frequency and the associated standard deviations of the mean. The last quantities are used to express the uncertainty (type A evaluation, [82]) on the estimate of the mean values. One can observe that such uncertainties are rather high with respect to the mean values (some percent) but it must be kept in mind that the *measurand* is the human being and hence differences between subjects or between the same subject in different days are obvious and natural. Figure 8.96 shows the same quantities of 8.95 for the inter-subject tests. From 8.95, first of all it can be concluded that the repeatability of the measurements on the same subject is pretty good, of course by considering, as said above, the particularity of the measurand. As a matter of fact, the relative values of the standard deviation of the mean range approximately from 3% to/7%, without significant variations from one color to another. Such values are comparable with the differences between the mean values of the normalized pupil area but not so high to significantly modify the shapes of the frequency responses shown in 8.95.

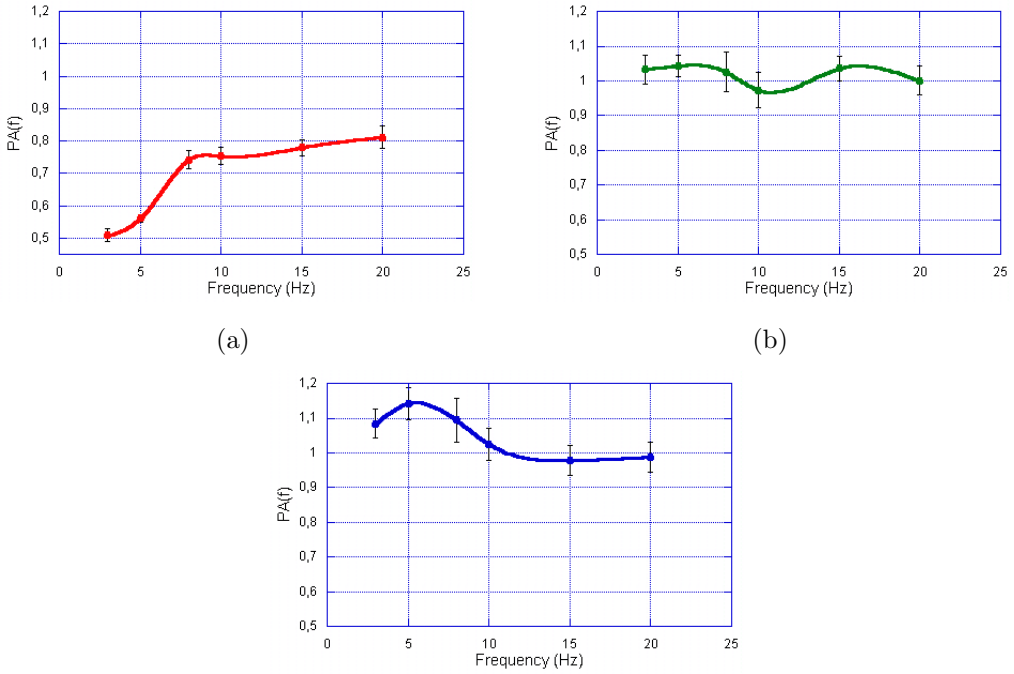

Figure 8.95: Intra-subject tests: plots of mean values of the normalized pupil area and associated standard deviations of the mean vs. flicker frequency for different colors: a) red, b) green, c) blue.

Moreover, for the considered subject, it can be observed that pupil response is remarkably dependent on the color of the flicker stimulus: when the color is red (figure 8.95 a), the pupil area increases vs. frequency; when the color is green (figure 8.95 b) minimum is exhibited at 10 Hz whereas when the color is the blue one (figure 8.95 c), a maximum occurs at 5 Hz. Such rough observations are confirmed when the plots in figure 8.96, which refers to tests carried out on 15 people, are considered. More in details, the above trends are more evident: the response to red (figure 8.96 a) is pretty monotone whereas the minimum for the green (figure 8.96 b) and the maximum for the blue (figure 8.96 c) are well marked. It can be noted that the shape of the response to green flicker is quite similar to the one obtained by the authors in [11] in different measurement conditions. Also in this case, the relative values of the standard deviations of the mean ($2\% \div 6\%$) are very good.

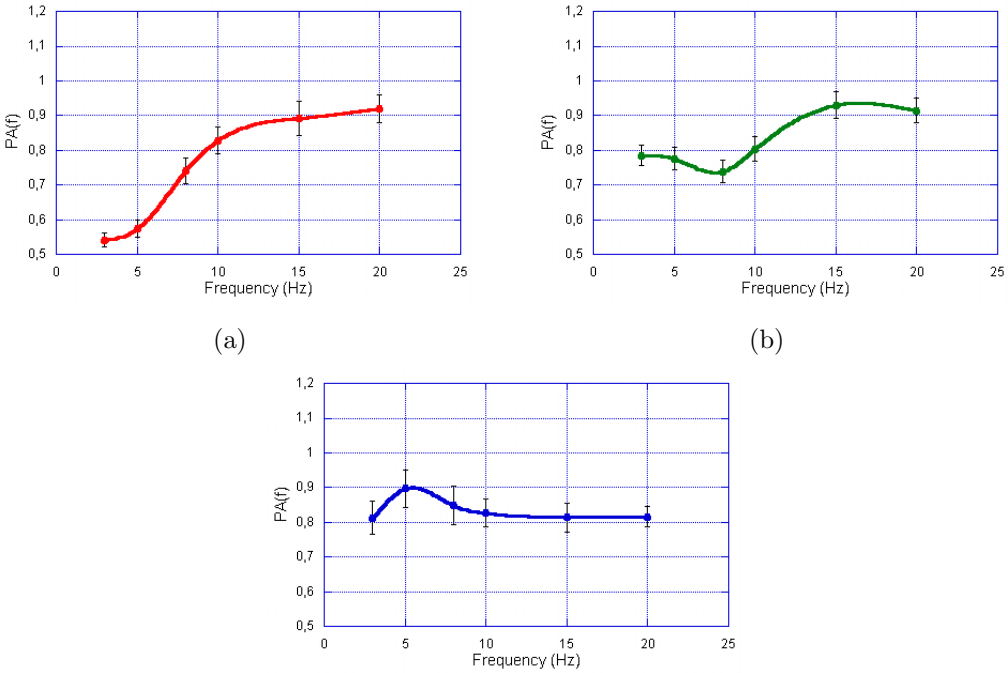

Figure 8.96: Inter-subject tests: plots of mean values of the normalized pupil area and associated standard deviations of the mean vs. flicker frequency for different colors: a) red, b) green, c) blue.

Melanopsin

Preliminary functional tests of the device were performed on a voluntary (male, age: 48 years) with 20/20 corrected vision and no known visual abnormalities. The study consisted of two experiments: experiment 1 measured the maximum pupil contraction versus stimulus intensity whereas experiment 2 was devoted to determine the time course of pupil response in relation to high intensity pulse stimulus.
Before each experiment, maximum pupil area (PA_{max}) was measured exposing the voluntary to darkness for at least 6 min to allow cone photoreceptors to dark adapt according to the classical adaptation curves obtained by Hecht et al. [83]. Minimum pupil area (PA_{min}) was determined exposing the subject to a bright white light stimulus (about 275 lux) for about 1 min since cones are known to show rapid light-adaptation [71]. The relative pupil area contraction (PAC%) was expressed versus maximum contraction ($PA_{max} - PA_{min}$) as follows:

$$PAC\% = \frac{PAC_{max} - PA(t)}{PA_{max} - PA_{min}} \times 100 \tag{8.9}$$

In our setting the measurements were performed under scotopic conditions. To minimize accommodation artifacts, a fixation image at the distance of 3 m was

presented to the right eye of the subject while the left was stimulated by the pupillometer. Both the experiments exploit photopically matched red and blue stimuli in the dark. Pupil diameter recording was started 30 seconds before the first light stimulus. The spectra of the stimuli were measured by fixing the optical head of an optical spectrum analyzer (PMA-11, Hamamatsu) on the soft eyepiece of the optical head whereas the homogeneity of the light distribution in the visual field was quantified using a calibrated photometer (Delta Ohm, HD9221). In experiment 1, the dark-adapted maximum pupil contraction versus stimulus intensity functions for red and blue stimuli were measured over a wide range of intensities from -1 to 1.5. log cd/m^2 in steps of about 0.5-log. The actual intensity step between the pulses was set consistently with the resolution of the of LEDs driver. Nevertheless, the luminance values of the red and blue stimuli are practically photopically matched. Starting from a pulse intensity of -1 log cd/m^2, the intensity of each pulse stimulus was increased by a 0.5-log step respect to the previous light pulse to reach the maximum intensity value of 1.5 log cd/m^2. To ensure the complete baseline recovery after each stimulus offset a repletion rate of 100 mHz was used whereas the light pulse duration was equal to 1 s.

Experiment 2 was devoted to determine the sustained pupil contraction after stimulus offset in photopic vision regime. Therefore, after 6-minute dark adaptation, red and blue pulse stimuli at high-intensity (1.66 log cd/m^2) were alternated for a total of eight cycles. To avoid transient effects, only the last four cycles have been recorded. According to Park et al. [84], to maximize the difference between the sustained pupil contraction after red and blue light offset, a 1-second pulse stimulus at the repetition rate of 100 mHz was used as for experiment 1.

The peaks wavelengths for the blue and red radiations are 452 nm and 631 nm, respectively. The visual angle subtended by the stimulus is about 5° and its homogeneity better than 5%.

Experiment 1: After 6-minute dark adaptation, the subject pupil size was $7.00 \pm 0.12mm$. Figure 8.97 shows the relative pupil area contraction and stimulus waveforms as acquired during the experiments. Figures 8.97 a and 8.97 b show the responses for to blue and red stimuli, respectively. The maximum PAC% to blue stimuli shows a monotonic trend for low-intensity light and a saturation at high intensities, whereas the maximum PAC% to red stimuli is characterized by moderated sensitivity to stimuli with intensity lower than -0.5 $logcd/m^2$.

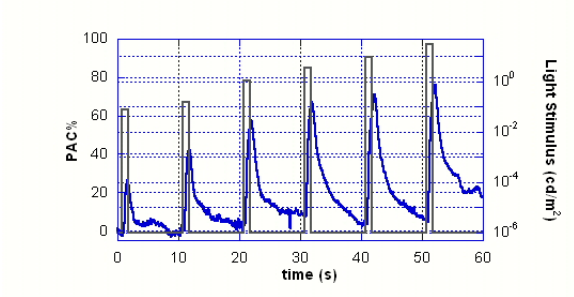

(a)

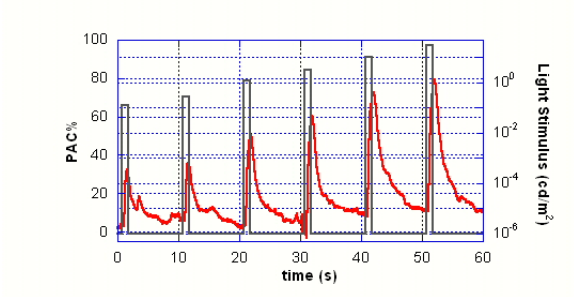

(b)

Figure 8.97: Relative pupil area contraction (red and blue traces) and stimulus (black trace) waveforms as acquired during experiment 1. Responses to blue a) and red b) stimuli.

Figures 8.98 shows the comparisons of maximum PAC% to the photopically matched blue and red stimuli. The blue stimuli induced larger PAC%, but at the highest intensities, the maximum pupil contractions for red and blue stimuli are similar. The maximum PAC% versus stimulus intensity function change almost linearly on the semi-log plot in the photopic vision region, i.e. approximately from 0 to 1.5 log cd/m^2. The thick blue and red lines are the linear regression lines for the blue and red data between -1 to -0.5 $logcd/m^2$ and between 0 to 1.5 $logcd/m^2$. The regression line slopes in the mesopic region are $40.87\%/(logcd/m^2)$ and $10.13\%/(logcd/m^2)$ for the blue and red stimuli, respectively. In the photopic region these values are $6.98\%/(logcd/m^2)$ and $15.40\%/(logcd/m^2)$ for the blue and red stimuli, respectively.

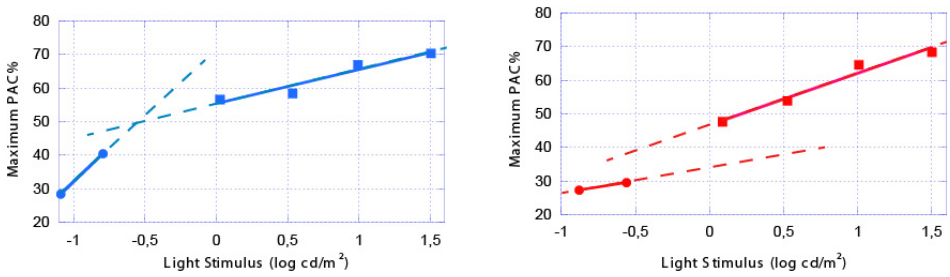

(a) (b)

Figure 8.98: Maximum relative pupil area contraction to photopically matched blue a) and red b) stimuli. Thick blue and red lines represent the linear regression lines for the blue and red data between -1 to -0.5 log cd/m^2 (mesopic vision region) and between 0 to 1.5 $logcd/m^2$ (photopic vision region). The dashed lines are given as guides to the eye out of these ranges.

Experiment 2: After 6 minutes of light adaptation, the subject resting pupil diameter was $6.86 \pm 0.14mm$. Waveforms of the pupillary responses obtained in experiment 2 are presented in figure 8.99. According to experiment 1, the maximum pupil contractions for red and blue stimuli are similar. The responses indicated a short constriction time followed by a sustained pupillary constriction after stimulus offset. The onset time of the response was found by fitting the pupillary responses by a single-exponential function.

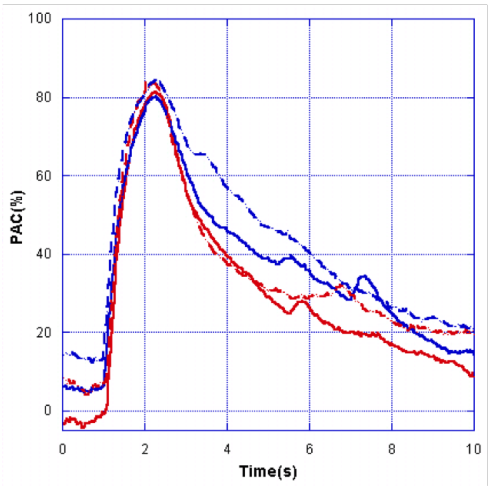

Figure 8.99: Relative pupil area contractions to red (continuous red line) and blue (dashed blue line) stimuli recorded during experiment 2.

The best-fitting allows us to determine the rise time constants shown in figure 8.100 a) for the four stimulus pulses. Same approach was used to characterize the re-dilatation kinetics. The recovery time constants, i.e. sustained pupillary constriction time constants, of the best-fitting exponential functions are shown in figure 8.100 b).

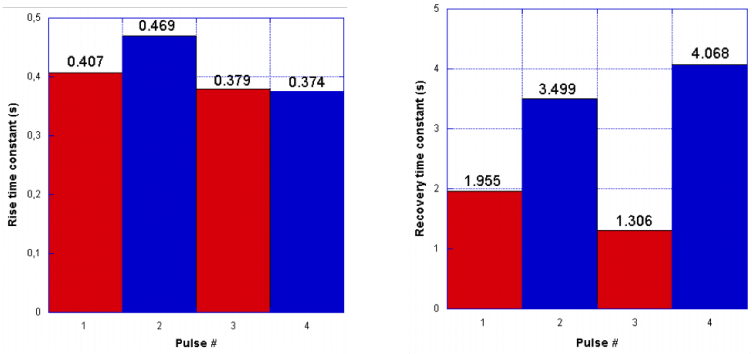

(a) (b)

Figure 8.100: Contraction and redilatation kinetics derived from the time-constant of the best-fitting exponential functions to PAC%. Time-constant for the contraction a) and redilatation b) of the relative pupil area for blue (pulses 1 and 3) and red (pulses 2 and 4) stimuli.

Chapter 9

Conclusion and Discussion

Indoorillumination has undergone big changes in recent years. LED-based products have replaced conventional light sources in several environments providing both superior efficiency and performance with capabilities such as tunable lighting.Indoor ambient lighting also has an important effect on well-being, in particular when the exposure is prolonged and/or susceptible populations are exposed, e.g. offices, classrooms, hospitals and daycare centers. This phenomenon has emerged thanks to the development high brightness solid-state sources. The GaN LED technology is the heart of all the commercial optical sources, thanks to the lumens / Watt intensity emitted by this sources resulting the perfect candidate to be the substitute of the obsolete sources. The technology is not yet fully mature, as has been reported the droop efficiency is one of the unsolved issue of the device.
Driven by the cost-per-lumen and efficacy improvements dictated by the solid-state-lighting roadmap, many efforts are being made both in industry and academia to improve the physical understanding of the efficiency droop phenomenon in InGaN/GaN blue LEDs. Several physical mechanisms have been held responsible for droop, relying on experimental and/or theoretical investigations, but no conclusive assessment of droop physical origin(s) has been attained. In fact, the knowledge of several key parameters that can impact droop is affected by significant uncertainties, including Auger coefficients, band offsets and polarization charges at AlGaN/GaN and InGaN/GaN interfaces, QW scattering rates, indium content and/or width fluctuations in the InGaN QWs. Some of these parameters are sensitive functions of material, growth, and/or processing conditions. All this may explain the wide spectrum of results and interpretations as well as the difficulties in comparing data from different technologies. Extensive efforts are also being devoted to attain a solution able to suppress droop. Many proposed remedies have actually been effective at a laboratory/research level, and some of them have already found their way to industrial-level implementation. The possibility that droop is induced by a combina-

tion of mechanisms may explain the difficulties encountered so far in its elimination, as well as the fact that its mitigation has been demonstrated by a variety of (sometimes conflicting) methods.

Ambient lighting should be designed taking into account the critical aspects associated with flicker. Several studies report the impact of lighting flicker on well-being, performance and physiological arousal [7, 8]. Obviously, this requires a precise understanding of physiological phenomena induced by flicker and a method of quantization of these effects. The experimental observations reported demonstrate as the flicker induces pupil contractions not associated to changes in luminance. The results show as the RGB components induce different effects on pupillary response. Mainly these differences are due to the actions undertaken by the photoreceptors [80, 82]. Note the singular behavior of the pupil when stimulated by blue radiation flicker: this stimulus induces an enlargement of the pupil when the frequency of flicker is set to about 5 Hz. For the subject analyzed in the test of repeatability, this condition is described by a pupillary area greater than the one observed in resting conditions. The pupillary aperture control system is complex and non-linear, therefore the correlation between frequency and time responses is not trivial and requires an appropriate model that we are developing. Concerning the measurement uncertainty, the results demonstrate how the variability observed on the same subject on different days is similar to the one observed in a population of 15 subjects. Hence, the variable that we chose to quantify the annoyance, i.e. the pupil area, could not require normalization between subjects. If a wider statistical confirms this statement, the use of the pupil area to quantify the flicker annoyance would be much simpler. We believe that this work can contribute to the understanding of the flicker annoyance issue and represents a first attempt at identification a measurable quantity describing it: the pupillary area. Hopefully, these results may be of interest to IES, CIE, IEEE groups (http://grouper.ieee.org/groups/1789) and, the EPA ENERGY STAR [http://www.energystar.gov] program that are working on recommended practices for evaluating flicker risks.

The depth study of the pupillary reflex mechanism is very important. The pupillary light response to a well-defined light stimuli is a non invasive technique diagnosis for estimating health of the human visual system and also human body. As reported in this work, there are several diseases that potentially can be diagnosed. Well-defined test protocols on volunteers is important for the diagnosis but is equally important to develop an analytical model of the pupillary reflex able to simulate the behavior of the pupil light reflex. In this regard, iwith this work the bases of a model have been reported. By the new Simulink model has been developed which is capable to simulate the polychromatic Pupillary Light Reflex dynamics with the help of an innovative experimental approach. The spectral sensitivity of the photorecep-

tors placed on the retina, the modulation inputs from both parasympathetic and sympathetic systems and the iris muscle mechanical properties are the key element. The experimental data have shown accordance between the real and the simulated response of the pupil to the light stimulus. The dynamical part, the velocities are well modeled. The light adaptation, which has been observed in the experimental data during the light stimulus, with a progressive and slow increase of the diameter during the stimulus is well described, in order to achieve a more accurate answer through the model a test campaign should be considered on more subjects and a fitting with new parameters could improve the system response.

The pupillometer developed and then described in this work behave according to design criteria. The portability, ease of use and flexibility characterize this instrument and demonstrate its full functionality. The tests performed on the melanopsin report a clear dependence on the nature of stimulus that acts on the eye. It has been reported that a blue stimulus generate different dynamics of the pupillary reflex, due to the production of melanopsin by the ipRGC. This photopigment has a peak of optical responsivity very close to the typical GaN LED peak emission. Furthermore melanopsin inhibits the production of melatonin which is closely linked to the regulation of circadian rhythms. It 'important to evaluate and observe what has been observed by the tests reported.

Over the lower range of intensities, the PAC% to blue stimuli are mainly rod mediated. Although we cannot rule out a cone contribution but the rods probably dominate in the low-range of intensity. However, being the stimuli in the mesopic region, the difference in sensitivity observed between blue and the red stimuli do not equal the expected huge difference accounted by the scotopic vision regime (after CIE 1951). In fact, the eye sensitivity function of the scotopic vision regime $V'(\lambda)$ is equal to 0.46 at 452 nm (blue) and 0.003 at 631 nm (red) [85]. Over the higher range of intensities, the PAC% to the blue stimuli are mainly cone mediated. However, in this vision regime, the rod contribution can not be neglected. The observed higher sensitivity to red stimuli is consistent with the values of the eye sensitivity function of the photopic vision regime (CIE 1978) $V(\lambda)$ that is equal to 0.048 at 452 nm (blue) and 0.25 at 631 nm (red) [85].

The sustained pupil responses after the offset of blue stimuli are attributed to melanopsin. In contrast to the previous study by Park et al. [84], neither the red nor the blue stimulus caused a significant sustained response. Nevertheless, contraction and re-dilatation time constants related to red stimuli were always shorter than the ones of blue stimuli. However, to observe significant contributions from melanopsin a large area of the retina should be stimulated. In fact, melanopsin was localized to a small subset (1-2%) of retinal ganglion cells (RGCs) [86]. A possible future development of our pupillometer would be focused on the implementation of

a system to easily adjust the visual angle over a wide range.
The pupillary reflex model has to be developed in detail to provide a tool to coupled with the flichermeter. The studies performed with the flickermeter and future developments may be useful to help for the formulation of new normatives compatible with the nature of the latest generation of LED sources. With regard to solid state sources, by the depth study of the parameters that cause the droop efficiency theoretically is possible to deal with solutions that lead LED InGaN/GaN structural modification to control within the theoretical limits of the parameters quantified by statistics methods.

Chapter 10

Publication List

10.0.1 Journal Papers (Accepted)

1. M. Mentek, C. Chiquet, F. Truffer, M. Bernabei, B. Mottet, J.P. Romanet, D. Godin-Ribout, M. Geiser, *Development of a prototype of laser Doppler flowmeter for the measurement of blood flow of retinal vessels and optic nerve head tissue in small animals (rats)*, Investigative Ophthalmology and Visual Science, Vol. 54, 4669, June 2013.

2. M. Geiser, F. Truffer, M. Mentek, M. Bernabei, F. Aptel, C. Chiquet, *Laser doppler fluometrie on small animal*, Acta Ophtalmologica 09/2014, (92s253).

3. M. Mentek, F. Truffer, C. Chiquet, D. Godin-RIbuot, S. Amoos, C. Leouillet, M. Bernabei, M. Geiser, *Compact Laser Doppler Flowmeter (LDF) Fundus Camera for the Assessment of Retinal Blood Perfusion in Small Animals*, PLoS ONE, 10(7): e0134378, July 30, 2015.

10.0.2 Journal Papers (Submitted)

1. M. Bernabei, R. Tinarelli, L. Peretto, L. Rovati, *Measurement of the pupil responses induced by RGB flickerinf stimuli*, IEEE Transactions on Intrumentation and Measurement.

10.0.3 Conference Papers

1. M. Bernabei, R. Tinarelli, L. Peretto, L. Rovati, *Sistema per la misura del diametro pupillare in condizione di flicker policromatico*, XXX Congresso Nazionale GMEE, pp. 241-242, Trento, 2013.

2. M. Bernabei, R. Tinarelli, L. Peretto, L. Rovati, *A simple handheld pupillometer for chromatic Flicker studies*, Proc. of SPIE 8930, Ophthalmic Technologies XXIV, San Francisco, USA, 2014.

3. M. Bernabei, R. Tinarelli, L. Peretto, L. Rovati, *A simple portable polychromatic pupillometer for human eye annoyiance measurement*, Proc. of the IEEE I2MTC 2014, pp. 1207-1211, Montevideo, Uruguay, 2014.

4. S. Cattini, L. Rovati, M. Bernabei, D. Cianciavicchia, P. Monari, A. Sicuri, *A simple measuring system for early detection of haemolysis during haemodialysis*, Proc. Of IEEE I2MTC 2014, pp282-287, Montevideo, Uruguay, 2014.

5. M. Bernabei, R. Tinarelli, L. Peretto, L. Rovati, *Misura della risposta pupillare condizionata dalla stimolazione della melanopsina*, XXXI Congresso Nazionale GMEE, pp. 355-363, Ancona, 2014.

6. M. Bernabei, R. Tinarelli, L. Peretto, L. Rovati, *Measurement of the pupil responses induced by RGB flickerinf stimuli*, I2MTC 2015, pp. 1634-1639, Pisa, Italy, 2015.

7. M. Mandurrino, M. Goano, S. Dominici, M. Vallone, F. Bertazzi, G. Ghione, M. Bernabei, L. Rovati, G. Verzellesi, M. Meneghini, G. Meneghesso, E. Zanoni, *Trap-assisted tunneling contributions to subthreshold forward current in InGaN/GaN light-emitting diodes*, Proc. SPIE 9571, Fourteenth International Conference on Solid State Lighting and LED-based Illumination Systems, 95710U San Diego, USA, September 8, 2015.

8. M. Bernabei, R. Tinarelli, L. Peretto, L. Rovati , *Misura della risposta pupillare da stimoli luminosi RGB*, , XXX Congresso Nazionale GMEE, Lecco, 2015.

9. G. Verzellesi, M. Bernabei, L. Rovati, M. Mandurrino, F. Bertazzi, M. Goano, M. Meneghini, G. Meneghesso, E. Zanoni, *Efficiency droop in Gallium Nitride based light-emitting diodes: physical mechanism and technological remedies*, EMN Meeting, Guangzhou, 12/2015.

Note in the bibliography references the IEEE style replaces author names that are identical to the previous reference with a long dash.

Bibliography

[1] D. Cao, N. Nicandro, and P. Barrionuevo, "A five-primary photostimulator suitable for studying intrinsically photosensitive retinal ganglion cell functions in humans," *Journal of Vision.*, vol. 15(1), p. 27, 2015.

[2] "Solid-state lighting research and development: Manufacturing roadmap," U.S. Department of Energy, www1.eere.energy.gov/buildings/ssl/techroadmaps.html., Tech. Rep., 2012.

[3] "Solid-state lighting research and development: Multi-year program plan," U.S. Department of Energy, www1.eere.energy.gov/buildings/ssl/techroadmaps.html, Tech. Rep., 2012.

[4] IEC, "Photobiological safety of lamps and lamp systems," Int. Org. Standardization, Geneva, Switzerland, Tech. Rep., 2006.

[5] P. Iacomussi, G. Rossi, and L. Rossi, "A comparison between different light sources induced glare on perceived contrast," in *Proceedings of the 27th Session of the CIE*, 2013.

[6] F. Behar-Cohen, C. Martinsons, F. Viénot, G. Zissis, A. Barlier-Salsi, J. Cesarini, O. Enouf, M. Garcia, S. Picaud, and D. Attia, "Light-emitting diodes (led) for domestic lighting: Any risks for the eye?" *Progress in Retinal and Eye Research*, vol. 30, pp. 239–250, 2011.

[7] R. Kuller and T. Laike, "The impact of flicker from fluorescent lighting on well-being, performance and physiological arousal," *Ergonomics*, vol. 41, pp. 433–447, 1998.

[8] J. Veitch and S. McColl, "Modulation of fluorescent light: Flicker rate and light source effects on visual performance and visual comfort," *Lighting Research and Technology*, vol. 27, pp. 243–256, 1995.

[9] IEEE, "Testing and measurement techniques: Flickermeter, functional and design specification," Int. Org. Standardization, Geneva, Switzerland, Tech. Rep., 1997.

[10] D. Rand, B. Lehman, and A. Shteynberg, "Issues, models and solutions for triac modulated phase dimming of led lamps," in *IEEE Power Electronics Specialists Conference*, 2007.

[11] L. Peretto, L. Rovati, G. Salvatori, R. Tinarelli, and A. Emanuel, "Investigation on the response of the human eye to the light flicker produced by different lamps," in *International Instrumentation and Measurement Technology Conference*, Sorrento, 2006, pp. 37–42.

[12] M. Masi, L. Peretto, R. Tinarelli, and L. Rovati, "Measurement of the pupil diameter under different light stimula," in *International Instrumentation and Measurement Technology Conference*, Singapore, 2009, pp. 1652–1656.

[13] ——, "Assessment of human annoyance under flicker condition," in *International Instrumentation and Measurement Technology Conference*, Binjiang, 2011, pp. 1–5.

[14] J. Barbur, S. Moro, J. Harlow, B. L. Lam, and M. Liu, "Comparison of pupil responses to luminance and colour in severe optic neuritis," *Clinical Neurophysiology*, vol. 115(11), pp. 2650–2658, 2004.

[15] I. Moro, M. Rodriguez-Carmona, E. Frost, G. Plant, and J. L. Barbur, "Recovery of vision and pupil responses in optic neuritis and multiple sclerosis," *Ophthalmic and Physiological Optics*, vol. 27(5), pp. 451–460, 2007.

[16] K. Bowles and T. Kraft, "Erg critical flicker frequency assessment in humans," *Advances in Experimental Medicine and Biology*, vol. 723, pp. 503–509, 2012.

[17] L. Peretto, L. Rovati, G. Salvatori, R. Tinarelli, and A. Emanuel, "A measurement system for the analysis of the response of the human eye to the light flicker," *IEEE Transactions on Intrumentation and Measurement*, vol. 56, pp. 1384–1390, 2007.

[18] R. Kardon, S. Anderson, T. Damarjian, E. Grace, E. Stone, and A. Kawasaki, "Chromatic pupil responses: preferential activation of the melanopsin-mediated versus outer photoreceptor-mediated pupil light reflex," *Ophthalmology*, vol. 116, pp. 1564–1573, 2009.

[19] ——, "Chromatic pupillometry in patients with retinitis pigmentosa," *Ophthalmology*, vol. 118, pp. 376–381, 2011.

[20] P. Drew, R. Sayres, K. Watanabe, and S. Shimojonostro, "Pupillary response to chromatic flicker," *Exp Brain Res*, vol. 136, pp. 256–262, 2001.

[21] E. Kimura and R. Young, "Nature of the pupillary responses evoked by chromatic flashes on a white background," *Vision Res.*, vol. 35, pp. 897–906, 1995.

[22] J. Li, J. Wang, Z. Liu, and A. Poppe, *Thermal Managment for LED Applications.* Springer, 2014, ch. Solid-State Physics Fundamentals of LED Thermal Behavior.

[23] S. Nakamura, M. Senoh, S. Nagahama, N. Iwasa, T. Matsushita, and T. Mukai, "Blue ingan-based laser diodes with an emission wavelength of blue ingan-based laser diodes with an emission wavelength of 450nm," *Appl. Phys. Lett.*, vol. 76(1), p. 22, 2000.

[24] J. Piprek and S. Nakamura, "Physics of high-power ingan/gan lasers," *IEE Proc.-Optoelectron.*, vol. 149(4), p. 145, 2002.

[25] [Online]. Available: https://it.wikipedia.org/wiki/Lampadaaincandescenza

[26] [Online]. Available: https://it.wikipedia.org/wiki/Lampadaalogena

[27] [Online]. Available: https://it.wikipedia.org/wiki/Lampadafluorescente

[28] [Online]. Available: https://it.wikipedia.org/wiki/Lampadina

[29] [Online]. Available: http://www.britannica.com/EBchecked/topic/1688997/human-eye

[30] J. Schnapf, T. Kraft, and D. Baylor, "Spectral sensitivity of human cone photoreceptors," *Nature*, vol. 325, pp. 439–41, February 1987.

[31] V. C. Smith and J. Pokorny, "Spectral sensitivity of the foveal cone photopigments between 400 and 500 nm," *Vision Research*, vol. 15, no. 161-171, 1975.

[32] O. Estevez and H. Spekreijse, "A spectral compensation method for determining the determining the flicker characteristics of the human color mechanism," *Vision Research*, vol. 14, pp. 823–830, 1974.

[33] L. Stark and P. Sherman, "A servoanalytic study of consensual pupil reflex to light," *Neurophysiol.*, vol. 20, pp. 17–26, 1957.

[34] L. Stark, F. Campbell, and J. Atwood, "Pupil unrest: An example of noise in a biological servomechanism," *Nature*, vol. 182, pp. 857–858, 1958.

[35] L. Stark and F. Baker, "Stability and oscillations in a neurological servomechanism," *J. Neurophysiol.*, vol. 22, pp. 156–164, 1959.

[36] L. Stark, "Stability, oscillations, and noises in the human pupil servomechanism," *Proc. IRE*, vol. 47, pp. 1925–1939, 1959.

[37] ——, "The pupillary control system its non-linear adaptive and stochastic engineering design characteristics," *Automatica*, vol. 5, pp. 655–676, 1969.

[38] F. Sun, W. C. Krenz, and L. Stark, "A systems model for the pupil size effect: I. transient data," *Biol. Cybern.*, vol. 48, pp. 101–108, 1983.

[39] W. C. Krenz and L. Stark, "Systems model for pupil size effect. ii. feedback model," *Biol. Cybern.*, vol. 51, pp. 391–397, 1985.

[40] C. Privitera and L. Stark, "A binocular pupil model for simulation of relative afferent pupil defects and the swinging flashlight test," *Biol. Cybern.*, vol. 94, pp. 215–224, 2006.

[41] A. Longtin and J. Milton, "Insight into the transfer function, gain, and oscillation onset for the pupil light reflex using nonlinear delay-differential equations," *Biol. Cybern.*, vol. 61, pp. 51–58, 1989.

[42] ——, "Modelling autonomous oscillations in the human pupil light reflex using non-linear delay-differential equations," *Bull. Math. Biol.*, vol. 51, pp. 605–624, 1989.

[43] ——, "Evaluation of pupil constriction and dilation from cycling measurements," *Vision res.*, vol. 30(4), pp. 515–525, 1990.

[44] P. C. Bressloff, C. Wood, and P. Howarth, "Nonlinear shunting model of the pupil light reflex," *Proc. R. Soc. Lond. B.*, vol. 263, pp. 953–960, 1996.

[45] V. Pamplona, M. M. Oliveira, and G. Baranoski, "Photorealistic models for pupil light reflex and iridal pattern deformation," *ACM Trans. Graph.*, vol. 28, pp. 106–1–106–12, 2009.

[46] S. Usui and Y. Hirata, "Estimation of automic nervous activity using the inverse dynamic model of the pupil muscle plant," *Biomedical Engeeniring Society*, vol. 23, no. 375-387, 1995.

[47] X. Fan and G. Yao, "Modeling transient pupillary light reflex induced by a short light flash," *IEEE Transactions on Biomedical Engineering*, vol. 58, 2011.

[48] J. L. Barbur, "Learning from the pupil: Studies of basic mechanisms and clinical application," in *The Visual Neurosciences*, L. M. Chalupa and J. S. Werner, Eds. Cambridge: MIT Press, 2003.

[49] A. Tzambazakis, D. Fotiou, A. Fotiou, and D. Tsiptsios, "Pupillary response and attention," *International Journal Of Psychophysiology*, vol. 45(1-2), pp. 104–105, 2002.

[50] A. Tales, T. Troscianko, D. Lush, J. Haworth, G. Wilcock, and S. Butler, "The pupillary light reflex in aging and alzheimer's disease," *Aging Clin. Exp. Res.*, vol. 13, pp. 473–478, 2001.

[51] X. Fan, J. H. Miles, N. Takahashi, and G. Yao, "Abnormal transient pupillary light reflex in individuals with autism spectrum disorders," *J. Autism Dev. Disord.*, vol. 39, pp. 1499–1508, 2009.

[52] D. Kahneman, B. Tursky, D. Shapiro, and A. Crider, "Pupillary, heart rate, and skin resistance changes during a mental task," *J. Exp. Psychol.*, vol. 79, pp. 164–167, 1969.

[53] H. Wilhelm and B. Wilhelm, "Clinical applications of pupillography." *J Neuroophthalmol.*, vol. 23(1), pp. 42–49, 2003.

[54] Y. Chen, H. J. Wyatt, and W. H. Swanson, "Pupillary evaluation of retinal asymmetry: Development and initial testing of a technique," *Vis. Res.*, vol. 45, pp. 2549–2563, 2005.

[55] T. Slamovits and R. Burde, *Neuro-ophtalmology.* Year Book Europe, 1994.

[56] H. Thompson, "Otto lowenstein, pioneer pupillographer," *J Neuroophthalmol.*, vol. 25, pp. 44–49, 2005.

[57] IEC, "International electrotechnical vocabulary, electromagnetic compatibility," Int. Org. Standardization, Tech. Rep., 1990.

[58] EN, "International electrotechnical vocabulary, electromagnetic compatibility," Int. Org. Standardization, Geneva, Switzerland, Tech. Rep., 1997.

[59] EN50160, "Voltage characteristics of electricity supplied by public distribution systems," IEC, Geneva, Switzerland, Tech. Rep., 2004.

[60] C. Rashbass, "The visibility of transient changes of luminance," *Journal of Physiology*, vol. 210, pp. 165–186, 1970.

[61] J. J. Koenderink and A. J. VanDoorn, "Visibility of unpredictability flickering lights," *Journal of the Optical Society of America*, vol. 64(11), pp. 1517–1522, 1974.

[62] J. Koenderink and A. J. VanDoorn, "Detectability of power fluctuations of temporal visual noise," *Vision Research*, vol. 18, pp. 191–195, 1978.

[63] B. Lorenz, E. Strohmayr, S. Zahn, C. Friedburg, M. Kramer, M. Preising, and K. Stieger, "Chromatic pupillometry dissects function of the three different light-sensitive retinal cell populations in rpe65 deficiency," *Investigative Ophthalmology and Visual Science*, vol. 53, pp. 5641–5652, 2012.

[64] A. Wilkins, N. Smith, A. Slater, and L. Bedocs, "Fluorescent lighting, headaches and eyestrain," *Lighting Research and Technology*, vol. 21(1), p. 11, 1989.

[65] R. S. Fisher, G. Harding, G. Erba, G. Barkley, and A. Wilkins, "Photicand patterninduced seizures: Expert consensus of the epilepsy foundation of america working group," *Epilepsia*, vol. 46(9), pp. 1426–1441, 2005.

[66] A. Wilkins, J. Veitch, and B. Lehman, "Led lighting flicker and potential health concerns: Ieee standard par1789 update," *Energy Conversion Congress and Exposition (ECCE)*, pp. 171–178, 2010.

[67] G. Asmundson and M. Stein, "Vagal attenuation in panic disorder: An assessment of parasympathetic nervous system function and subjective reactivity to respiratory manipulations," *Psychosomat. Med.*, vol. 56, pp. 187–193, 1994.

[68] X. Ming, P. Julu, M. Brimacombe, S. Connor, and M. Daniels, "Reduced cardiac parasympathetic activity in childrenwith autism," *Brain Dev.*, vol. 27, pp. 509–516, 2005.

[69] M. Dustin and K. Wong, "Melanopsin-expressing, intrinsically photosensitive retinal ganglion cells (iprgcs)," *Webvision*, 2015.

[70] K. Stephenson, C. Schroder, G. Bertschy, and P. Bourgina, "Complex interaction of circadian and non-circadian effects of light on mood: Shedding new light on an old story," *Sleep Medicine Review*, vol. 16, pp. 445–454, 2012.

[71] D. H. McDougal and P. D. Gamlin, "The influence of intrinsically photosensitive retinal ganglion cells on the spectral sensitivity and response dynamics of the human pupillary light reflex," *Vision Research*, vol. 50, pp. 72–87, 2010.

[72] Synopsys, *Sentaurus Device User Guide*, 2013.

[73] Ioffe and Institute. Semiconductor parameter database. [Online]. Available: http://www.ioffe.ru/SVA/NSM/Semicond/GaN/index.html

[74] I. Vurgaftman and J. Meyer, "Band parameters for nitrogen-containing semiconductors," *J. Appl. Phys*, vol. 94, p. 2675, 2003.

[75] F. Bernardini and V. Fiorentini, "Macroscopic polarization and band off- sets at nitride heterojunctions," *Phys. Rev. B*, vol. 57(16), p. R9427, 1998.

[76] M. Grupen and K. Hess, "Simulation of carrier transport and nonlinearities in quantum-well laser diodes," *IEEE J. Quantum Electron*, vol. 34(1), p. 120, 1998.

[77] J. Pal, G. Tse, V. Haxha, and M. Migliorato, "Second-order piezoelec- tricity in wurtzite iii-n semiconductors," *Phys. Rev. B*, vol. 84, p. 085211, 2011.

[78] R. J. Lucas, S. Peirson, D. Berson, T. Brown, H. Cooper, C. Czeisler, M. Figueiro, P. Gamlin, S. Lockley, J. O'Hagan, L. Price, I. Provencio, D. Skene, and G. Brainard, "Measuring and using light in the melanopsin age," *TRENDS in Neurosciences*, vol. 37, 2014.

[79] L. Dongheng and D. Parkhurst, "Starburst: A robust algorithm for video-based eye tracking," Iowa State University, Iowa, Tech. Rep., 2005.

[80] M. Fischler and R. Bolles, "Random sample consensus: a paradigm for model fitting with applications to image analysis and automated cartography," *Communications of the ACM 24*, vol. 6, pp. 381–395, 1981.

[81] M. G. Masi, L. Peretto, R. Tinarelli, and L. Rovati, "A pupil size measurement system for the analysis of the impact of flicker on human being," in *Proc. of the 16tth IMEKO TC-4 Symposium*, 2008, pp. 22–24.

[82] EN13005, "Evaluation of measurement data – guide to the expression of uncertainty in measurement," JCGM, Tech. Rep. 100:2008, 2008.

[83] S. Hecht, C. Haig, and A. Chase, "The influence of light adaptation on subsequent dark adaptation of the eye," *J.gen.Physiol. 20*, vol. 831-850, 1937.

[84] J. Park, A. Moura, A. Raza, D. Rhee, R. Kardon, and D. Hood, "Toward a clinical protocol for assessing rod, cone, and melanopsin contributions to the human pupil response," *Investigative Ophthalmology and Visual Science*, vol. 52, pp. 6624–6635, 2011.

[85] E. Schubert, *Light-Emitting Diodes 2nd Edition.* Cambridge University Press, 2010.

[86] Hattar, H. W. Liao, M. Takao, D. M. Berson, and K. W. Yau, "Melanopsin-containing retinal ganglion cells: architecture, projections, and intrinsic photosensitivity," *Science*, vol. 295, no. 1065-1070, 2002.